Study of Ferromagnetic and Field Effect Properties of ZnO Thin Films

XIA, Daxue

A Thesis Submitted in Partial Fulfilment

of the Requirements for the Degree of

Doctor of Philosophy

in

Electronic Engineering

The Chinese University of Hong Kong

February 2011

UMI Number: 3492006

UMI

Dissertation Publishing

ProQuest

Abstract

Spintronics (spin transport electronics), in which both spin and charge of carriers are utilized for information processing, is perceived to be a candidate to extend and possibly to become the next-generation electronics. Its advantages include nonvolatility (data retention without electrical power), lower energy consumption, faster processing speed, and higher integration densities in comparison with the current semiconductor devices relying solely on electron charge. To realize a spin-field effect transistor, two respects are prerequisite. On the one hand, the mechanism of ferromagnetism should be addressed before one could prepare magnetic semiconductor films in a controllable way. On the other hand, excellent field effect properties should be sought through a convenient and low-cost strategy for manufacturing future nano-scale spintronic devices. This thesis is comprised of two parts. Firstly, it deals with the synthesis, characterization, and magnetism of transition-metal-doped or un-doped zinc oxide (ZnO) thin films. Secondly, it focuses on the field effect properties of solution processable ZnO thin films, which are not only of great interest for current charge-carrier based thin film transistors, but also of fundamental importance in future spin-based transistors.

A facile spin-coating technique has been developed to fabricate ZnO thin films. Even without magnetic element doping, the film is found to show room temperature ferromagnetism. A broad series of advanced microscopic and spectroscopic techniques are utilized to characterize the thin films properties. Oxygen vacancy defects are tentatively attributed to the observed ferromagnetism. Following the similar method, Ga doped or Ga, Co co-doped ZnO thin films are prepared. The ferromagnetism is enhanced with Ga doping, providing more carriers. It is discovered that room temperature ferromagnetism can exist in both highly conductive regime and the less conductive or near insulating regime. Transition metal

I

doping is not necessary to realize ferromagnetic coupling. By annealing single crystalline ZnO in high vacuum, similar hysteresis loops indicative of ferromagnetism have been observed, which excludes the interfacial and grain boundary effects in polycrystalline ZnO as the origin of ferromagnetism.

High performance thin film transistors are featured by high carrier mobility, low power consumption, facile and low cost fabrication process, low temperature preparation, and high throughput to meet the demands in next generation large area and flexible display technology. By developing a novel process to fabricate alumina gate dielectric and proper doping into ZnO thin films, the high performance devices are attained with larger mobility than most ever reported devices fabricated by low cost solution process without high temperature annealing. By employing this technique, the device is endowed with almost all features mentioned above. Spin-coated alumina provides unique dielectric properties, excellent thermal stability, visible transparency, low cost, and seamless integration with oxide channel layers, which will probably pave the way for wide applications in transparent flexible electronics in future.

This thesis research contributes a deeper insight into the microscopic origin of ferromagnetism in wide-band-gap oxide based DMSs. Meanwhile, a novel process of alumina gate dielectric dedicated to low operating voltage application has been unveiled, with which the field-effect performance of ZnO TFTs has been significantly improved. This technique may not only make significant impact on conventional charge based transparent electronics, but also might provide clues and simple platforms in future to investigate the spin-related field effect properties in ZnO.

博士學位論文摘要

自旋電子學是一門新興學科，它同時利用電子的電荷和自旋來進行信息的存儲和處理．這一新興技術將挑戰進而有望取代目前只依靠載流子電荷作爲信息載體的微電子學．相形之下，前者的優勢包括非揮發性（即數據無需電源維持而保存），低能量損耗，更快的處理速度以及更高的集成密度．爲了實現自旋場效應晶體管，有兩個問題必須克服．其一，人們對磁性半導體的鐵磁性機理必須有明確的理解，由此人們才能夠可控地獲得滿足磁電效應的器件；其二，高性能的場效應特性應當能夠通過一種低成本高產出的方式獲得．本文首先研究了氧化鋅薄膜的合成，通過各種結構以及性能表征手段，研究了磁電相關性．其次，研究了基于傳統電荷爲信息載體的氧化鋅薄膜晶體管的場效應，系統地研究了溶液方法的制備參數對器件性能的影響，報道了一種通過簡單方法可獲得的介電層，使得器件的特性比前人的報道有了大幅度的改善和提高．

采用簡單的旋塗法，我們制備了氧化鋅薄膜．實驗發現，即使沒有磁性金屬離子的摻雜，同樣可以觀察到氧化鋅薄膜的常溫鐵磁性．通過一系列的微觀結構和成分分析（x 射線衍射，x 射線光電子能譜，ICP-MS 等)和光譜技術（拉曼光譜，熒光光譜，陰極射線光譜等)，排除了鐵磁性雜質的影響，發現鐵磁性與薄膜中的氧空位缺陷密切相關．當摻入了 Ga 等施主雜質後，電子的濃度大爲增加．同時氧化鋅薄膜的鐵磁性大幅度增強．實驗發現，隨著氧化鋅薄膜的載流子濃度變化，薄膜的導電機制發生變化．這種變化也導致了鐵磁性作用的強弱發生改變．同時，我們將單晶氧化鋅 置于高真空腔內退火，同樣可以觀察到鐵磁性．這表明，薄膜與基片間的界面效應以及多晶晶粒中的晶界效應不可能是產生鐵磁性的源泉．

高性能的薄膜晶體管通常包含以下特點，高載流子遷移率，低功耗，簡單制備工藝，低成本，低制備工藝溫度以及高制備產出效率．這類晶體管可滿足下一代大面積柔性襯底上的顯示技術要求.本文采用一種新的方法制備了氧化鋁柵極介電層，結合氧化鋅優選摻雜,獲得了迄今由溶液方法並由低溫退火制備的晶

體管的最大電子遷移率．這種工藝技術賦予了晶體管幾乎包含上述高性能器件的所有優點．用旋塗法制備的柵極介電層，提供了許多其他介電材料無法給予的優良特性，包括較高的單位面積電容，較小的漏電電流，高溫熱穩定性，透明性，低成本，以及與氧化物溝道層的無縫銜接．相信這一技術將對透明電子技術的發展產生積極的推動作用．

本文不僅加深了人們對氧化物稀磁半導體的磁性機理的認識和理解，對原有提出的模型提出了修正和擴充．同時，我們發現了旋塗法合成的氧化鋁的優異的介電性能，使得氧化鋅薄膜晶體管的性能得到大大提高．這一研究雖然是建立在傳統的電荷型晶體管之上，但是我們相信它不僅對于當今的常規薄膜晶體管的應用有著積極的促進作用，同時也爲將來自旋場效應晶體管提供了新的研究思路和平台．

Acknowledgement

Table of contents

List of Tables

List of Figures

Chapter 1 Introduction

1.1 Spintronics

Since the 1970's, the national security, economic growth and daily lives in our societies have reaped the benefits of the rapid improvement of computers, appliances and communication devices, in their improved performance and decreased costs by virtue of Moore's Law. The Law postulates that circuit performance or the number of transistors per chip doubles roughly every 18 months. The information technology pertaining to the modern microelectronics has created a multi-trillion dollar industry globally per year whose products are entirely ubiquitous. However, manufacturers in the present microelectronic industry have recognized the continued advances predicted by Moore's Law will cease in the near future [1]. It is due to the fact that current microelectronic devices composed of transistors would have been scaled down to sizes where quantum effects are beginning to interfere the functionality, resulting in severe leakage currents. The limitation of top-down technology has motivated efforts worldwide to search for new strategies. Spintronic devices are anticipated to be the ideal solution to such an standoff in that spin of electron can also carry information, be easily manipulated by externally applied magnetic fields and survive for relatively long coherence times [2,3]. Accordingly, the potential advantages of spintronic devices would be non-volatility (permitting data retention in non-powered conditions), lower energy consumption, faster processing speed, and higher integration densities compared with today's semiconductor devices that rely solely on electron charge [2]. By exploiting these benefits, computers may become much faster and chips may become much smaller. Moreover, they are expected to play an increasing technological role in future high-density 3D data storage, magnetic sensors, quantum computing, and biomedical applications.

There is strong evidence that the technology shift taking place from

microelectronics to spintronics will help to meet the sensing and storage demands of information technology in the 21st century. The next-generation electronics, spintronics, will bring us new technologies to further improve quality of our life. For example, we might see more powerful computers and robots equipped with spin-based microprocessors that could liberate us from heavy mental and physical tasks dramatically. It is anticipated that the impact of spintronics on the microelectronics industry and other fields could be comparable to the development of the laser/transistor research in the last century [4]. It will most likely have a significant impact on the future of all aspects of electronics as we continue to move into the 21st century

Spintronics (spin-transport electronics) is a nascent area of breakthrough science with expected outcomes of advanced materials and nanotechnology. It is a rapidly boosting interdisciplinary research field, extensively involving physics, materials science and solid state electronics [1, 2, 5, 6]. Spintronics exploits the inherent quantum properties of electron spin as well as the other degree of freedom of charge for memory and logic operations [2]. Splitting and manipulating the spin-up and spin-down currents (a new kind of binary logic of one and zero) through nanostructuring of magnetic materials is promising to add a new dimension to the practice of electronics. All spintronic devices act according to the following schemes: (i) information is stored (written) into spins as a particular spin [6], orientation (up or down); (ii) the spins, being attached to mobile electrons, carry the information along a wire; and (iii) the information is read at a terminal [6].

Spintronics first emerged in 1988 when giant magnetoresistance effect was discovered in metallic thin film sandwich multilayer heterostructures, which are the basis for the earliest spin-dependent spin-valve device [7]. The device clearly demonstrated that the electronic properties of materials can be manipulated by magnetic field.

There are several other kinds of spintronic devices, the most two important of which includes spin field effect transistors (spin-FET) and spin-LED.
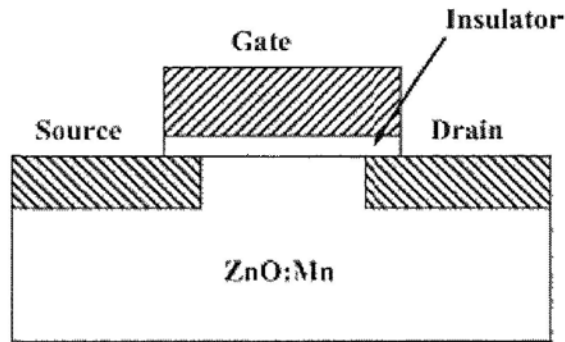
Fig.1-1-1 A schematic of a spin-FET based on transition metal-doped ZnO. Co-doped ZnO can be used as the source and drain contacts (adapted from Ref. [8]).

Sato and Katayama-Yoshida proposed a ZnO based spin-FET, as shown in Fig.1-1-1. The authors did first principles calculations for the ground state of transition metal-doped ZnO, and concluded that (Zn, Mn)O is of antiferromagnetic ground state, and ferromagnetism can be induced by hole doping. In this proposed structure, holes can be injected into Mn-doped ZnO by applying a negative bias gate voltage, and the system changes to a half-metallic ferromagnet. When ferromagnetic (Zn, Co)O is used for source and drain contacts, spin polarized electrons can flow in half metallic (Zn, Mn)O.
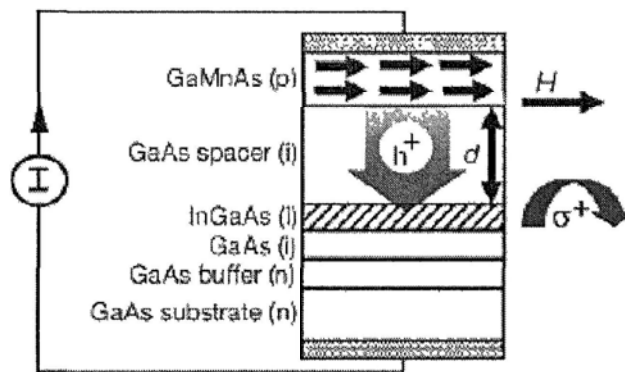
Fig.1-1-2 Injection of spin-polarized holes into a light-emitting p-n diode using a ferromagnetic semiconductor (Ga, Mn)As. (a) Sample structure. Spin-polarized holes h+ travel through the nonmagnetic GaAs and recombine with spin-unpolarized electrons in the (In,Ga)As quantum well. I represents the current, and σ+ represents circularly polarized light emitted from the edge of the quantum well (adapted from Ref. [9]).

3

Spin light emitting diode (spin LED) allows modulating the polarization of the light emitted by the spin LED by application of an external magnetic field, which is of interest to optical switching and optical communication with increased bandwidth. Spin polarized light emission has been demonstrated in II–VI semiconductors [10] and III–V GaAs [9]. The latter is discussed here, particularly since the GaN varieties are not yet available and there are some fundamental issues whether one circular polarization over the other is promoted. The sample structure of a GaAs-based spin LED is depicted in Fig.1-1-2. The structure contains a p-type ferromagnetic semiconductor (Ga, Mn)As and n-type nonmagnetic semiconductor GaAs, which were epitaxially grown by MBE. The use of ferromagnetic (Ga, Mn)As allows one to inject spins in the absence of magnetic field. Spontaneous magnetization develops below the Curie temperature in the ferromagnetic p-type (Ga, Mn)As semiconductor, indicated by the arrows in the (Ga, Mn)As layer. Under forward bias, spin polarized holes are injected from the (Ga, Mn)As side into the nonmagnetic region and recombine with spin unpolarized electrons injected from the n-type GaAs substrate in a nonmagnetic quantum well made of (In, Ga)As (hatched region), as shown in Fig. 1-1-2, through a spacer layer with thickness d producing polarized electroluminesence (EL). Due to the crystal symmetry of GaAs, injected spin-polarized electrons have been detected in the form of circularly polarized light emission from the quantum well, which corresponds to the magneto-optical Kerr effect loops and can be directly related to spin-polarization. The presence of spin polarization has been confirmed by the observation of hysteresis in the polarization of the emitted light as a function of the magnetic field. The Curie temperature of (Ga, Mn)As is 52 K.

Both above devices have not yet realized in practical application, as a result of insufficient understanding of the mechanism of ferromagnetism in DMS. As one of the goals, the present work is dedicated to provide new insights and promote the complete understanding.

1.2 Spintronic materials--dilute magnetic semiconductors

Just as silicon forms the heart of microelectronics, spintronic materials will be the material bases of spintronics. No matter what kinds of spintronic devices are designed, none of them can be realized without qualified spintronic materials that will effectively allow spin-polarized carriers to be injected, transported, and manipulated in the device. The candidates for spintronic materials are half-metals [2,11], magnetoelectric multiferroics [12-14], diluted magnetic (semi-magnetic) semiconductors (DMSs) [2, 5, 14-16] and etc. Among them, DMSs are fascinating materials that combine both ferromagnetic and semiconducting properties [17], thus allowing in principle the possibility of combining logic and storage operations on the same semiconductor chip [16]. By randomly replacing cation sites of the host nonmagnetic semiconductors with minute amounts of TM ions or rare earths, as illustrated in Fig.1-2-1 [16], one can make diluted ferromagnetic semiconductors such as (Ga, Mn)As and (In, Mn)As [5,15,18]. Fig. 1-2-2 shows the schematic density of states of a DMS below Curie temperatures (T_C), in which magnetic exchange interactions split the spin up and spin down bands at the Fermi level, leading to 100 % spin polarization [2]. However, the T_C of those "conventional" ferromagnetic semiconductors are too low (typically below 200 K) to fulfill the practical spintronics applications [15,18]. This requires the above-room-temperature ferromagnetic semiconductor, normally Tc over 500 K for practical applications. In 2000, Dietl *et al.* used a mean-field theory based on Zener model calculations to predict that room-temperature ferromagnetic semiconductors might be created by substituting proper Mn ions in p-type wide-band-gap semiconductors such as GaN and ZnO (see Fig. 1-2-3), provided that the hole density is sufficiently high [19]. Shortly thereafter, the topical wide-band-gap oxide DMSs, such as ZnO [20-22], TiO_2 [20,22,23], SnO_2 [24] and In_2O_3 [25] and nitride DMSs, such as GaN [20,22] and AlN [20] have become extensively studied. Nonetheless, there is a strong open debate in the reported magnetic behaviors and theories.
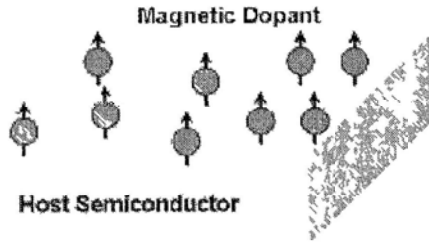
Fig.1-2-1 The host semiconductor appears ferromagnetic when incorporated a few percent of magnetic dopant (Adapted from Ref. [16]).
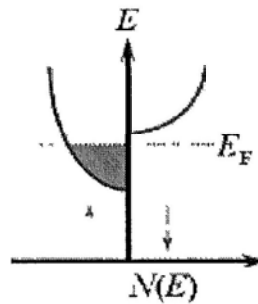
Fig.1-2-2 A schematic "half-metallic" density of states of a DMS below T_C. E is the electron energy, E_F is the Fermi level, and $N(E)$ is the density of states (Adapted from Ref. [6]).
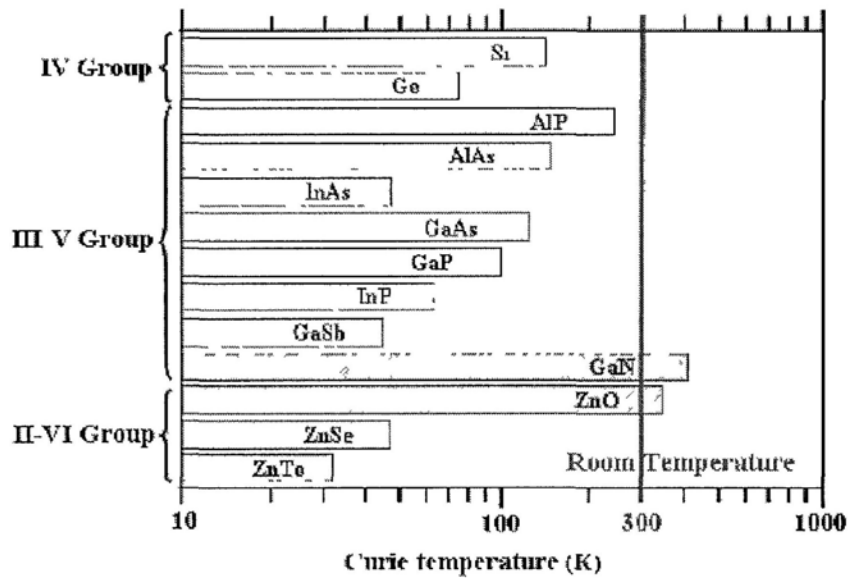
Fig.1-2-3 Predicted Curie temperature for 5 % Mn-doped p-type semiconductors containing a sufficiently high hole density of 3.5×10^{20} cm^{-3}, determined using a Zener model (Adapted from Ref. [19]).

The search for high-T_C ferromagnetic semiconductors has led to numerous studies on various candidate materials. Within the realm of DMSs, the wide-band-gap diluted magnetic oxides such as ZnO [20-22], TiO_2 [20,22,23], SnO_2 [24] and In_2O_3 [25] are the particularly desirable host materials because they possess unusual optical and electronic properties for integrated opto-spintronics applications in addition to their other merits, such as low cost, environmentally safe, easy processing, and etc. Although the state-of-the-art theoretical and experimental studies on high-T_C FM in these diluted oxides have been widely reported since Dietl's prediction in 2000 [19], the origins of magnetic interactions have remained highly controversial and confusing [20,22]. This is one of our direct reasons in mind to employ a broad spectrum of advanced techniques to carefully investigate the magnetic properties and microstructures, thus providing the in-depth insight into origin of magnetism—such a debated problem so far. In the following, the latest progress in the theoretical and experimental studies on oxide DMSs is reviewed.

(1) Theoretical Studies

The mechanisms responsible for the intrinsic FM have not been fully understood and been still in its infancy so far. The theory dealing with FM driven by the exchange interaction between carriers and localized magnetic ions was first proposed by Zener [26]. Zener theory indicates that direct superexchange between the magnetic ions is not ferromagnetic but the indirect superexchange involving carrier mediation is. Therefore, the features of DMSs are induced by the exchange interaction between localized d shell electrons of the magnetic ions and the delocalized band carrier states (s or p origin), namely sp-d exchange. In recent years a large number of theoretical efforts have been undertaken to explain the detailed exchange mechanisms involved in FM. But there are still notable variations between the theoretical and experimental results. Models based on the (i) Ruderman-Kittel-Kasuya-Yosida (RKKY) interactions, (ii) mean-field theory, (iii) double exchange, (iv) magnetic polarons, (v) nanoscale phase separation; (vi) *ab initio* calculations, and etc., have been developed to account for the magnetic properties observed experimentally. It is believed that

with the significant improvements in the experimental techniques for DMSs, for example, an advanced electron energy-loss magnetic circular dichroism (EMCD) technique was invented and reported in Nature in 2006 [27], the theories pertinent to understanding of the underlying mechanisms in DMSs would be expected to get coherent in due time.

I. Ruderman-Kittel-Kasuya-Yosida (RKKY) model

Early attempts to understand the magnetic behavior of DMSs are based on models in which the local magnetic moments are assumed to interact with each other via RKKY interactions. The basic idea behind the RKKY interaction is based on the exchange coupling between the magnetic ion and the conduction band free electrons [28]. The conduction electron is magnetized in the vicinity of the magnetic ion, with the polarization decaying with distance from the magnetic ion in an oscillatory fashion. This oscillation causes an indirect superexchange interaction (RKKY) between two magnetic ions on the nearest or next nearest magnetic neighbors. This coupling may result in a parallel (ferromagnetic) or an anti-parallel (antiferromagnetic) setting of the moments dependent on the separation of the interacting atoms. The model becomes efficient when a high concentration of free carriers is present especially at higher temperatures.

II. Mean-field Zener model

Dietl *et al.* used mean-field Zener model to successfully predict T_C in various p-type semiconductors (see Fig.1-2-3) [19]. This model assumes that FM occurs through long-range interactions between the local moments of the Mn atoms mediated by free holes in the material by use of mean-field approximation. As compared to the RKKY interaction, the mean-field Zener model takes into account the anisotropy of the carrier-mediated exchange interaction associated with the spin-orbit coupling in the host materials. In the process it reveals the important effect of the spin-orbit coupling in the valence band in determining the magnitude of T_C and the direction of the easy axis in p-type ferromagnetic semiconductors. However, it overestimates the T_C substantially for lower magnetic ion concentrations.

III. Double exchange model

Sato and Katayama-Yoshida performed *ab initio* calculations of the electronic structures of TM-doped ZnO and proposed the double exchange mechanism for the carrier-mediated FM [29]. In this model, magnetic ions in different charge states couple with each other by virtual hopping of the extra electron from one ion to the other, which has been well developed for mix-valence manganites [30]. In the oxide DMSs, double exchange is thought to be not suitable to explain the high-temperature FM because T_C in this model is proportional to the density of carriers and the band width [31].

IV. Bound magnetic polaron (BMP) model

The BMP model is inherently applied to low carrier density systems [32]. BMPs are formed by the alignment of the spins of many TM ions with that of much lower number of weakly bound carriers within a polaron radius (Fig.1-2-4). The localized carriers of the polarons act on the TM impurities surrounding them, thus producing an effective magnetic field and aligning all spins. The average radius of BMP increases exponentially with decreasing temperature, finally overlapping with other isolated BMP, thus leading to the ferromagnetic transition at percolation [32]. Recently Coey and co-workers have used a spin-split donor impurity-band model based on BMPs to explain the observed systematic variation of magnetic moments across the TM-doped ZnO series [33], where Co shows much larger magnetic moment than other TM metals. High T_C's are found whenever unoccupied $3d$ states overlap the impurity band, but not otherwise. This model elegantly solved the gap between high T_C and insulating behavior of diluted ferromagnetic oxides. Complementarily, Calderon and Das Sarma suggested that a combination of BMP model at low temperatures and RKKY-Zener model at high temperatures should be responsible for the high-T_C FM in oxide DMSs [31].

9

Fig.1-2-4 Interaction of two BMPs. The polarons are shown with gray circles; small and large arrows show impurity and localized carrier spins, respectively (Adapted from Ref. [32]).

V. Nanoscale phase separation model

Since no quantitative arguments supporting the polaron scenario have been put forward, Dietl and Sato *et al.* have proposed this new model recently [34]. There are two kinds of phase separation in this model [34], the spinodal decomposition (chemical phase separation) and disorder-driven electronic phase separation. In spinodal decomposition, nanoscale phase is separated into regions with low and high concentrations of the magnetic constituent, in which the high concentration of magnetic constituent accounts for the high-T_C FM in the most of DMSs. On the other hand, the disorder-driven nanoscale phase can be separated into paramagnetic and ferromagnetic regions below and close to the apparent T_C. The paramagnetic phase can persist down to the lowest temperatures that are characterized by the blocking temperature (T_B). Theoretically, T_B could be approximated by:

$$T_B \approx KV / 25k_B$$

(1-1)

where K is the density of the magnetic anisotropy energy, V is the nanoparticle volume, KV product means the energy barrier for the magnetization reversal in a single particle, and k_B is Boltzmman's constant. The ferromagnetic ordering exists in the regions where the carriers mediate long-range ferromagnetic interactions between the randomly distributed TM ions. This model well explains why insulating DMSs can have the high-T_C FM. Co-doping and post-growth processing are very effective to control the distribution of charge states of magnetic constituents and the resultant FM.

VI. Ab initio calculations

Ab initio first-principles spin-density functional theory (DFT) calculations are more definitive than other theories/models because the calculations are comprehensive by nature in terms of being inclusive of all the mechanisms that may take place. It is viable to obtain an accurate determination of whether the material is ferromagnetic and if so what the T_C is. After Dietl and co-workers predicted hole-mediated FM above room temperature in p-type Mn-doped ZnO [19], Sato *et al.* predicted that the high-T_C FM could be realized in V, Cr, Fe, Co, and Ni-doped n-type ZnO as well by performing *ab initio* calculations based on the local density approximation (LDA), as shown in Fig. 1-2-5 [35]. Recently, the "beyond-LDA" methods are proposed to handle the strong correlation effects and lattice relaxations in the theoretical calculations. Using generalized gradient approximation-based *ab initio* calculations, Lee and Chang also found that electron doping stabilizes the FM in Co-doped ZnO, and a high concentration of both Co ions and electron carriers are necessary to achieve FM in (Zn,Co)O [36]. In the similar way, Wang *et al.* also
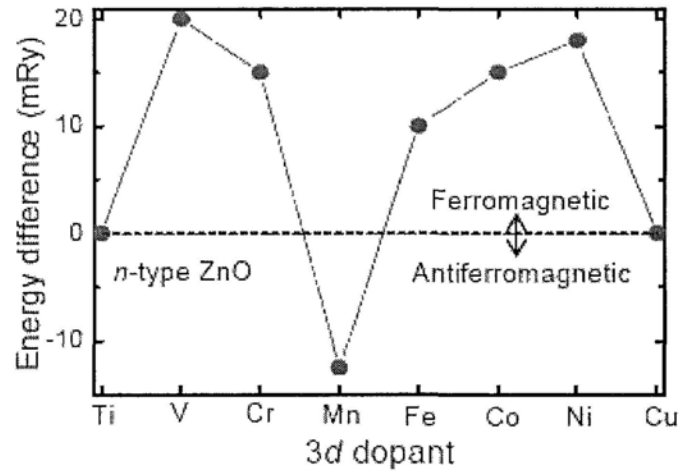
Fig.1-2-5 *Ab initio* calculations of magnetic configurations for TM-doped ZnO. The vertical axis shows the total energy difference per unit cell between the ferromagnetic and the antiferromagnetic states. Positive energy difference means that the ferromagnetic state is more stable than the antiferromagnetic state. 1 mRy $\approx$ 0.0136 eV (Adapted from Refs. [29] and [35]).

calculated the total energies of (Zn,Mn)O [37], finding that in the diluted limit when Mn atoms are far apart, the system is paramagnetic; as the Mn concentration increases, the system is antiferromagnetic, leading to the spin-glass state. The ferromagnetic ground state of (Zn,Mn)O is stabilized by N co-doping (hole doping) by virtue of the large hybridization of the N $2p$ states with the Mn $3d$ states, consistent with predictions by Dietl *et al.* [19] and Sato *et al.* [35]. Using LDA-based *ab initio* calculations, Hu *et al.* showed that Co atoms favor antiferromagnetic coupling through oxygen without additional carriers and semiconductor band structures were obtained in (Zn,Co)O [38]. Gopal and Spaldin reported that the ferromagnetic state is generally disfavored in the realistic (LDA + U) calculations, and the calculated magnetic behavior is strongly dependent both on the computational details and the choice of Hubbard coefficient U [39]. Using an all-electron B3LYP hybrid DFT study Patterson strongly suggested the important role played by defects indeed in promoting magnetic interactions in (Zn,Co)O [40], which is essentially the same as the impurity-band model proposed by Coey *et al.* [34]. Very recently, Katayama-Yoshida and Sato *et al.* have proposed a unified physical picture of magnetism and an accurate calculation method of T_C in DMSs based on *ab initio* calculations by the Korringa-Kohn-Rostoker coherent-potential approximation (KKR-CPA) method within the LDA [41]. They also proposed that the nanoscale phase separation model associated with spinodal nano-decomposition are responsible for the high-T_C phase in the inhomogeneous system by combining with the Monte Carlo simulations [41].

In summary, most theoretical studies in diluted magnetic oxides and other DMS systems are in agreement with the point regarding the crucial role played by additional carriers/defects in the ferromagnetic state in spite of the general inconsistency.

(2) Experimental Studies

The aforementioned theoretical predictions have launched an explosion of active experimental research on TM-doped ZnO, TiO_2, SnO_2, and In_2O_3 as potential DMS materials for spintronics. A number of approaches have been explored to prepare

oxide DMSs, among which are mostly traditional sputtering, molecular beam epitaxy (MBE), pulsed laser deposition (PLD), metal organic chemical vapor deposition (MOCVD), and vapor transport with ion implantation, mostly with high processing temperature. Depending on the growth conditions employed for growing DMSs, one could readily produce samples that span the entire spectrum of possibilities from single phase (showing intrinsic FM with a wide distribution of T_C, paramagnetism, antiferromagnetism, or spin-glass behavior) to secondary-phase or an interface formation (indicating extrinsic FM) [42, 43], resulting in the difficulties in experimentally identifying the mechanism exactly responsible for the observed FM if it really exists. The inconsistency is, to some extent, caused by the extreme sensitivity of magnetic properties to the sample forms, the associated growth conditions, and post-growth treatment with the sufficiently detailed materials characterization in advance. Furthermore, Mofor et $al.$ reported that the sapphire substrate itself rather than the sample could show ferromagnetic behavior [44]. Abraham et $al.$ reported that the improper handling with stainless steel tweezers can lead to contaminations of the sample [45]. Even etched Si/SiO_2 interfaces can show magnetic hysteresis, too [43]. Consequently, it is of vital importance to carefully correlate the measured magnetic properties with detailed material analysis methods that are capable of detecting other tiny secondary phases and precipitates. According to the theoretical predictions, it is generally believed that only p-type Mn-doped ZnO and n-type Co-doped ZnO can show high-T_C FM. Recently Gamelin and co-workers have made a significant progress in experiment to verify such a bipolar regulation, as summarized in Fig.1-2-6 [46], which place the reports of ferromagnetic n-type (Zn,Mn)O on a questionable position. One report by Philip et $al.$ is especially worth noting, which reported high-T_C FM in a truly ferromagnetic semiconductor, i.e., $(In,Cr)_2O_3$ thin film, that fulfilled the perfect spintronic functionality, providing the most convincing and encouraging evidence of high-T_C FM in the oxide thin films, and paved way for the practical silicon-based spintronic microprocessors [4,25]. However, the lack of utilization of relatively low-cost bottom-up synthetic route would prohibit their ultimate commercial realization for the viable nano-spintronics applications. In this regard,

significant attention has been paid to the preparation of nanostructured spintronic materials. Different from the traditional fabrication methods, wet-chemical synthetic routes (including our own work) [47-49] are entering into this realm since solution processing routes are generally combined with the self-assembly strategies that have become a mainstream of nanosicence and nanotechnology. A more detailed summary of recent work on dilute magnetic semiconductors can be found in Ref. [50].
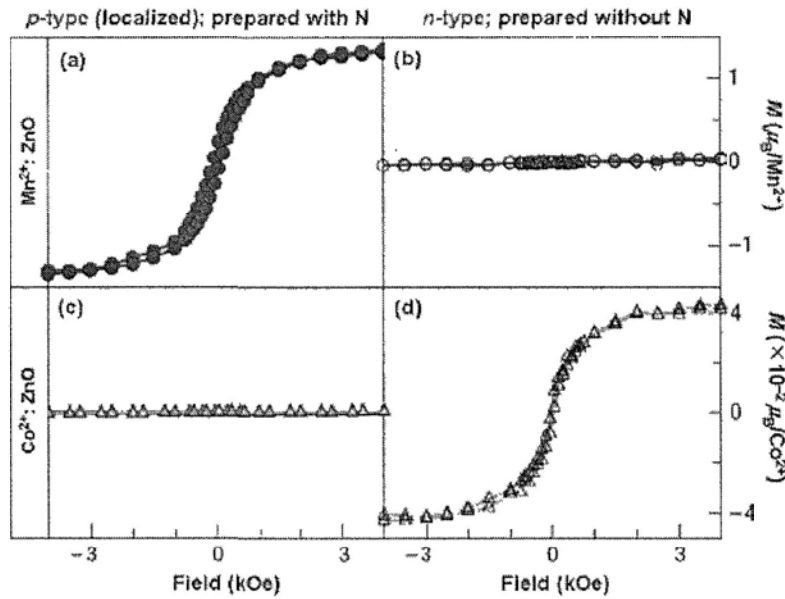
Fig.1-2-6 300 K magnetization data of (Zn, Mn)O and (Zn, Co)O films prepared by direct chemical synthesis with or without addition of nitrogen. (a, b) 0.2 % Mn^{2+}:ZnO with and without added nitrogen, respectively; (c, d) 3.5 % Co^{2+}:ZnO with and without added nitrogen, respectively (Adapted from Ref. [46]).

It is worth noting that recently, various oxides have been reported to show room temperature ferromagnetism even without the doping of magnetic ions. Detailed literature review in this part is summarized in Chapter 2.

Conclusively, although enormous efforts have been made to study the diluted magnetic oxides for more than ten years, and people have gained lots of understanding of their microstructures and properties, there is still a long way to go for these oxide DMSs to be extensively used in nano-spintronics.

1.3 Features of ZnO as a wide band-gap semiconductor

ZnO, as a multifunctional semiconductor with aesthetic morphologies, direct wide band gap (3.37 eV at 300 K), large excitonic binding energy (60 meV), and outstanding electro-optic and piezoelectric properties, has triggered a great deal of interest in the past few years [51]. The seamless integration of FM as a result of TM-doping into ZnO host further expands its multifunctionality into spintronics especially in the aspect of opto-spintronics. Due to its UV light laser emission and low cost, ZnO may become an advantageous alternative to GaN as a UV laser material [52]. Moreover, wet chemical processing of ZnO is feasible; for instance, single-crystal bulk and various ZnO nanostructures have been successfully prepared by solvothermal/hydrothermal technique [53]. ZnO exhibits native n-type conductivity due to electron doping via defects originating mainly from Zn interstitials, O vacancies and/or hydrogen interstitials in the ZnO lattice. However, p-type doping in ZnO remains a big challenge [54]. If hole-mediated FM is the major mechanism in DMSs, the attainment of p-type ZnO could pave the way for a promising prospect for ZnO-based spintronic devices. Further more, n-type ZnO possesses longer spin coherence lifetime (188 ps at 280 K), suggesting that spin polarized electron currents would be sufficiently useful if such currents could be generated in TM-doped ZnO [55]. Compared with GaN, ZnO also crystallizes in the hexagonal wurtzite phase in the P63mc space group (with a = 3.249 Å and c = 5.206 Å). Fig.1-3-1 exemplifies the hexagonal crystal structure of Co-doped ZnO diluted oxide (with Zn sites substituted by Co atoms). The solubility of Co and Mn into ZnO host is usually high and can reach up to 30 % and 35 %, respectively [56,57], mainly due to the fact that $4s^2$ electrons of Co and Mn easily participate in the bonding process with O atom that lacks 2 electrons in its $2p$ shell.
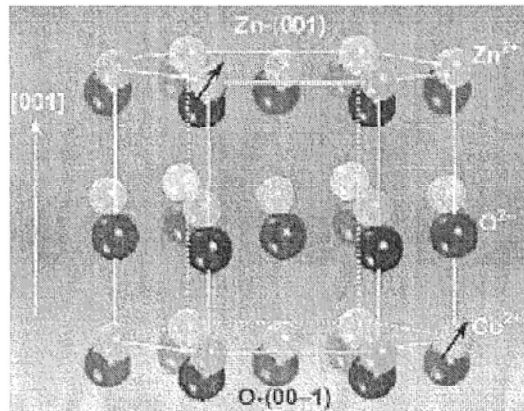
Fig.1-3-1 Schematic lattice structural model of Co-doped ZnO DMS with the hexagonal wurtzite structure. Co^{2+} ions are sitting on the Zn sites and thus produce magnetic moments (arrows). It shows the ±(001) polar surfaces. The intrinsic polar nature of ZnO host makes it grow faster along [001] direction (Adapted from Ref. [58]).

1.4 ZnO-based thin film transistors

Electronic systems that can cover large areas on flexible substrates have received increasing attention in the last couple of decades because they enable classes of applications that lie outside those easily addressed with wafer-based electronics. Examples include flexible displays, electronic textiles, sensory skins, and active antennas [59,60]. This type of electronics, sometimes referred to as macroelectronics, differs from established microelectronic and nanoelectronic systems, where progress is driven primarily by reducing the critical dimensions of the functional elements (e.g., channel lengths and dielectric thicknesses in transistors) to increase the speed and computing capacity and to reduce the operating voltages. Macroelectronics, instead, uses thin-film transistors (TFTs) distributed over large areas where, in existing applications that use glass substrates, they provide switching elements in active-matrix liquid-crystal displays (AMLCDs) or medical X-ray imaging devices [61]. Here, the overall size of the systems rather than the minimum feature size of an individual circuit component represents the primary scaling metric. Amorphous silicon (a-Si) is currently the dominant semiconductor used for transistors in these systems. In fact, this material is now the second most economically significant semiconductor, behind single-crystal silicon. An emerging direction in research is to develop alternative materials and patterning techniques for these macroelectronic systems, with a goal of increasing their performance, decreasing their cost (per unit area), and enabling them to be formed on low-cost, bendable substrates. Low-temperature deposition or printing-type techniques for fabricating of high-quality semiconductor films on substrates such as metal foils [62], plastic sheets [63] and even paper [64] are of particular interest. Integrating semiconductors with plastic substrates which are the most attractive type of flexible substrate for many applications requires processing temperatures below the glass-transition or thermal-degradation temperatures of the plastics. Although many promising results have been obtained with thin films of small-molecule organics and polymers [65], the electrical performance that can be obtained from them is still too low (comparable to

a-Si in the best cases) for many potential applications. Even with high-purity single crystals of these materials, the motilities are less than those of polycrystalline silicon [66,67]. Furthermore, the uncertain long-term reliability and lack of controlled doping techniques for these materials represent other areas that require further research. By contrast, many inorganic semiconductors exhibit high carrier motilities and excellent stability [68]. The main challenge, for uses in macroelectronics on plastics, for example, is that forming high-quality films of these materials and certain steps associated with processing them into devices require temperatures that exceed the glass-transition and/or thermal decomposition temperatures of the plastics. Also, many aspects of the growth and processing do not scale easily to large areas without the use of complex manufacturing systems. Progress in the last several years, however, has led to examples of methods that avoid these limitations. The literatures with regards to this work are reviewed below, emphasizing inorganic semiconductor films that have been, or have the potential to be, integrated with plastic substrates to generate high-performance TFTs, since most of organic electronic materials which have thus far been processed are modest in performance.

I Films of Silicon—From Amorphous to Large-Grained Polycrystalline

TFTs fabricated with hydrogen-terminated amorphous Si (a-Si: H) represent, by far, the most successful systems for applications in large-area electronics. Silicon films with various degrees of crystallinity and mobilities that can be orders of magnitude larger than a-Si: H can be formed using a-Si precursor films and thermal treatments. These films are classified as nanocrystalline Si (nc-Si), microcrystalline Si (μc-Si), and polycrystalline Si (pc-Si). The motilities, in general, increase with grain size because the grain boundaries often represent scattering and trapping sites. Fig.1-4-1 summarizes the properties of different Si films formed through chemical vapor deposition (CVD) approaches.
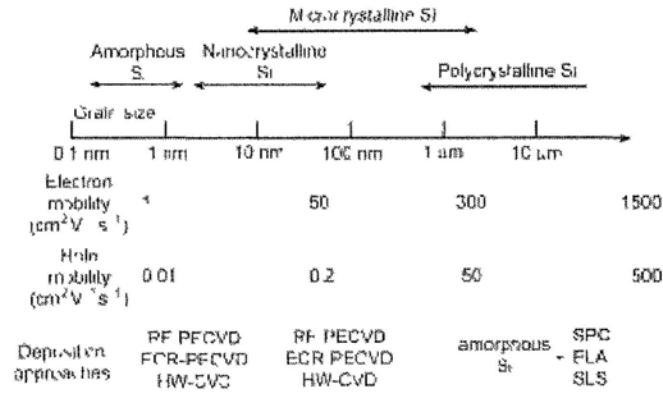
Fig.1-4-1 Grain sizes and carrier mobilities of Si films with various crystallinities grown via dry processes. Abbreviations: RF-PECVD, radiofrequency plasma-enhanced chemical vapor deposition; ECR-PECVD, electron cyclotron resonance plasma-enhanced chemical vapor deposition; HW-CVD, hot-wire chemical vapor deposition; SPC, solid-phase crystallization; ELA, excimer-laser annealing; SLS, sequential lateral solidification (adapted from Ref. [69]).

The main issues of silicon films in applications oriented to above mentioned macroelectronics prepared by various methods, e.g. chemical vapor deposition (CVD) or solution processing include one or several of these: lower mobility (~ 0.1 cm^2 V^{-1}s^{-1}), high temperature, high cost equipment, vacuum requiring and being opaque, etc., which may prevent silicon films, in current forms, from being used with plastic substrates.

II Films of Chalcogenides

Chalcogenide compounds, including sulfides, selenides, and tellurides, are classes of semiconductors that have been used for transistors and other devices since the early days of solid-state electronics. In fact, the first TFT, demonstrated by Weimer in 1962, was fabricated with a thin film of polycrystalline CdS in a structure similar to that of metal-semiconductor field-effect-transistors (MESFETs) [70]. Furthermore, the first AMLCD reported by Brody *et al* in 1973 used CdSe-based TFTs as the pixel switches [71]. Chalcogenide TFTs were successfully fabricated in the 1970s on not only rigid glass slides but also flexible plastics (e.g., Mylar films and Kapton strips) and certain types of paper [72]. The emergence of MOSFETs and integrated circuits based on crystalline Si technology caused a decline in these development activities.

The emergence of nanoparticle and nanowire versions of chalcogenides has led to a re-examination of these materials for transistor applications, particularly in fields such as large-area or flexible electronics, where silicon-wafer-based electronics cannot be used easily.

Typical mobilities in this class of thin films are less or close to 1 $cm^2V^{-1}s^{-1}$ [73,74]. The advantages of this class of materials include the attainment of both p and n type thin film transistors, which is appealing and useful in the fabrication of CMOS circuits, unlike that of oxide thin films based transistors (to be discussed below). However, the mobility is still insufficient. Furthermore, chalcogenide compounds are usually very toxic, which makes them rather unpleasant.

III Films of transparent oxides

Oxides of transition metals, such as ZnO and its derivatives, provide another class of inorganic semiconductor for large area electronics. These oxides are usually transparent in the visible owing to their large bandgaps of >3 eV. This optical behavior, when combined with transparent conductors and dielectrics, allows unusual applications, such as invisible electronics for heads-up displays on windshields or cockpit enclosures. Such oxide thin films, with properties suitable for TFTs, can be formed on both inorganic and plastic substrates by either gas-phase deposition or solution processes.

Radiofrequency magnetron sputtering [75] and pulsed-laser deposition [76] are the most commonly used techniques to form films of ZnO for device applications. Mobility as large as 70 $cm^2V^{-1}s^{-1}$ has been reported at room temperature deposition [77]. p-type ZnO thin films can also be prepared by pulsed laser deposition technique, using P or As as the dopant, although the p-type field effect has seldom been observed.

ZnO films can also be formed by spin-coating solution suspensions of ZnO nanocrystals in the form of chemically synthesized and functionalized spheres or rods. Although the mobility of ZnO thin films prepared by spin-coating method is usually less than 1 $cm^2V^{-1}s^{-1}$, obviously much worse than sputtered films, they are

20

nevertheless interesting owing to the compatibility of solution-based techniques with low cost, large-area deposition. It is because of this great potential significance in practical application, in this work, field effect properties of ZnO thin films prepared by spin-coating are investigated.

ZnO can crystallize with other materials, such as In_2O_3, Ga_2O_3, and SnO_2, to form binary or ternary oxides that are transparent and offer high mobility. An example is single crystalline $InGaO_3(ZnO)_5$ (IGZO) films, which can be epitaxially grown on (111) single-crystal yttria-stabilized zirconia (YSZ) substrates, with mobilities as high as ca. 80 cm^2V^{-1} s^{-1} reported for TFTs fabricated using them [78]. Typically, high mobility ($>10cm^2V^{-1}s^{-1}$) can be achieved in amorphous oxide systems, i.e., In_2O_3–Ga_2O_3 (a-IGO), Ga_2O_3–ZnO (a-GZO), In_2O_3–ZnO (a-IZO), and In_2O_3–Ga_2O_3-ZnO (a-IGZO). Transparent TFTs of this type are promising for a range of applications, such as backplanes for backlit liquid-crystal displays and for certain types of organic light-emitting diodes (OLEDs). This latter possibility has been demonstrated with TFTs consisting of zinc tin oxide (ZTO; 60 nm thick) as the semiconductor, ITO (R_{sheet}= 8 Ω/square) as the gate electrode, Al_2O_3/TiO_2 (ATO; 220 nm thick) as the gate dielectric, and Al-doped ZnO (AZO; R_{sheet}= 8 Ω /square) as the source and drain electrodes [79]. However, these devices were all relying on vacuum based pulsed laser deposition or sputtering techniques, which are considerably expensive and throughput is very low. The aim of this work is to obtain high performance thin film transistors by spin-coating method, while the cost is significantly reduced and the throughput can be increased tremendously at the same time.

1.5 Significance of this work

This work studies the ferromagnetic properties and field effect properties of ZnO thin films prepared by the same spin-coating method. By investigating the magnetic performance of un-doped and doped ZnO thin films by various tuning methods, assisted with various structure and electrical properties characterization, the puzzling mechanism of ferromagnetism in ZnO thin films has been complemented with new insights, which broadened the understanding of ferromagnetism in dilute magnetic oxides. A comprehensive mechanism has been initially put forward, although far from perfect. It is complementary to the previously proposed mechanism, but it is generalized into a more generalized form.

High mobility, low voltage ZnO based thin film transistors are fabricated. The active channel layer is prepared by a solution processing method, which required no high temperature annealing. Our devices show larger mobility than most of others ever obtained to date by solution processing without experiencing high temperature annealing, and they are comparable to other devices otherwise needing expensive vacuum based deposition techniques. A gate dielectric prepared by rarely reported spin-coating method is discovered, which can be seamlessly integrated with transparent ZnO channels. This finding would make significant impact on future transparent electronics.

Our study shows that carrier mediated ferromagnetism is not impossible in certain conducting regime, which suggests that ferromagnetism and field effect properties of ZnO thin films may be unified into spin field effect transistors. Although our study of field effect properties of ZnO thin films are simply charge based, it is highly expected that clues might be provided in future spintronic device investigation.

References

[1] S. Das Sarma, Am. Sci. 89, 516 (2001).

[2] S. A. Wolf, D. D. Awschalom, R. A. Buhrman, J. M. Daughton, S. von Molnar, M. L.Roukes, A. Y. Chthelkanova, D. M. Treger, Science 294, 1488 (2001).

[3] J. M. Kikkawa, D. D. Awschalom, Nature 397, 139 (1999).

[4] E. Svoboda, IEEE Spectrum 44, 15 (2007).

[5] H. Ohno, Science 281, 951 (1998); Physica B 376, 19 (2006).

[6] I. Zutic, J. Fabian, S. Das Sarma, Rev. Mod. Phys. 76, 323 (2004); S. Das Sarma, J. Fabian, X. Hu, I. Zutic, Superlattices Microstruct. 27, 289 (2000)

[7] M. N. Baibich, J. M. Broto, A. Fert, F. N. Vandau, F. Petroff, P. Ettenne, G. Creuzet, A. Friederich, J. Chazelas, Phys. Rev. Lett. 61, 2472 (1988).

[8] K. Sato and H. Katayama-Yoshita, Mat. Res. Soc.Symp. Proc. 666 (2001) F4.6.

[9] Y. Ohno, D. K. Young, B. Beschoten, F. Matsukura, H. Ohno and D. D. Awschalom, ibid.402 (1999) 790.

[10] R. Fiederling, M. Keim, G. Reuscher, W. Ossau, G. Schmidt, A. Waag and L. W. Molenkamp, ibid. 402 (1999) 787.

[11] C. Felser, G. H. Fecher, B. Balke, Angew Chem. Int. Ed. 46, 668 (2007).

[12] R. Ramesh, N. A. Spaldin, Nat. Mater. 6, 21 (2007).

[13] W. Eerenstein, N. D. Mathur, J. F. Scott, Nature 442, 759 (2006).

[14] M. Bibes, A. Barthelemy, IEEE Trans. Electron. Devices 54, 1003 (2007).

[15] A. H. Macdonald, P. Schiffer, N. Samarth, Nat. Mater. 4, 195 (2005).

[16] S. Pearton, Nat. Mater. 3, 203 (2004).

[17] G. A. Ozin, A. C. Arsenault, *Nanochemistry: A Chemical Approach to Nanomaterials*, The Royal Society of Chemistry, Cambridge, UK (2005).

[18] J. Wunderlich, B.G. Park, A. C. Irvine, L. P. Zârbo, E. Rozkotová, P. Nemec, V. Novák, J. Sinova, T. Jungwirth, Science, 24, 1801 (2010).

[19] T. Dietl, H. Ohno, F. Matsukura, J. Cibert, D. Ferrand, Science 287, 1019 (2000).

[20] S. A. Chambers, Surf. Sci. Rep. 61, 345 (2006); J. M. D. Coey, Curr. Opin. Solid State Mater. Sci. 10, 83 (2006); E. Senthil, S. Venkatesh, and M. S. R. Rao, Appl. Phys. Lett. 96, 232504 (2010)

[21] K. Ueda, H. Tabata, T. Kawai, Appl. Phys. Lett. 79, 988 (2001); W. G. Xie, F. Y. Xie, X. L. Yu, K. Xue, J. B. Xu, J. Chen, and R. Zhang, Appl. Phys. Lett. 95,

262506 (2009).

[22] R. Janisch, P. Gopal, N. A. Spaldin, J. Phys.: Conden. Matter 17, R657 (2005); C. Liu, F. Yun, H. Morkoc, J. Mater. Sci. 16, 555 (2005); R. K. Singhal, A. Samariya, S. Kumar, Y. T. Xing, D. C. Jain, S. N. Dolia, U. P. Deshpande, T. Shripathi, and E. B. Saitovitch, J. Appl. Phys. 107, 113916 (2010).

[23] Y. Matsumoto, M. Murakami, T. Shono, T. Hasegawa, T. Fukumura, M. Kawasaki, P. Ahmet, T. Chikyow, S. Koshihara, H. Koinuma, Science 291, 854 (2001).

[24] S. B. Ogale, R. J. Choudhary, J. P. Buban, et al. Phys. Rev. Lett. 91, 077205 (2003).

[25] J. Philip, A. Punnoose, B. I. Kim, Nature Mater. 5, 298 (2006), F. Jiang, X. Xu, J. Zhang, X. Fan, H. Wu, and G. A. Gehring, Appl. Phys. Lett. 96, 052503 (2010).

[26] C. Zener, Phys. Rev. 81, 440 (1951); Phys. Rev. 83, 299 (1951).

[27] P. Schattschneider, S. Rubino, C. Hebert, J. Rusz, J. Kunes, P. Novak, E. Carlino, M. Fabrizioli, G. Panaccione, G. Rossi, Nature 441, 486 (2006).

[28] K. Yosida, *Theory of Manetism*, Springer, Berlin, Germany, 1996.

[29] K. Sato, H. Katayama-Yoshida, Jpn. J. Appl. Phys. 39, L555 (2000).

[30] C. Zener, Phys. Rev. 82, 403 (1951); A. J. Millis, Nature 392, 147 (1998); A. J. Millis, P. B. Littlewood, B. I. Shraiman, Phys. Rev. Lett. 74, 5144 (1995).

[31] M. J. Calderon, S. Das Sarma, arXiv: cond-mat/0603182 (2006).

[32] A. Kaminski, S. Das Sarma, Phys. Rev. Lett. 88, 247202 (2002); A. C. Durst, R. N. Bhatt, P. A. Wolff, Phys. Rev. B 65, 235205 (2002); Z. L. Lu, H. S. Hsu, Y. H. Tzeng, F. M. Zhang, Y. W. Du, and J. C. A. Huang, Appl. Phys. Lett. 95, 102501 (2009).

[33] J. M. D. Coey, M. Venkatesan, C. B. Fitzgerald, Nature Mater. 4, 73 (2005); Phys. Rev. Lett. 93, 177206 (2004).

[34] T. Dietl, Nature Mater. 5, 673 (2006); K. Sato, H. Katayama-Yoshida, P. H. Dederichs, Jpn. J. Appl. Phys. 44, L 948 (2005).

[35] K. Sato, H. Katayama-Yoshida, Physica B 308, 904 (2001).

[36] E. C. Lee, K. J. Chang, Phys. Rev. B 69, 085205 (2004).

[37] Q. Wang, Q. Sun, B. K. Rao, P. Jena, Phys. Rev. B 69, 233310 (2004); Q. Wang, Q. Sun, P. Jena, Y. Kawazoe, Phys, Rev. B 70, 052408 (2004).

[38] S. J. Hu, S. S. Yan, M. W. Zhao, L. M. Mei, Phys. Rev. B 73, 245205 (2006).

[39] P. Gopal, N. A. Spaldin, Phys. Rev. B 74, 094418 (2006).

[40] C. H. Patterson, Phys. Rev. B 74, 144432 (2006).

[41] H. Katayama-Yoshida, K. Sato, T. Fukushima, M. Toyoda, H. Kizaki, V. A. Dinh, P. H. Dederichs, Phys. Stat. Sol. A 204, 15 (2007) and references therein.

[42] D. C. Kundaliya, S. B. Ogale, S. E. Lofland, Nature Mater. 3, 709 (2004); J. Y. Kim, J. H. Park, B. G. Park, Phys. Rev. Lett. 90, 017401 (2003); M. A. Garcia, M. Ruiz-Gonzalez, A. Quesada, Phys. Rev. Lett. 94, 217206 (2005).

[43] G. Kopnov, Z. Vager, R. Naaman, Adv. Mater. 19, 925 (2007); Z. G. Yin, N. F. Chen, Y. Li, X. W. Zhang, Y. M. Bai, C. L. Chai, Y. N. Xie, and J. Zhang, Appl. Phys. Lett. 93, 142109 (2008)

[44] A. C. Mofor, A. El-Shaer, A. Bakin, Appl. Phys. Lett. 87, 062501 (2005).

[45] D. W. Abrahm, M. M. Frank, S. Guha, Appl. Phys. Lett. 87, 252502 (2005).

[46] K. R. Kittilstved, W. K. Liu, D. R. Gamelin, Nat. Mater. 5, 291 (2006); K. R.Kittilstved, D. R. Gamelin, J. Appl. Phys. 99, 08M112 (2006); K. R. Kittilstved, N. S.Norberg, D. R. Gamelin, Phys. Rev. Lett. 94, 147209 (2005).

[47] X. F. Wang, J. B. Xu, N. Ke, J. G. Yu, J. Wang, Q. Li, H. C. Ong, R. Zhang, Appl.Phys. Lett. 88, 223108 (2006); Z. H. Zhang, X. Wang , J. B. Xu, S. Muller, C. Ronning and Q. Li, Nature Nanotechnology, 4, 523 (2009).

[48] X. F. Wang, J. B. Xu, B. Zhang, H. G. Yu, J. Wang, X. X. Zhang, J. G. Yu, Q. Li, Adv. Mater. 18, 2476 (2006); X. Wang, F. Song, Q. Chen, T. Wang, J. Wang, P. Liu, M. Shen, J. Wan, G. Wang, and J. Xu, J. Am. Chem. Soc. 132, 6492 (2010).

[49] X. F. Wang, J. B. Xu, W. Y. Cheung, J. An, N. Ke, Appl. Phys. Lett. 90, 212502 (2007).

[50] S. J. Pearton, D. P. Norton, M. P. Ivill, A. F. Hebard, J. M. Zarada, W. M. Chen, and I. A. Buyanova, Journal of Electronic Materials, Vol. 36, No. 4 (2007)

[51] S. J. Pearton, D. P. Norton, K. Ip, Y. W. Heo, T. Steiner, Prog. Mater. Sci. 50, 293 (2005); C. Klingshirn, Phys. Chem. 8, 782 (2007).

[52] M. H. Huang, S. Mao, H. Feick, H. Q. Yan, Y. Y. Wu, H. Kind, E. Weber, R. Russo, P. D. Yang, Science 292, 1897 (2001).

[53] G. R. Patzke, F. Krumeich, R. Nesper, Angew. Chem. Int. Ed. 41, 2446 (2002).

[54] A. Tsukazaki, A. Ohtomo, T. Onuma, Nature Mater. 4, 42 (2005).

[55] G. Ghosh, V. Sih, W. H. Lau, D. D. Awschalom, S. Y. Bae, S. Wang, S. Vaidya, G. Chapline, Appl. Phys. Lett. 86, 232507 (2005).

[56] T. Fukumura, Z. Jin, A. Ohtomo, H. Koinuma, M. Kawasaki, Appl. Phys. Lett.

75,3366 (1999).

[57] S. K. Mandal, A. K. Das, T. K. Nath, D. Karmakar, Appl. Phys. Lett. 89, 144105 (2006)..

[58] X. F. Wang, J. B. Xu, *Synthesis and Characterization of Transition-Metal-Doped Zinc Oxide Nanocrystals for Spintronics*, Ph. D Thesis of Electronic Engineering Department, The Chinese University of Hong Kong, 2007.

[59] Special issue on "*Macroelectronics*", Mater. Res. Soc. Bull.31 (6), 447 (2006).

[60] R. H. Reuss, B. R. Chalamala, A. Moussessian, M. G. Kane, A. Kumar, D. C. Zhang, J. A. Rogers, M. Hatalis, D. Temple, G. Moddel, B. J. Eliasson, M. J. Estes, J. Kunze, E. S. Handy, E. S. Harmon, D. B. Salzman, J. M. Woodall, M. A. Alam, J. Y. Murthy, S. C. Jacobsen, M. Olivier, D. Markus, P. M. Campbell, E. Snow, Proc. IEEE, 93, 1239 (2005).

[61] G. H. Gelinck, H. E. A. Huitema, E. van Veedendaal, E. Cantatore, L. Schrijnemakers, J. B. Putten, T. C. T. Geuns, M. Beenhakkers, J. B. Giesbers, B. H. Huisman, E. J. Meijer, E. M.Benito, F. J. Touwslager, A. W. Marsman, B. J. E. van Rens, D. M. Leeuw, Nature Mater. 3, 106 (2004).

[62] J. H. Cheon, J. H. Choi, J. H. Hur, J. Jang, H. S. Shim, J. K. Jeong, Y. G. Mo, H. K. Chung, IEEE Trans. Electron Devices 53, 1273 (2006).

[63] J. A. Rogers, Science 291, 1502 (2001).

[64] F. Eder, H. Klauk, M. Halik, U. Zschieschang, G. Schmid, C. Dehm, Appl. Phys. Lett.84, 2673 (2004); W. Lim, E. A. Douglas, D. P. Norton, S. J. Pearton, F. Ren, Y. W. Heo, S. Y. Son, and J. H. Yuh, Appl. Phys. Lett. 96, 053510 (2010).

[65] K. Cheng, M. H. Yang, W. W. W. Chiu, C.Y. Huang, J. Chang, T. F. Ying, Y. Yang, Macromol. Rapid Commun. 26, 247 (2005).

[66] V. C. Sundar, J. Zaumseil, V. Podzorov, E. Menard, R. L. Willett, T. Someya, M. E. Gershenson, J. A. Rogers, Science, 303, 1644 (2004).

[67] A. L. Briseno, R. J. Tseng, M. M. Ling, E. H. L. Falcao, Y. Yang, F. Wudl, Z. Bao, Adv. Mater. 18, 2320 (2006).

[68] R. F. Service, Science, 312, 1593 (2006); J. Liu, D. B. Buchholz, R. P. H. Chang, A. Facchetti, and T. J. Marks, Adv. Mater. 22, 2333 (2010); H. S. Kim, M.G. Kim, Y. G. Ha, M. G. Kanatzidis, T. J. Marks, and A. Facchetti, J. Am. Chem. Soc. 131, 10826 (2009).

[69] Y. Sun and J. A. Rogers, Adv. Mater. 19, 1897 (2007).

[70] P. K. Weimer, Proc. IRE 50, 1462 (1962).

[71] T. P. Brody, J. A. Asars, G. D. Dixon, IEEE Trans. Electron Devices, 20, 995 (1973).

[72] T. P. Brody, IEEE Trans. Electron Devices, 31, 1614 (1984); T. P. Brody, Proc. SPIE-Int. Soc. Opt. Eng. 1664, 2 (1992).

[73] D. V. Talapin, C. B. Murray, Science, 310, 86 (2005).

[74] D. B. Mitzi, L. L. Kosbar, C. E. Murray, M. Copel, A. Afzali, Nature, 428, 299 (2004).

[75] A. Pimentel, E. Fortunato, A. Gonçalves, A. Marques, H. Águas, L. Pereira, I. Ferreira, R. Martins, Thin Solid Films, 487, 212 (2005); A. Lu, J. Sun, J. Jiang, and Q. Wan, Appl. Phys. Lett. 96, 043114 (2010)

[76] I. D. Kim, Y. Choi, H. L. Tuller, Appl. Phys. Lett. 87, 043 509 (2005); M. Kimura, T. Kamiya, T. Nakanishi, K. Nomura, and H. Hosono, Appl. Phys. Lett. 96, 262105 (2010).

[77] E. Fortunato, A. Pimentel, L. Pereira, A. Gonçalves, G. Lavareda, H. Águas, I. Ferreira, C. N. Carvalho, R. Martins, J. Non-Cryst. Solids, 338–340, 806 (2004).

[78] K. Nomura, T. Kamiya, H. Ohta, K. Ueda, M. Hirano, H. Hosono, Appl. Phys. Lett. 85, 1993 (2004).

[79] P. Görrn, M. Sander, J. Meyer, M. Kröger, E. Becker, H.-H. Johannes, W. Kowalsky, T. Riedl, Adv. Mater. 18, 738 (2006).

Chapter 2 Characterization Techniques

2.1 Study approach

To study the magnetic properties and the mechanism behind spin-coated ZnO (un-doped or doped), we adopt the triangle approach as shown in Fig. 2-1-1 in this work. Firstly, we prepare zinc oxide (ZnO) thin films. Then we examine the magnetic properties to investigate whether they do satisfy the aimed properties or not. Furthermore, we carry out detailed microscopic and spectroscopic techniques, such as x-ray diffraction, x-ray photoelectron spectroscopy, Raman spectroscopy, and other advanced characterization techniques to investigate the mechanism responsible for the observed magnetic properties.
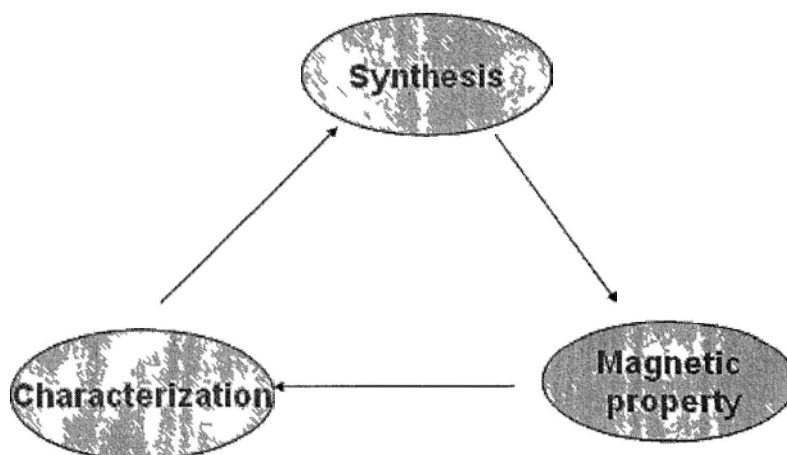
Fig.2-1-1 Schematic of study strategy adopted to investigate the magnetism of ZnO thin films

Before the detailed discussion, in this chapter, several important characterization techniques used in this work and their related physics are described in a concise way. They include magnetometry (superconducting quantum interference device magnetometer (SQUID)), x-ray photoelectron spectroscopy (XPS), Raman spectroscopy, photoluminescence and cathodoluminescence, etc.

2.2 Characterization techniques

2.2.1 Magnetometry

Magnetic susceptibility measurements are performed using a superconducting quantum interference device (SQUID, Quantum Design MPMS XL-7 Tesla) with a maximum sensitivity of $\sim 10^{-8}$ emu) magnetometer, which is the most sensitive device available for measuring magnetic fields. Before the sample measurement, the machine is accurately calibrated by a small piece of magnetic material having the known mass and magnetic susceptibility.

SQUID uses two Josephson junctions in a closed superconducting loop to detect extremely small changes of small current in external magnetic fields, allowing measurement of a sample with very small magnetic moment. The movement of the sample through superconducting detection pickup coils induces a current through the detection coils that forms a closed superconducting loop with the connecting wires and the SQUID input coil. The system makes use of a second order derivative coil configuration to eliminate effects of stray fields. The sample chamber is at low pressure of helium gas. SQUID is the most sensitive magnetometry technique available now [1]

In addition to magnetization-field (*M-H*) measurement, temperature dependent magnetization (Zero field cooling (ZFC) and field cooling (FC) conditions) in continuous mode is another important way to investigate the magnetic nature of samples. The nomenclature ZFC denotes the procedure of cooling the sample in zero field and measuring the magnetization upon warming up with the applied field on. The nomenclature FC denotes the procedure of cooling the sample in a specific applied field and measuring the magnetization with the field on. The net result of ZFC and FC measurement is the determination of the temperature range over which irreversibility in the magnetization exists. This range of irreversibility can also be seen by performing field-dependent magnetization (i.e., *M* vs. *H* loop) at varying temperature. If both hysteresis in the *M* vs *H* loop and a difference in the FC and ZFC traces can be observed, then the materials are deemed ferromagnetic. The occurrence

of the divergence in the ZFC-FC curves is simply due to the fact that the spins of the ferromagnetic materials tend to align with the easy crystalline axis and remain frozen in that direction at lower temperature. ZFC-FC has been recognized as a reliable technique that can indirectly detect any ultra-small magnetic nanoclusters in the DMS matrix, which otherwise could not be easily detected by usual characterization techniques [2, 3]. If there existed the ultra-small magnetic nanoclusters then they would have normally displayed the superparamagnetic behavior with a low blocking temperature [2,3]. When the particles are too small, the magnetic-anisotropy energy holding the particle becomes so small that the thermal energy becomes strong to cause it to demagnetize (randomize). So a collection of particles acts like a paramagnet. This phenomenon is known as superparamagnetism. T_B is defined as the peak temperature where the net moment of the system reaches a maximum (i.e., all spins align with the external applied field). Experimentally T_B can be determined by the peak in the conventional ZFC magnetization in a small field. More accurately, it should be determined by the magnetization curve where the remanence and coercivity reduce to zero. For example, Fig. 2-2-1 shows the typical ZFC-FC curves for Co nanoparticles with different sizes. The T_B increases with increasing particle size. Above T_B, ZFC and FC curves overlap and the superparamagnetism phenomenon takes place with evidence of neither remanence nor coercivity.
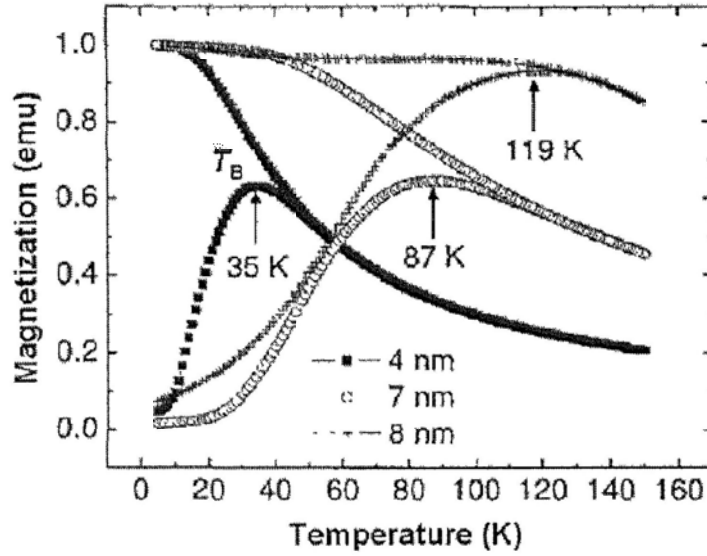
Fig.2-2-1 ZFC-FC curves of Co nanoparticles with different sizes in the applied external field of 50 Oe. The blocking temperature (T_B) is marked by arrows (Adapted from Ref. [4]).

2.2.2 X-Ray Photoelectron Spectroscopy (XPS)

XPS is a unique and non-destructive surface-sensitive technique to determine the chemical state, bonding environment, and elemental compositions in the surface (typically within 10 nm thickness) of the samples at the larger scale, which is a good complement to other technique. XPS works according to the principle of photoelectric effect, where an x-ray photon can knock out an inner electron from a core level of an atom, as seen in Fig. 2-2-2. The kinetic energy of emitted photoelectrons is defined as [5]

$$E_K = h\nu - E_B - \Phi \qquad (2-1)$$

where $h\nu$ is the energy of the photon, Φ is the work function of the spectrometer, and E_B is the binding energy of electron in the solid. Thus the binding energy becomes:

$$E_B = h\nu - \Phi - E_K \qquad (2-2)$$

where E_B is the binding energy of the orbital from which the electron is expelled.
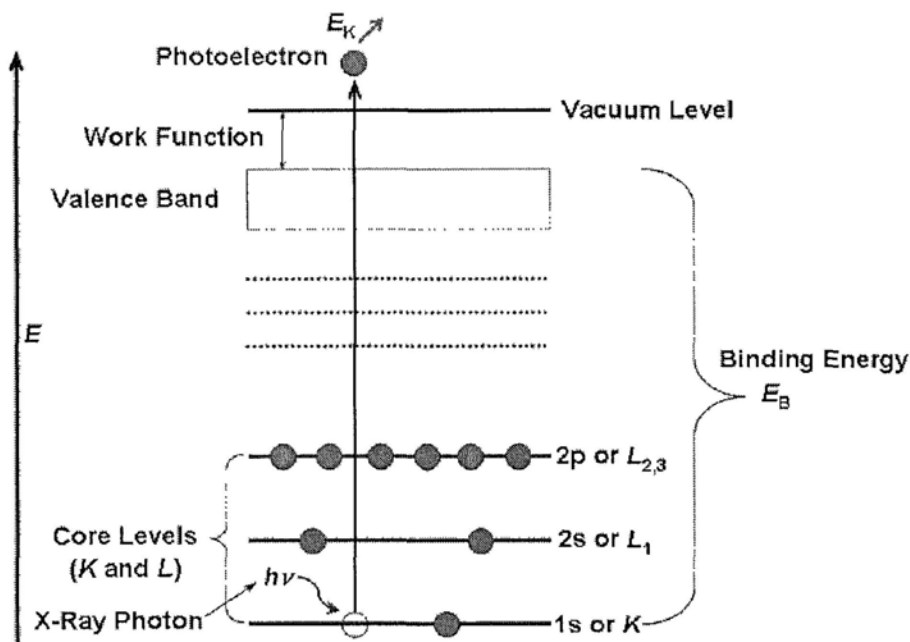
Fig.2-2-2 The schematic energy level diagram of the photoemission process. The L shell can be split into $L2$ and $L3$ levels as a result of spin-orbit coupling.

Since the kinetic energy of the outgoing electrons is measured and hv and Φ are known, E_B can be determined. Each E_B peak in the spectra corresponds to a different atomic orbital, therefore the formal oxidation state of the atom and the local chemical and physical environment can be obtained. Knowing the electron binding energy allows the identification of all elements except hydrogen since each element has its unique electron binding energy. The chemical shift of the binding energy can occur, which enables one to obtain information on chemical states from the variations in binding energies of the photoelectron. The relative surface concentrations of elements in the sample can be obtained by knowing the corresponding peak area A (number of photoelectrons per second in a peak) and the atomic sensitivity factor S. A general relevant expression for the atomic fraction of element x in a sample (C_x) is illustrated below:

$$C_x = \frac{n_x}{\Sigma n_i} = \frac{n_x / S_x}{\Sigma A_i / S_i} \tag{2-3}$$

where n_x is the number of atoms of element x per cm^3 of the sample. A software package can be used to obtain the relative concentrations of each element contained in

the sample. Usually the detection limit is in the range of 0.1 % –1 % dependent on the elements to be detected. The analysis area is usually at a few hundred micrometers, and the depth profile is about 5~10 nanometers in the surface due to the short mean free path of the emitted photoelectrons.

2.2.3 Micro-Raman Spectroscopy

Raman scattering spectroscopy is a fast and nondestructive tool to investigate the microscopic structure, topological disorder, and the influence of impurity doping on the host lattice dynamic properties. It could give an alternative perspective on the possible existence of secondary phase in the DMS host materials that may be not detectable by the usual characterization techniques such as x-ray diffraction (XRD). In this work, Raman spectroscopy is performed at room temperature using a micro-Raman spectrometer (Renishaw InVia) with a 514.5 nm (2.4 eV) Ar+ laser as an excitation source in the backscattering geometry. The laser power is kept low enough to avoid heating the sample by optical filtering and/or defocusing the laser beam in the samples. The incident laser power on the samples is estimated to be below 10 mW. The spectra are performed in the frequency range of 100–900 cm^{-1} with a spectral resolution of about 1 cm^{-1} and the scattered photons are collected by a liquid-nitrogen-cooled CCD detector. The wave number shift resolution is estimated to be better than 0.5 cm^{-1}. The laser spot size on the samples is 1–2 μm in diameter within 1 μm depth. In this case, while inhomogeneity in the Raman spectra on the micron scale or larger may not directly provide the signature of the secondary phases, it does indicate a nonuniform sample that is therefore less desirable for the detailed magnetic characterization. In order to obtain a good signal-to-noise ratio, small slits and long integration times are used. We collected spectra from three different locations of the same sample and we presented the representative one. All the spectra obtained are calibrated with the reference single-crystal silicon line centered at 520 cm^{-1} and normalized to the incident photon flux.

2.2.4 Other Characterization Techniques

I. X-Ray Diffraction (XRD)

XRD is a nondestructive technique that can provide crystallographic information from a relative larger area of the sample compared with TEM. It is an initial screening for the presence of secondary phases if existed in the DMS host lattice. Its sensitivity is usually lower than 1 %, so it may not be good enough to identify minute amounts of secondary phases or nominal contamination. Thin film XRD patterns are obtained from a Bruker D8 Advance X-ray diffractometer (Cu K_α radiation, $\lambda = 1.5406$ Å) in the α-2θ geometry. The samples are mounted in the XRD sample holder and run at room temperature for a period of around 3 hours with the x-ray generator operated at a power of 40 kV and 40 mA. The scan rate used depended on the thickness of the sample, sample, and data are typically collected for 2θ values ranging from 20° to 80° by solving Bragg's Law.

II. Scanning Electron Microscopy (SEM)

SEM is capable of producing high-resolution images of the sample surface structure and cross-section view. The morphology and qualitative analysis of elements in samples are acquired from SEM (LEO 1450VP). This instrument is coupled with an energy dispersive x-ray spectroscopy (EDX) detector. When energetic electron beam is incident on the sample, x-rays are generated that are characteristic of the elements present in the sample, allowing one to identify and roughly quantify the elemental species. The accelerating voltage for the scans is 15 kV.

III. Atomic Force Microscopy (AFM)

Atomic force microscopy (AFM) or scanning force microscopy (SFM) is a very high-resolution type of scanning probe microscopy, with demonstrated resolution on the order of fractions of a nanometer, more than 1000 times better than the optical diffraction limit [6].

The AFM consists of a cantilever with a sharp tip (probe) at its end that is used to scan the specimen surface. The cantilever is typically silicon or silicon nitride with a

34

tip radius of curvature on the order of nanometers. When the tip is brought into proximity of a sample surface, forces between the tip and the sample lead to a deflection of the cantilever according to Hooke's law. Depending on the situation, forces that are measured in AFM include mechanical contact force, van der Waals forces, capillary forces, chemical bonding, electrostatic forces, magnetic forces, Casimir forces, solvation forces, etc. Along with force, additional quantities may simultaneously be measured through the use of specialized types of probe. Typically, the deflection is measured using a laser spot reflected from the top surface of the cantilever into an array of photodiodes. Other methods that are used include optical interferometry, capacitive sensing or piezoresistive AFM cantilevers. These cantilevers are fabricated with piezoresistive elements that act as a strain gauge. Using a Wheatstone bridge, strain in the AFM cantilever due to deflection can be measured, but this method is not as sensitive as laser deflection or interferometry.

The AFM can be operated in a number of modes, depending on the application. In general, possible imaging modes are divided into static (also called contact) modes and a variety of dynamic (or non-contact) modes where the cantilever is vibrated. In our study, AFM, DI Nanoscope 3 in contact mode is used to observe the surface of the thin film.

IV. Inductively Coupled Plasma–Mass Spectrometry (ICP–MS)

In order to examine the nominal possible amount of ferromagnetic impurities, the sample composition is scrutinized by ICP–MS (ELAN DRC-e, PerkinElmer, US). The sample is soaked in the nitric acid solution to completely dissolve the thin film. The detection limit of ICP-MS is on the order of ppb (part per billion).

V. Micro-Cathodoluminescence (CL)

The luminescence properties of the samples are measured by a CL spectrometer. CL is a phenomenon of optical and electrical interaction, where a beam of electrons generated by an electron gun impacts on a material and causes it to emit UV, visible and infrared light according to the electronic structure of the material due to the

recombination of generated electron-hole pairs. A Cambridge S-360 SEM equipped with a tungsten filament is used to perform the CL experiments. The accelerating voltage of the primary electron beam is set at 10 kV, and the probe current is set at 5 nA. Whenever the electron beam irradiated the sample, the electron beam is scanned for a rectangular pattern with area according to the magnification of the SEM. The CL emitted from the sample is collected by a parabolic mirror and the collected light is directed to an Oxford Instruments MonoCL2 spectrometer system for analysis. The monochromatic light passing through the spectrometer is detected by the CCD detector.

VI Photoluminescence Spectroscopy (PL)

Photoluminescence is a process in which a substance absorbs photons (electromagnetic radiation) and then re-radiates photons. Quantum mechanically, this can be described as an excitation to a higher energy state and then a return to a lower energy state accompanied by the emission of a photon. This is one of many forms of luminescence (light emission) and is distinguished by photoexcitation (excitation by photons), hence the prefix photo-. The period between absorption and emission is typically extremely short, on the order of 10 nanoseconds. Under special circumstances, however, this period can be extended into minutes or hours.

Ultimately, available energy states and allowed transitions between states (and therefore wavelengths of light preferentially absorbed and emitted) are determined by the rules of quantum mechanics. A basic understanding of the principles involved can be gained by studying the electron configurations and molecular orbitals of simple atoms and molecules. In this work, PL is used to study the defect scenario in ZnO thin films. We utilize Jobin Yvon HR（High resolution）800UV with the light source of He-Cd 325 nm.

2.3 Summary

This chapter briefly introduces the principles, applications and characteristics of the techniques that are utilized to investigate the inter-relationship of composition, structure and magnetic performance of ZnO thin films.

References

[1] D. Jiles, *Introduction to Magnetism and Magnetic Materials*, Chapman and Hall, USA, 1998.

[2] J. L. Dormann, D. Fiorani, E. Tronc, Adv. Chem. Phys. 98, 283 (1997).

[3] M. Jamet, A. Barski, T. Devillers, Nat. Mater. 5, 653 (2006).

[4] R. K. Zheng, H. Gu, B. Xu, X. X. Zhang, Phys. Rev. B 72, 014416 (2005).

[5] J. F. Moulder, W. F. Stickle, P. E. Sobol, K. D. Bomben, *Handbook of X-ray Photoelectron Spectroscopy* (Ed: J. Chastain), Perkin-Elmer, Eden Prairie, MN,1992.

[6] D. K. Schroder, *Semiconductor Materials and Device Characterization*, Wiley-IEEE Press, 3rd edition, 2006.

Chapter 3 Ferromagnetism of Un-doped ZnO Thin Films

3.1 Introduction

Transition metal (TM) doped ZnO materials have attracted considerable attention due to their potential applications in spintronics, as Dietl *et al.* theoretically predicted that room temperature ferromagnetism (RTFM) could be realized in ZnO-based magnetic semiconductors [1]. However, the mechanism of ferromagnetism in ZnO-based materials is increasingly controversial, with the co-existence of favoring carriers [2-4] or defects, including zinc vacancies [5], zinc interstitials [6,7], and oxygen vacancies [8,9], H impurities [10], etc.

In addition to TM doped ZnO [11,12], there are reports that intrinsic RTFM has also been found in un-doped ZnO nanostructures, either in thin films [13,14], nanoparticles [15] or nanowires [16]. The necessity of magnetic doping to form ferromagnetism in oxide is still under discussion [17-19]. With the absence of magnetic ions, the saturation magnetization moment ranged from several thousandths of emu/g to tens of emu/g. Xu *et al.*[13] attributed the ferromagnetic origin to zinc vacancies, while Banerjee *et al.* [20] claimed the oxygen vacancy (F^+ centers) clusters as the primary contributor. Sundaresan *et al.* [21] even generalized the ferromagnetic performance to be a universal feature of un-doped oxide nanoparticles. Theoretically, Wang *et al.* [22] concluded that the FM is due to zinc vacancies, whereas Sanchez *et al.* [23] found the local spin-polarization induced at the O atoms with dangling bonds at the surface. Recently, by first principles calculation, E. Liu *et al.* [24] concluded that it is oxygen vacancies rather than electrons that mediate the spin-spin interaction in Co-doped ZnO. R. Podila *et al.* attributed the origin to be oxygen p orbital, where the dynamic exchange between O_2 and O- leads to FM coupling [25]. The unique properties of $2p$ states has been ascribed to the intrinsic origin of ferromagnetism in both oxides and nitrides, provided that the threshold hole concentration is achieved,

whether it is magnetically doped or not [26]. Further discussion could be found in [27-29]. However, due to the poor detection limit of normal characterization techniques (XRD or XPS, etc.) used in previous work, it is often difficult to exclude magnetic impurities and to claim an intrinsic RTFM. Meanwhile, experimental evidence supporting the defect origin is limited. The defects in ZnO can be indirectly investigated by electrical characterization and spectroscopic characterization. Systematic evidence provided by these techniques to examine the defect origin of RTFM in ZnO is still quite scarce. In this chapter, results are presented which support the intrinsic nature of RTFM in un-doped ZnO thin films, and details about the defect change observed in different treatment processes are studied by electrical measurement and photoluminescence spectroscopy. Without magnetic doping, the question becomes much simpler. Phase segregation presumably accompanying with the doping process can be easily ruled out.

3.2 Preparation and characterization

ZnO thin film is prepared by spin-coating method in the following conditions. Zinc acetate (Zn（CH$_3$COO$_2$, 99.99 %) is dissolved (concentration: 0.7 M) in 2-methoxyethanol (99.9 %), with monoethanolamine (MEA, 99.5 %) as the stabilizer. A homogeneous solution is obtained after stirring the mixture for 2 hours at 60 °C. The molar ratio of zinc acetate to MEA is kept at 1: 2. The sol is spin coated onto 1 cm × 1 cm Si (100) substrate at 3000 rpm for 30 seconds. Before spin-coating, the substrate is ultrasonically washed consecutively by DI water, ethanol, and acetone for 30 minutes respectively. The precursor films are preheated at 300 °C for 10 minutes to evaporate the organics. This coating and preheating process is repeated several times until the desired thickness (~ 120 nm, confirmed by surface profiler). This process is schematically shown in Fig. 3-2-1. The as-prepared thin films are further treated by rapid thermal annealing (RTA) under N$_2$, O$_2$, and Ar (with purity of 99.99 %) ambient for 1 minute at about 680 °C. Before investigating the magnetic properties, the composition, structure and surface morphology are examined by SEM, AFM, XRD and XPS characterization measurements. Results of representative ZnO thin films annealed in O$_2$ are shown here. The difference of annealing ambient makes no significant impact on these properties.
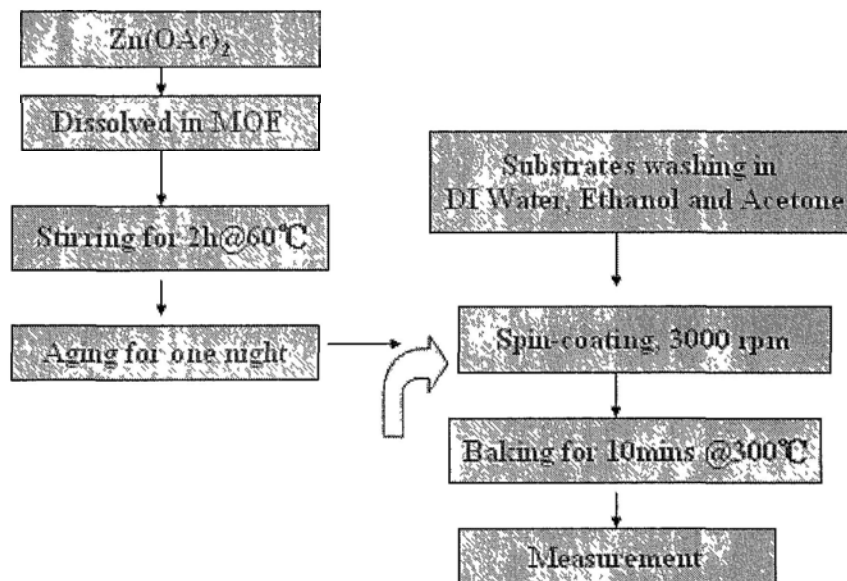
Fig.3-2-1 Schematic flow chart showing the preparation process.

The surface and cross section of ZnO is shown in Fig.3-2-2 by SEM.
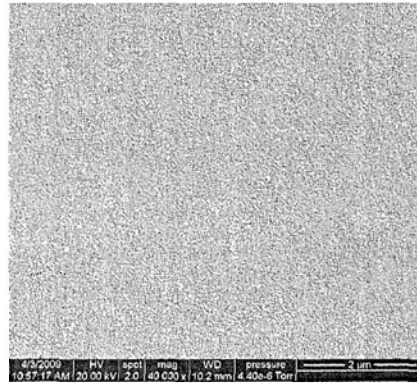
Fig.3-2-2 Surface morphology of spin-coated ZnO thin films by SEM.
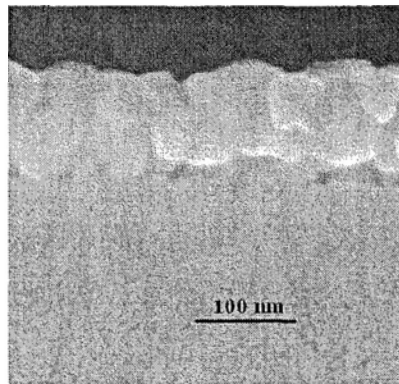
Fig.3-2-3 Cross section view of ZnO thin films on Si substrate.

It can be observed that the thin film is very uniform in a large area. The thickness estimated from the cross section view agrees very well with that obtained by surface profiler. The size of the particle is approximately 30 nm.

The surface roughness of the ZnO thin films is observed by AFM, as shown in Fig.3-2-4.
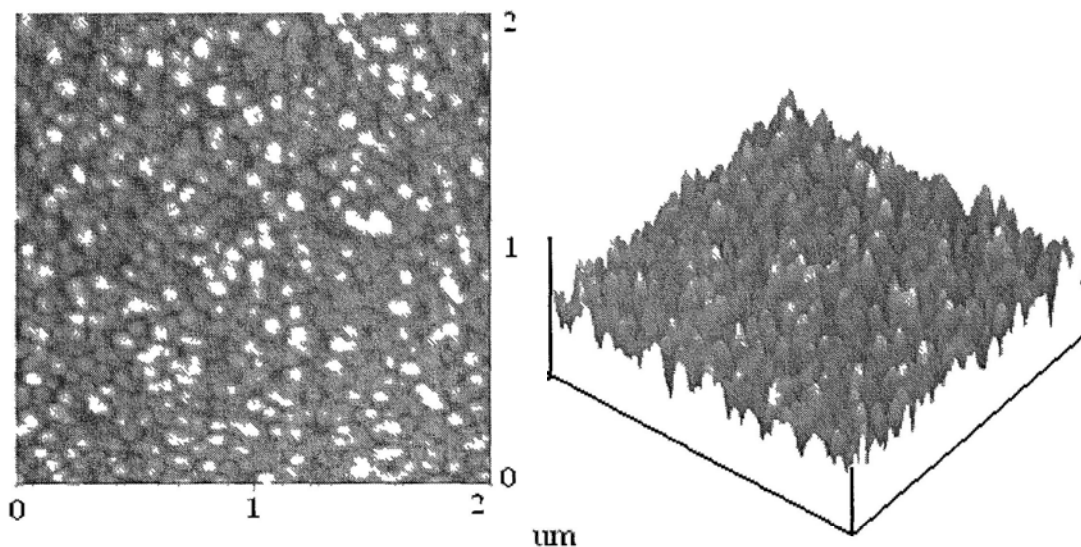
Fig.3-2-4 Surface morphology of ZnO thin films.

High quality polycrystalline thin films are obtained. The root-mean-square surface roughness in 2×2 μm^2 scan area is close to 5 nm. The grain size can be estimated to be $30 \sim 50$ nm.

Fig.3-2-5 shows the XRD pattern of the same ZnO thin film. The wurtzite structure of polycrystalline ZnO can be clearly found, and no impurity phase has been observed within the detection limit. The preferential growth direction is along c-axis.
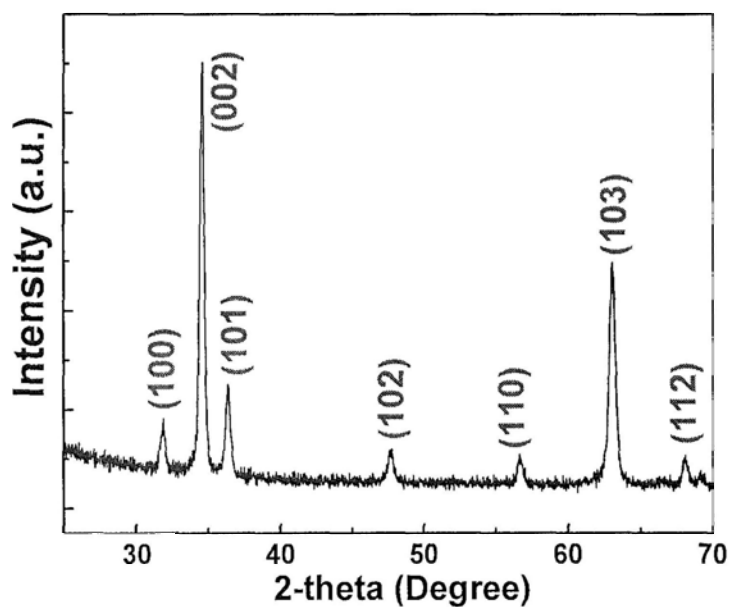
Fig.3-2-5 XRD pattern of ZnO thin film annealed in O_2.
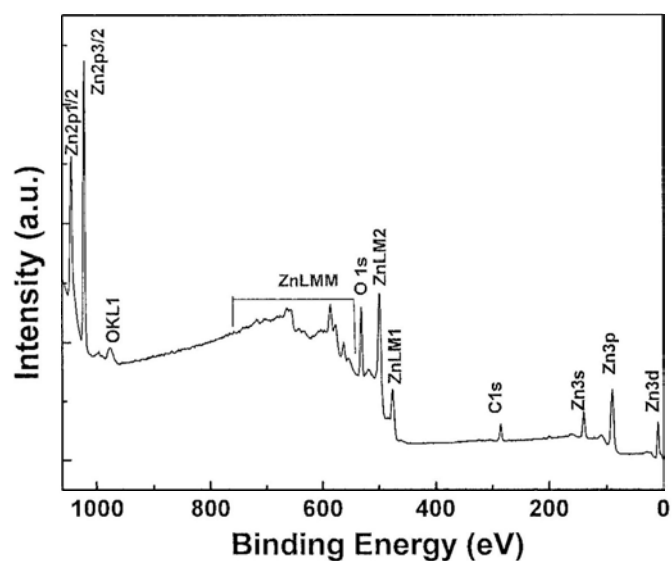
Fig.3-2-6 XPS spectrum of un-doped ZnO thin film (survey scan).
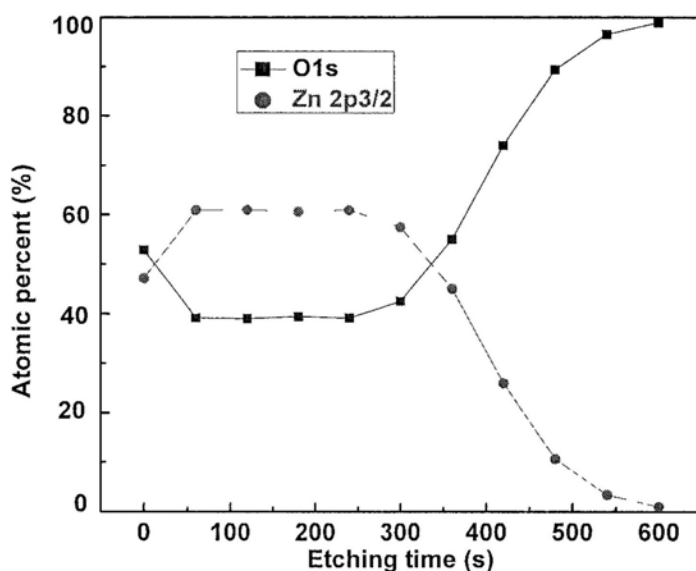
Fig.3-2-7 XPS depth profile of un-doped ZnO thin film.

The elemental composition is investigated by XPS, as demonstrate in Fig.3-2-6 and Fig.3-2-7. It is found that no ferromagnetic metal related species are present in the sample down to the detection limit of 0.1 %. In order to check the interior of the thin film, the depth profile is performed. The etching speed is about 15 nm per minute. Again, the thickness can be roughly estimated to be close to 100 nm, in agreement with previous findings by other technique. The composition of the inner side is

identical to that in the surface, which implies that the prepared thin film is homogeneous across the whole depth direction. Only Zn and O are detected. The oxygen deficient non-stoichiometry is clearly demonstrated before the removal of the thin film. The increase of oxygen at the tail is ascribed to the thin silicon dioxide layer on the Si substrate.

To thoroughly determine the concentration of unintentionally introduced impurities (for example, from the starting chemical agents, washing solutions, annealing environment, or even from the handling tools), which is beyond the detection of XPS, we choose several samples prepared by following the identical conditions and handled with identical tools to perform ICP-MS measurement. The sample is soaked in the nitric acid solution to completely dissolve the thin film. The mass of the thin film is calculated by comparing the mass loss before and after the soaking of the sample. The sample results show only the presence of Ni with a concentration much smaller than 10^{-6}, and no other metal elements including Fe and Co are detected.

3.3 Magnetic properties

To avoid the magnetic interference from the substrate, a clean substrate undergoes all the handling process (washing, preheating, annealing and cutting) except spin-coating and is measured by SQUID. This test is repeated for several blank substrates. The applied magnetic field is parallel to the thin film surface, which is the default direction in the magnetization measurement in the present study unless specifically stated. Fig.3-3-1 shows the diamagnetic behavior, which ensures that there is no ferromagnetic impurity inside and in the air-bearing surfaces of the substrate.
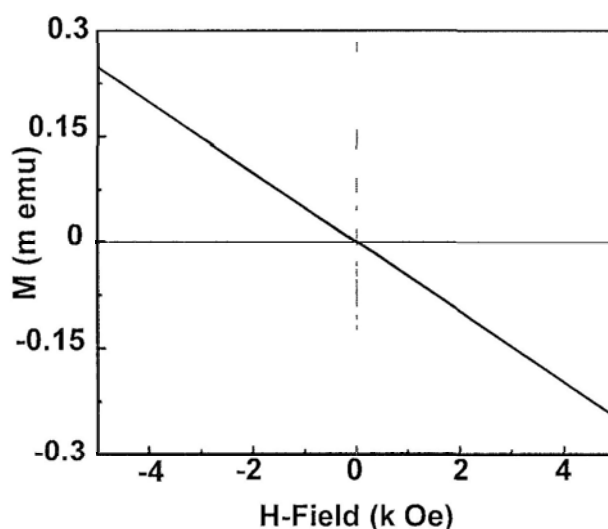
Fig.3-3-1 Diamagnetic behavior of the clean substrate after washing.

In Fig.3-3-2, we show the zero field cooling (ZFC) and field cooling (FC) magnetization curves for the as-prepared thin film. For ZFC, the sample is cooled down to 5 K in the absence of magnetic field, and the data are collected while warming up to 300 K in the field of 500 Oe. The FC data are taken while warming up the sample after cooling it down to 5 K in the presence of 500 Oe. For the FC curve, as the temperature increases, due to thermal energy, the frozen magnetic moments may become randomized, as a result, the magnetization decreases [20]. The separation between these two curves, although quite small (on the order of 10^{-7} emu, and the machine we used has the detection limit of 2×10^{-8} emu), demonstrates the

ferromagnetic properties of the un-doped thin film. There is no superparamagnetism observed.
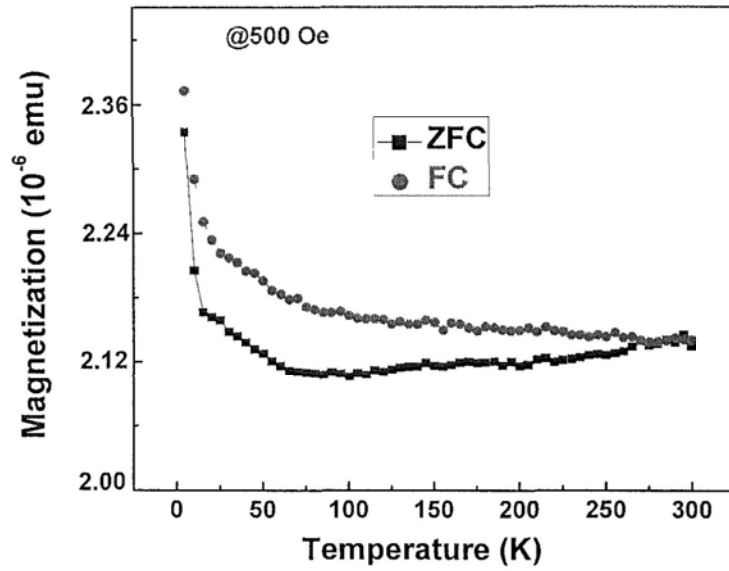
Fig.3-3-2 ZFC and FC curves for the as-prepared ZnO thin film.

The magnetization dependence on field (*M* versus *H*) of the as prepared ZnO thin film is measured at 300 K and 5 K, respectively. The result is shown in Fig.3-3-3. It is noticeable that the saturation magnetization moment only increases moderately (corresponding to the small increase of magnetization in Fig.3-3-2) with the decrease of temperature, which is consistent with the defect nature of the weak ferromagnetism in ZnO film as discussed below. These results are in good agreement with the reported finding for ferromagnetism in pure ZnO nanostructure [13].
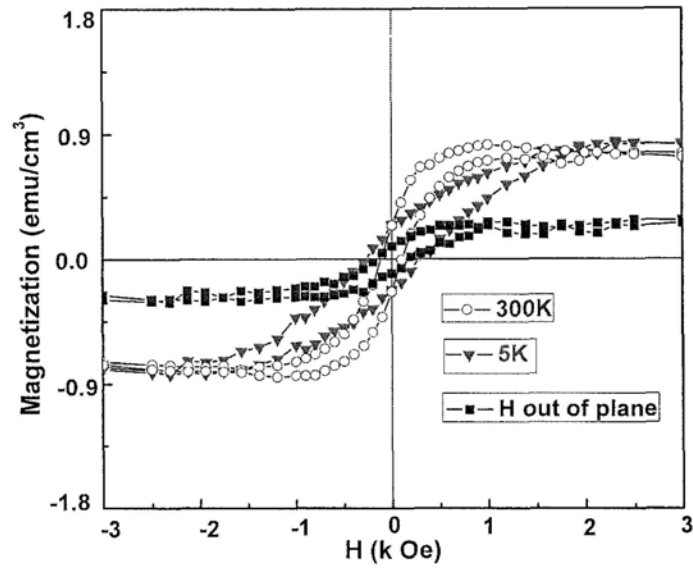
Fig.3-3-3 In-plane room temperature (300 K, circle) and low temperature (5 K, triangle) hysteresis loops for as-prepared ZnO thin film; Black curve (in square) is for H normal to the film at room temperature.

The hysteresis loop at room temperature for the same sample when the field is applied normal to the film (out-of-plane direction) is also shown in Fig.3-3-3. Compared to the in-plane loop, the out-of-plane saturation magnetization moment (Ms) decreases almost by half. The magnetic moments in the film have the tendency to fix along certain directions. This large anisotropy corroborates the claim that the ferromagnetism might come from defects, because it is usually supposed that defects cannot be symmetrically magnetic [30]. It may also eliminate the possibility of explaining the magnetization in terms of the segregated ferromagnetic impurities in the thin films [31].

To investigate the magnetic performance of the un-doped ZnO thin films, an as-prepared sample is cut identically into four pieces, three of which are annealed in N_2, O_2 and Ar, respectively. These four pieces are measured by SQUID, with the results shown in Fig.3-3-4. Clear M-H loops can be observed. The unit volume M_S for the as-prepared thin film is close to 1 emu/cm^3, which agrees very well with other reported results of un-doped ZnO [13,14,16]. The diamagnetic nature of the substrate has been shown previously. As aforementioned, by ICP-MS characterization, the only

48

possible impurity concentration of Ni is much smaller than 10^{-6}, through calculation (maximum: $10^{-10} \sim 10^{-9}$ emu), Ni and its compounds obviously cannot be responsible for the measured total magnetization (on the order of 10^{-6} or close to 10^{-5} emu, film size: 5 mm × 5 mm × 120 nm). Therefore, it can be concluded that the observed room temperature ferromagnetism (RTFM) of the ZnO thin film is an intrinsic behavior rather than from any other ferromagnetic impurities.
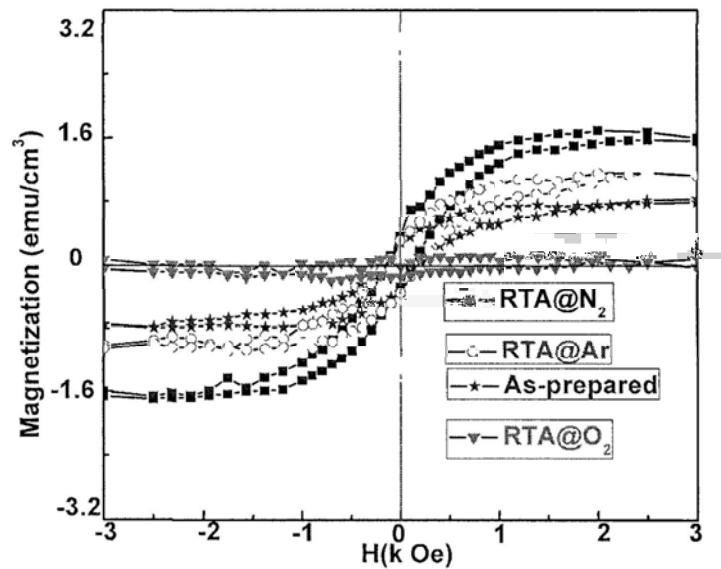
Fig.3-3-4 Hysteresis loops for the as-prepared and annealed samples in N_2, O_2 as well as Ar, respectively at room temperature.

As widely known, oxygen vacancy V_O is easily generated under vacuum or inert gas in ZnO:

$$O^{2-} \rightarrow O + Vo + 2e^{-} \qquad (3\text{-}1)$$
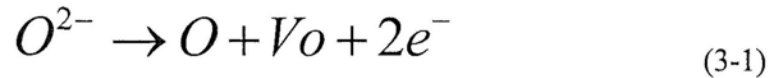
The generated O atoms are very oxidative. Therefore, it is expected that an oxidative ambient can suppress the generation of V_O, while a reducing condition will facilitate the creation of oxygen vacancies, which may make the resistance of ZnO annealed in N_2 smaller than in O_2 [32]. The annealing effect on oxygen vacancy concentration has been reported before [33]. This may explain the different enhancement effects for M_S by N_2 and Ar annealing. The Ar annealing effect is similar to the vacuum annealing,

which has been reported to enhance the M_S in ZnO [34]. However, because of the smaller electron negativity of N compared to O, N_2 annealing may facilitate the creation of oxygen vacancy compared with Ar. The difference between N_2 annealing and O_2 annealing treatments for the as-prepared sample may help to exclude Zn interstitial and other ferromagnetic metal species as the major origin for FM. Hence, it is more reasonable to speculate that the above mentioned magnetic behavior change results from the alteration of oxygen vacancy under different annealing conditions. This oxygen vacancy change could be further supported by optical and electrical characterization as discussed below.

Fig.3-3-5 shows the photoluminescence spectra for the identically annealed samples, in which the typical near-band edge peak at around 374 nm for ZnO can be seen. In addition, a broad peak centered at 500 nm is present, which is widely regarded as originating from the oxygen vacancy defect [32,35,36], although some disagreement exists [37]. For eye guidance, the parts around 500 nm for as-prepared thin film and O_2 annealed one are zoomed in, as shown in the inset in the middle. Normally the relative intensity ratio of peak at 500 nm to peak at 374 nm (simply denoted as intensity ratio hereafter) provides a bench mark of oxygen vacancy concentration [35], which is summarized in Fig.3-3-6. It could be found that the evolution trends for intensity ratio and the correspondent M_S are identical. Namely, M_S increases with the oxygen vacancy concentration.
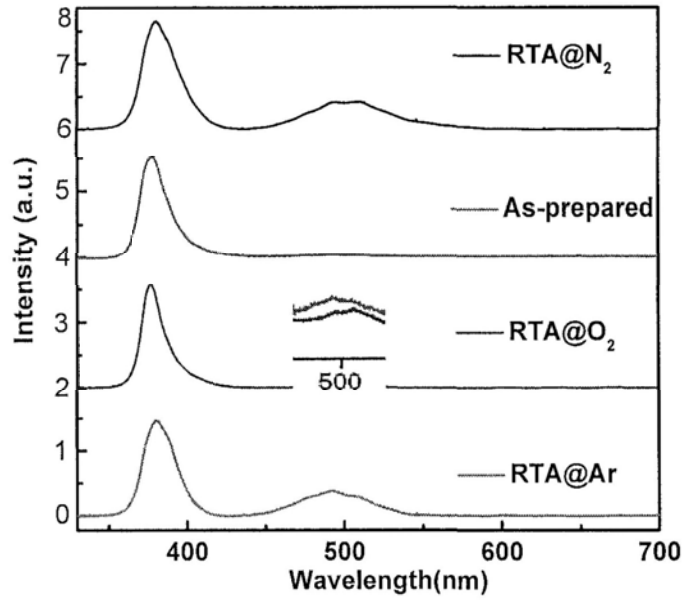
Fig.3-3-5 Room temperature PL spectra for as-prepared and annealed samples in N_2, O_2, and Ar, respectively; Inset: zoomed in parts around 500nm for as-prepared and the O_2 treated samples

The resistivity evolution under identical annealing treatments is also shown in Fig.3-3-6. Oxygen vacancy is one major type of donor defects in ZnO-based semiconductors [38,39]. As pointed out by Tatsumi *et al.* [40], the increase and decrease of electron concentration in un-doped ZnO is ascribed to the generation and reduction of oxygen vacancy. Theoretical calculations also indicated that oxygen vacancies produce shallow donor states [41]. It is worth noting that the resistivity evolution does not exactly follow the M_S alteration. Due to the improved lattice order, and hence reduced lattice scattering, the O_2 treated thin film demonstrates smaller resistivity, although the oxygen vacancy concentration (donor concentration) is smaller than that in the as-prepared sample. Under the same annealing temperature for the identical time duration, the resistivity and M_S change accordingly. The resistivity change reflects the oxygen vacancy concentration variation, although the carrier concentration is not necessarily equal to the oxygen vacancy concentration [33, 35]. The consistency between M_S and oxygen vacancy suggests the significant role of oxygen vacancy in inducing the FM in pure ZnO thin film.
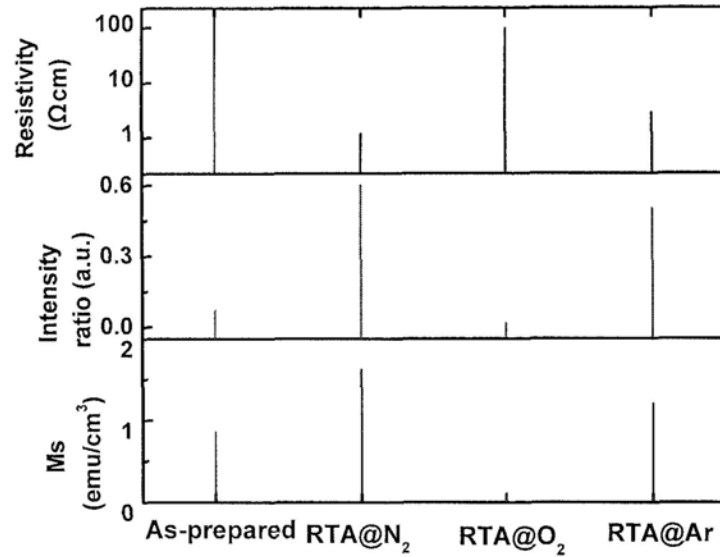
Fig.3-3-6 *Ms*, PL intensity ratio and resistivity variations for as-prepared and annealed samples in N_2, O_2 and Ar, respectively.

In order to provide more evidence to support the role of oxygen vacancies, another experiment is designed. The as-prepared ZnO thin film is first annealed in N_2, then in O_2 and finally in N_2 again .The annealing temperature is always kept at 680 °C and the time duration is 1 minute as aforementioned. After each annealing, the *M-H* curve is collected at room temperature (the magnetic field is parallel to the film surface, the same as previous measurement). The results showing well-defined *M-H* loops are presented in Fig.3-3-7. The unit volume saturation magnetization moment is quite consistent with that in previous measurement, revealing a good reproducibility. It can be clearly observed that the saturation magnetization increased with N_2 annealing, then diminished with O_2 annealing and then re-enhanced in N_2 annealing. The diamagnetic substrate is unlikely to account for the observed ferromagnetism.
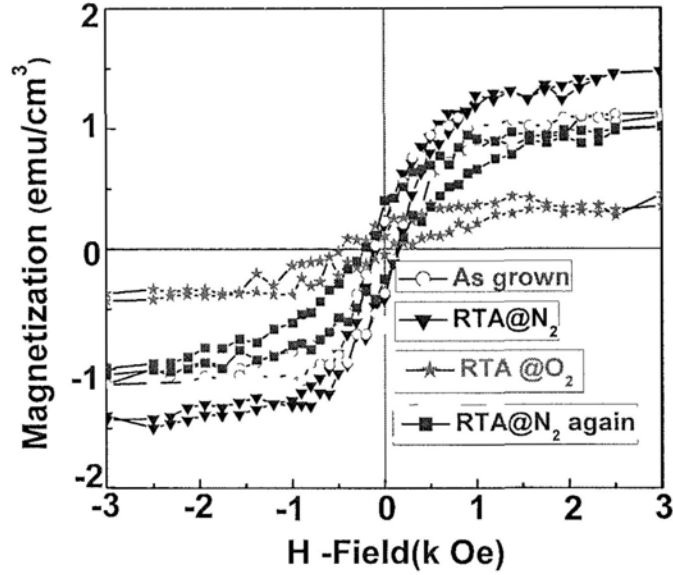
Fig.3-3-7 Hysteresis loops for ZnO thin film with sequential annealing.

This exactly proves the proposed mechanism of oxygen vacancy induced ferromagnetism. Similarly, more characterization measurements are performed to observe the alteration of the structure or properties to affirm the assumption.

The annealing effect on oxygen vacancy could find support in the Raman spectra as well, as shown in Fig.3-3-8, where Raman spectra of samples annealed in O_2 and N_2 in addition to the blank substrate are presented. Most of the peaks (including the highest one near 500 cm $^{-1}$) are mixed with those from the substrate except the one at around 438 cm^{-1}, which is the characteristic peak for wurtzite ZnO (E_2^{High}), and is mainly describing the vibration mode of oxygen atoms [42]. The peak broadening is related to the defects. Through analyzing the full width at half maximum (FWHM) variation of different vibration mode corresponding to specific atoms, details about the defect could be obtained. As shown in Fig.3-3-8 (b), it is obvious that the FWHM for the one annealed in O_2 is the smallest, the widest for the as grown one and the one annealed in N_2 shows
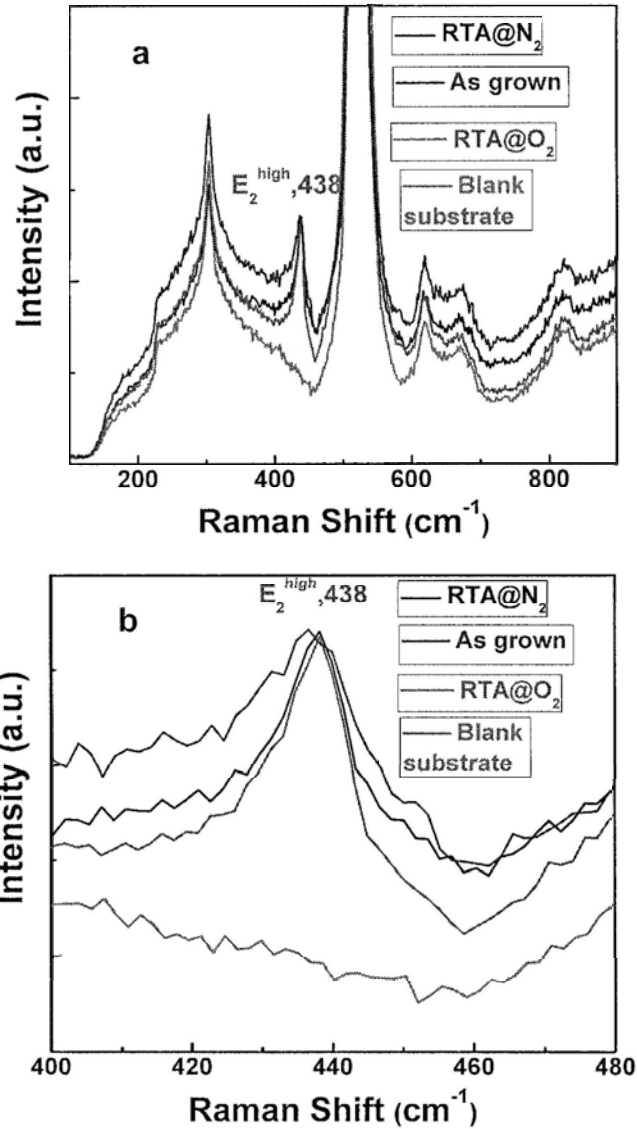
Fig.3-3-8 Original (a) and locally enlarged (b) Raman spectra of the substrate, as-grown and annealed ZnO films.

medium broadening. The one annealed in O_2 is the closest to the perfect structure in its stoichiometry, because the density of oxygen vacancy is reduced significantly. Annealing in N_2 renders the peak broaden to some extent because of the creation of abundant oxygen vacancies. The largest peak broadening for the as-grown sample is probably due to the much abundance of disorder without high temperature annealing.

To study the oxygen vacancy variation in the above process, cathodoluminescence spectroscopy is performed after each annealing. The result is shown in Fig.3-3-9. In addition to the typical peak at around 370 nm corresponding to the band emission of

ZnO, a broad peak centering at 520 nm could be found once the sample is annealed in N_2, and almost diminished in O_2 annealing. This green emission peak is widely attributed to the oxygen vacancy defect, whose intensity could serve as a barometer for us to study the variation of oxygen vacancy [32, 35]. From Fig.3-3-9, it can be seen that the concentration of oxygen vacancy increases in N_2 annealing, and decreases in O_2 annealing, and then increases again in the second-time N_2 annealing, which synchronizes the change of the magnetic performance in the same process, therefore the CL results proved the above-proposed role of oxygen vacancies. It is noted that in the as-grown piece, the green emission is slightly low, unexpected from the results of *M-H* loops. This might be because the lattice disorder reduces the emission efficiency or increases the scattering of generated photons without annealing at higher temperature.
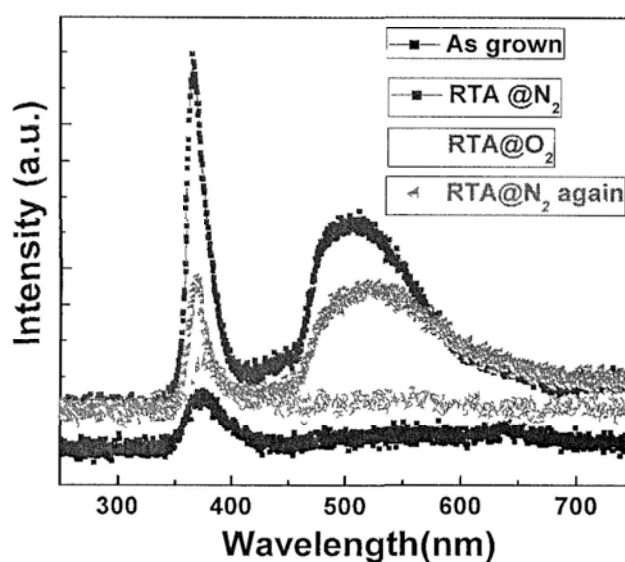
Fig.3-3-9 CL spectra for films annealed in sequence.

From previous discussion, it is expected that the electrical performance might also exhibit such a reversible behavior following the above mentioned oxygen vacancy alteration in the annealing sequence. Another separate as-prepared sample (film size: ~10 mm × 10 mm ×120 nm) is evenly cut into four pieces, which are named No.1, 2, 3 and 4, respectively. First, No 2, 3 and 4 are annealed in N_2, then No.3 and 4 are

annealed in O_2, and finally No. 4 is annealed in N_2 again. All of the annealing conditions are kept the same as before. Therefore, No. 2, 3 and 4 represented the identical annealing sequence in the magnetism characterization. These four pieces are tested by four point probe method after Al is evaporated as the electrode by a shadow mask. The resistivity results are shown in Fig.3-3-10, together with unit volume saturation magnetization moment (M_S) for comparison. As expected, after annealing in N_2, the resistivity is reduced remarkably due to the creation of oxygen vacancies providing donors, while it increases tremendously then after the following O_2 annealing, owning to the depression of oxygen vacancies. Finally, the annealing in N_2 again recovers the small resistivity. This again supports the proposed mechanism very well. The inconsistency between the as-grown one and the one after annealing in O_2, when considered in terms of their magnetic behavior, could be attributed to the lower mobility in the as-grown sample without annealing.
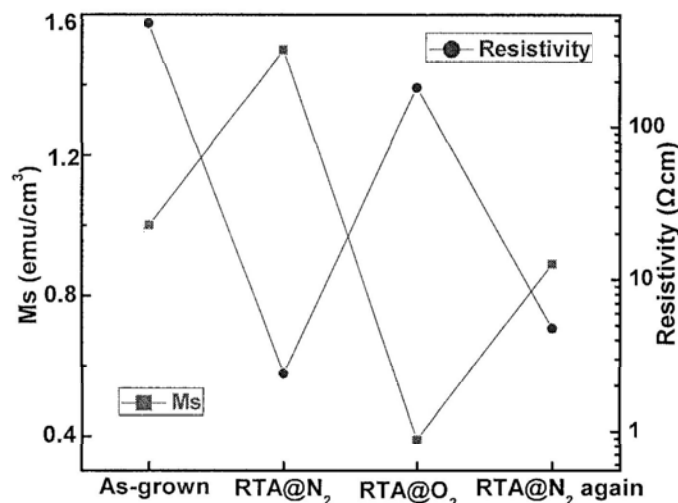
Fig.3-3-10 Unit volume saturation magnetization moment (M_S) and resistivity evolutions with consecutive annealing.

3.4 Ferromagnetism in single crystalline ZnO

In previous discussion, room temperature ferromagnetism is mainly attributed to oxygen vacancy. Solution prepared ZnO thin films followed by high temperature annealing are usually polycrystalline, as shown in our study. Many grain boundaries are present in polycrystalline thin films. Recently, it is claimed by Ref. [43] that room temperature ferromagnetism in pure oxide nanostructures is originated from grain boundaries. When there is little grain boundary, the ferromagnetism may disappear. It is worth investigating whether room temperature ferromagnetism can be observed or not in single crystalline ZnO, provided that oxygen vacancies are present.

A comparative study is performed following the similar way. Single crystalline ZnO substrate sized 5 mm × 10 mm is bought from Hefei Kejing Materials Technology, Co., LTD, and it is cut identically into two halves. One is annealed in a ultrahigh vacuum chamber (8.0 $\times 10^{-10}$ mbar) at ~ 700 °C for 15 minutes, the other is not treated in any way, named as "virgin".
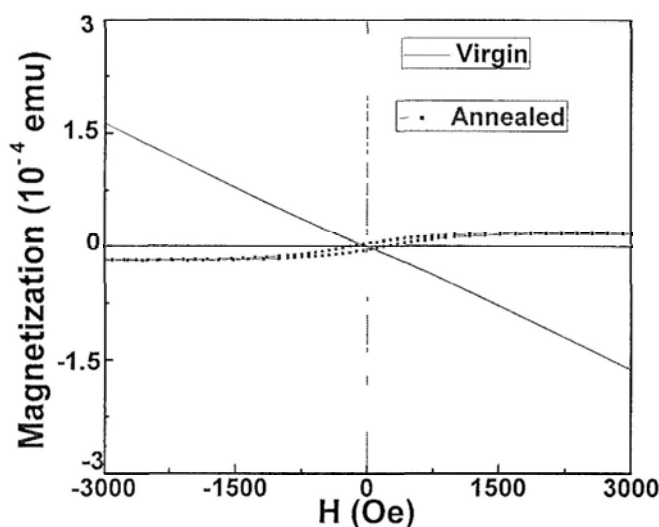
Fig.3-4-1 Magnetization dependence on magnetic field of virgin and annealed single crystal ZnO.

The one without annealing shows expected diamagnetic nature, while after annealing, a clear hysteresis loop can be observed. Since the annealing process is

performed in an ultrahigh vacuum chamber (8.0 $\times 10^{-10}$ mbar), foreign impurities could be excluded easily. There are no grain boundaries in single crystalline ZnO. This result unambiguously proves that RTFM is not relying on grain boundaries. Interface induced ferromagnetism as claimed by [44] can be excluded as well. It is easy to understand this in terms of oxygen vacancy based mechanism. The variation of oxygen vacancy in the annealing process has been investigated by photoluminescence spectroscopy in a previous publication [45], where a clear increase of defect concentration is observed.

Similar RTFM has been found in single crystalline TiO_2 [46], where the origin of magnetic moments are attributed to Ti^{3+}-V_O complex. It is suspected that a similar defect complex composed of Zn atoms and the nearby oxygen vacancies is present. Zn $L_3M_{45}M_{45}$ peak is examined to study whether a Zn related charge transfer process is involved. Compared to Zn $2p$ peak, the Auger peak Zn LMM is much more sensitive to chemical surroundings, and is more often selected to investigate the chemical state of Zn [47,48]. In the kinetic energy spectrum, $L_3M_{45}M_{45}$ peak lies at 988 eV for Zn^{2+}, while that of metallic Zn is close to 992 eV [48].

The result of single crystalline ZnO is shown in Fig.4-4-2. It is very obvious that the peak shifts towards a larger energy. This might be ascribed to a relieved bonding with oxygen vacancies nearby. A similar shift is observed when comparing the peaks of the spin-coated ZnO thin films annealed in O_2 and N_2, respectively, which is demonstrated in Fig.4-4-3. This shift is correlated with the Zn involved charge transfer process. In the present work, we include such kind of oxygen vacancy complex as well when referring to oxygen vacancies.
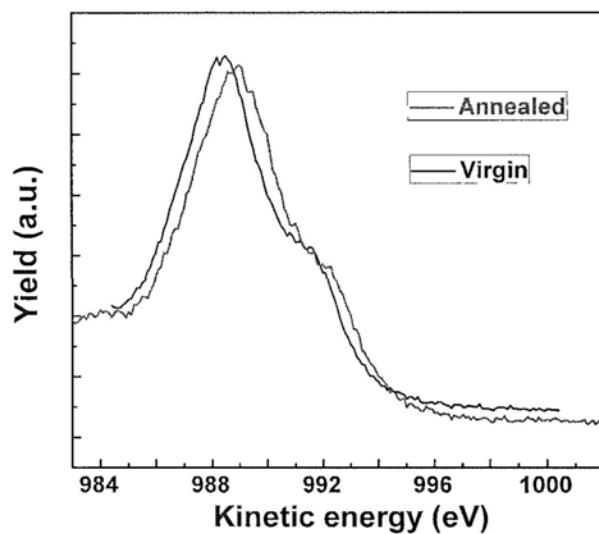
Fig.3-4-2 XPS spectra of Zn $L_3M_{45}M_{45}$ transitions in single crystalline ZnO.
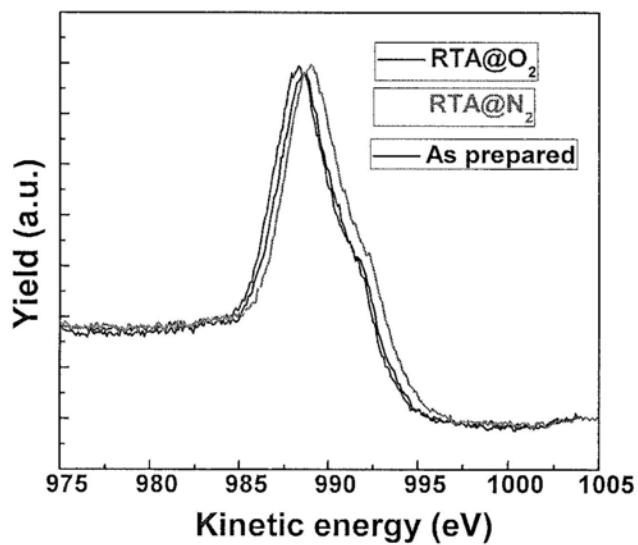
Fig.3-4-3 XPS spectra of Zn $L_3M_{45}M_{45}$ transitions of spin-coated ZnO thin films annealed in O_2 (blue), N_2 (magenta) and the as prepared (Black).

3.5 Oxygen vacancies and ferromagnetic interaction

It is assumed that oxygen vacancies in ZnO not only provide carriers responsible for conductivity, but also induce magnetic moment in adjacency. It is well known that oxygen vacancy mainly assumes +1 charge state (singly ionized), which is one of the main defects responsible for the n-type nature of pure ZnO [32, 35]. Singly ionized oxygen vacancies have been widely proved to be paramagnetic centers providing local magnetic moment by electron spin resonance [48-50]. In order to study the possibility of magnetic moment induced by oxygen vacancies in ZnO, the first-principle calculations are performed within Vienna *ab initio* simulation package (VASP) [25]. The PW91 general gradient approximation (GGA) is used [52-53]. The electron-ion interaction is described by PAW method [54]. 400 eV is used as the Plane-wave basis set cutoff. The on site coulomb interaction for Zn is used, namely GGA+U [55]. A $3 \times 3 \times 2$ super cell with a single oxygen vacancy is considered, corresponding to 2.8 % vacancy concentration. We use V_O^0, V_O^1, V_O^2 to denote oxygen vacancy with neutral, +1 and +2 valence states, respectively. The magnetic moments for V_O^0, V_O^1 and V_O^2 at 2.8 % concentration are 0.001 μ_B (Bohr magneton), 0.752 μ_B and 0.002 μ_B, respectively. The spin polarized density of states (DOS) of V_O^1 at 2.8 % concentration is shown in Fig.3-5-1. The Fermi level is within the band of spin up state and in the gap of spin down state.
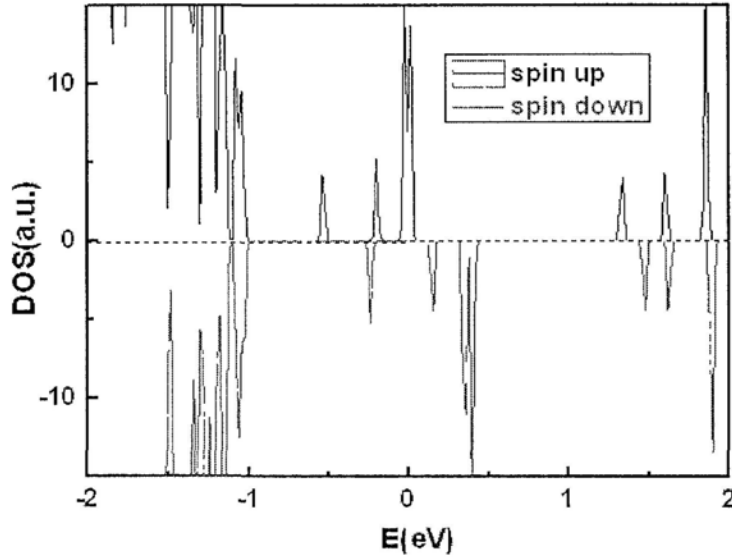
Fig.3-5-1 Spin polarized density of states (DOS) of V_O^1 in a $3 \times 3 \times 2$ supercell.

For a rough estimation to compare the experimental value with the calculation, by taking the oxygen vacancy concentration of around 2 % [56], using the magnetic moment of 1.6 emus per cubic centimeter in our experimental case, we can obtain the average magnetic moment of a single oxygen vacancy of 0.2 μ_B, which is on the same order of magnitude of our calculated result for singly ionized oxygen vacancy. It is worthy of noting that the first-principles calculation is only applicable to the low temperature scenario. Our experimental result indicates that the low temperature ferromagnetism and RTFM of ZnO show almost the same magnitude. The above calculation corroborates the validity of the proposed assumption. Similar spin moment induced by singly ionized oxygen vacancy has been reported in TiO_2 [57], which has been found to show RTFM in the absence of magnetic doping as well [58].

Another theoretical study has also reported the oxygen vacancies mediated spin-spin interaction in ZnO by use of the projector augmented wave (PAW) formalism of DFT as implemented in the VASP package [59]. It is found that the coupling of $3d$ states with delocalized O-$2p$ states leads to the FM coupling between the localized magnetic moment. The FM coupling is calculated to be energetically more stable than the anti-FM state, although the V_O at different sites contributes differently to the spin interaction. The electrons of O ions is also spin-polarized to

some extent.

In addition to pure ZnO, such oxygen vacancy induced ferromagnetism has also been confirmed theoretically in pure TiO_2 [60]. It is found that in a $2 \times 2 \times 2$ supercell, one oxygen vacancy can induce a magnetic moment of 0.22 μ_B in the near neighboring Ti site because of chare redistribution. This magnetic moment is very close to our calculation in the case of ZnO, as shown previously. Nevertheless, like the wide dispute in the experimental result, various other defects such as zinc vacancies, extended surface states, etc. have been attributed to induce the ferromagnetism in other theoretical works [61-62], which suggest the complexity of the defect scenarios or the importance of the calculation parameters or other approximation treatments.

It is claimed that net magnetic moment is formed by clustered oxygen vacancies [20]. It is difficult to distinguish the role of isolated and clustered oxygen vacancies; both cases are included in the present work. In these reports of defect induced ferromagnetism, it is usually observed that there is only a slight difference between the ferromagnetism at low temperature and room temperature [13,63], including results presented here. This might be because of the compromised effect of the reduced defect concentration (magnetic moment centers) and the weaker thermal disturbance to ferromagnetic interaction at lower temperatures.

Another possibility is that the creation of oxygen vacancy leads to the d orbital of nearest neighboring Zn not fully being occupied, presumably in a charge transfer process. This local unpaired $3d$ electron provides local magnetic moments. In this case, the defective complex of Zn and oxygen vacancy serves as the magnetic moment centers, as opposed to the single oxygen vacancy (or vacancy clusters) alone. Similar mechanism has been described in single crystal TiO_2 [64]. Evidence in favor of this mechanism has been provided aforementioned. This complex is sensitive to charge transfer in re-dox reactions and environments, which may account for the different behaviors in different annealing conditions, and in some other reported surface modifications [15]. Localized carriers around the local moment form the bound magnetic polaron (BMP). More BMPs would be formed provided that the

localized carrier and moment concentrations are increased. The role of these localized carriers mediating the coupling between moments has been confirmed in [65]. As the concentration of defect complex increases beyond the percolation threshold, hopping of localized carriers are large enough to form a long-range ferromagnetic order between the magnetic moment centers (oxygen vacancies themselves or Zn-oxygen vacancy defect complex).

Experimental evidences in favor of oxygen vacancies induced ferromagnetism has been provided previously. In most cases of ZnO thin films prepared by spin-coating, they are poorly semiconducting or near insulating, which is hardly explained by the carrier mediated ferromagnetism. The defect nature of ferromagnetism in this conducting regime has been confirmed in a majority of previous studies [5-9], and can be well explained by the bound magnetic polaron model proposed by J. M. D. Coey *et al.* [66].
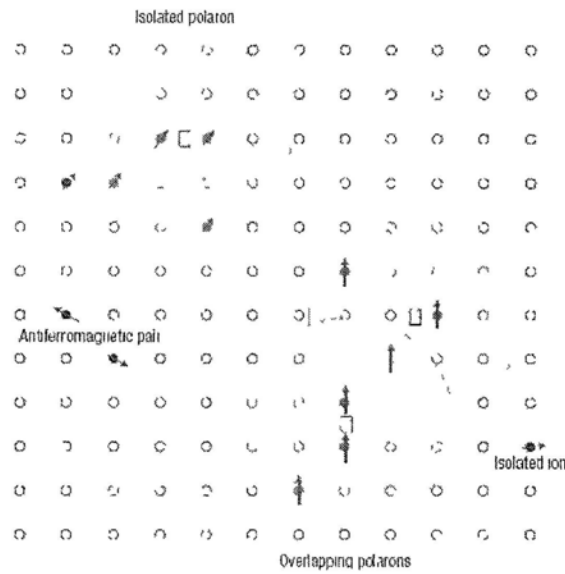
Fig.3-5-2 Representation of magnetic polarons.

The mechanism of bound magnetic polaron is illustrated in Fig.3-5-2 [66], where the black solid circles indicate otherwise the isolated magnetic moment and the square represents the defect bound with the magnetic moment. The defect captures bound electron nearby. Within the localization radius of the bound electron (the blue shaded

region), the magnetic moments can be ferromagnetically coupled. As long as the defect concentration and the magnetic moment concentration are large enough, the overlapping of these bound magnetic polarons can interact with each other to exhibit a long range ferromagnetism, as found in other coupling models such as RKKY. In the magnetically doped ZnO or other oxide, the magnetic moments arise from the doped magnetic ions. However, without magnetic doping, this magnetic moment is supposed to arise from the oxygen vacancy itself. This possibility has been reported in other works [20]. As mentioned previously, this local magnetic moment can also be created by the less fully occupied d orbital of Zn as a result of local charge transfer. Therefore, the traditional s-d exchange interaction mechanism can be still applicable.

The exchange interaction between a localized spin moment S and the bound donor electron s can be described in the following equation [66]:

$$-J_{sd}S \bullet s \left| \psi(r) \right|^2 \Omega$$

(3-2)

where J_{sd} is the s-d exchange interaction parameter, r is the localization radius of the donor electron and Ω is the volume of the magnetic polaron. With this model, it is not difficult to understand that the collective ferromagnetism is related to the concentration of magnetic moments and the coupling strength between these moments. Therefore, this model agrees with our finding that larger M_S is observed when the oxygen vacancy concentration is increased.

The ferromagnetism in oxide without magnetic doping is called d^0 magnetism. On the other hand, this magnetism can be explained qualitatively from the energy point of view. Unlike the traditional bound magnetic polaron model, defect states themselves give rise to magnetic moments associated with molecular orbitals localized in the vicinity of the defects, as shown in Fig.3-5-3. These states then create the impurity band needed to mediate a long-range ferromagnetic interaction between them [67]. The impurity band need not be metallic. It can facilitate the spin exchange provided the localization length is less than the distance between the defects. This is the basis of a calculation by Monnier and Delley [68]. In ZnO or other oxides, these defects are

typically oxygen vacancies (*F* centers). High Curie temperatures arise when the $3d\uparrow$ or $3d\downarrow$ density of states mixes with the spin-split impurity band at the Fermi level [69]. In this picture, the criterion for ferromagnetism is a sufficiently large density of states at the Fermi level $D(E_F)$ for the Stoner criterion [69]

$$D(E_f)I > 1$$

(3-3)

to be satisfied, where *I* is the band exchange integral. Almost inevitably, this means a d or f band, so magnetic metals and alloys generally involve d or f elements with partly-filled bands [69].
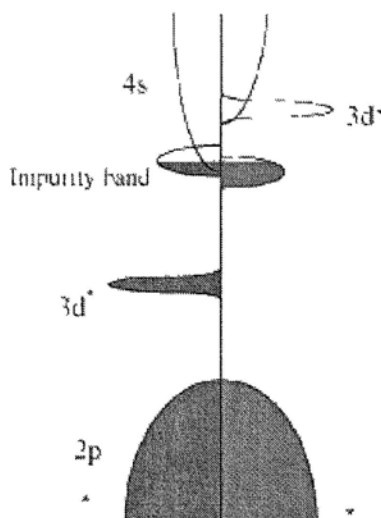
Fig.3-5-3 Population of an unoccupied *d* band by overlap with an impurity band, which leads to spin splitting of the latter.

It has been claimed that the reason leading to the controversial reported magnetic properties in ZnO based dilute magnetic oxide is partially the magnetic phase inhomogeneity in dilute magnetic oxides by Y. H. Wu *et al* [70]. In our study, this is possible as well, because the microscopic coexistence of ferromagnetic coupled region or paramagnetic region can't be excluded. The oxygen vacancies may not be uniformly distributed. In those regions where magnetic polarons are too far away to be interactive, paramagnetic phase may exist. The collective magnetic performance

may depend on the relative amplitude of the ferromagnetic phase or the paramagnetic phase.

Very recently, in the crystalline ZnO nanowires, a close investigation between the oxygen vacancy concentration, room temperature magnetization moment and PL intensity ratio of green band and UV emission intensity has been reported [71]. It is found that oxygen vacancies boost both the green band emission and the magnetism, which is in good agreement with our findings. It might be argued that the green band emission in PL can be attributed to other defects such as zinc interstitials, however, because of the larger formation energy than oxygen vacancy, these defects are usually only formed in the O_2 rich environment [72-73]. Although both PL and magnetic properties are closely linked with the oxygen deficiency, the associated physical mechanisms and their quantitative dependence are not necessarily identical.

3.6 Conclusion

To conclude this chapter, RTFM has been found in spin-coated un-doped ZnO thin films. With the support of ICP-MS and other composition characterization techniques, it is concluded that this RTFM is intrinsic. The correlations between the magnetic, optical and electrical characterization of the films under various treatment processes provide evidences for the role of oxygen vacancies, which is consistent with the findings of ferromagnetism in other un-doped oxides [31,74]. During a sequential annealing in N_2-O_2-N_2, consistent reversible correlation among the ferromagnetism, cathodoluminescence, and electronic performance evolution has been found with the support of Raman spectra. A presumptive description about the magnetic moment formation and ferromagnetic interaction mechanism has been put forward. Theoretical calculations show good agreement with the assumption based on the experimental findings.

References

[1] T. Dietl, H. Ohno, F. Matsukura, J. Cibert, D. Ferrand, Science, 287, 1019 (2000).

[2] K. R. Kittilstved, D. A. Schwartz, A. C. Tuan , S. M. Heald , S. A. Chambers, D. R. Gamelin, Phys. Rev. Lett. 97, 037203 (2006).

[3] Z. L. Lu, H. S. Hsu , Y. H. Tzeng, F. M. Zhang, Y. W. Du, J. C. A. Huang, Appl. Phys. Lett. 95, 102501 (2009).

[4] Z.Yang, M. Biasini, W. P. Beyermann, M.B.Katz, O. K. Ezekoye, X. Q. Pan, Y. Pu , J. Shi, Z. Zuo, J. L. Liu, J. Appl. Phys. 104, 113712 (2008).

[5] D.Yan, Z Z. Sun, Q. Liu, Z. Li, Z. Pan, J. Wang, S. Wei , Appl.Phys.Lett., 91, 062113 (2007).

[6] D. A. Schwartz, D. R. Gamelin, Adv. Mater.16, 2115 (2004).

[7] R. S. Lubna, Z. Hao, W. G. Wang, A. Bakhtyar, Z. Tao, F. Xin, Y. Q. Song, Q. Y. Wen, H. W. Zhang, S. Ismat, Q. X. John, J. Phys. D: Appl. Phys. 43, 035002 (2010).

[8] V. K. Sharma,G. D.Varma, J. Appl. Phys., 102, 056105 (2007); G. Milan, J. Gerhard , H. Christian, A. Hermann, Phys. Rev. B, 75, 205206 (2007).

[9] M. Venkatesan, C. B. Fitzgerald, J. M. D. Coey, Nature, 430, 630 (2004).

[10] E. Z. Liu, J. F. Liu, Y. He, J. Z. Jiang, J. Magn. Magn. Mater., 321, 3507 (2009).

[11] C. Song, F. Zeng, K. W. Geng, X. B. Wang, Y. X. Shen, F. Pan,   J. Magn. Magn. Mater., 309, 25 (2007).

[12] P. K. Sharma, R. K. Dutta, A. C. Pandey, J. Magn. Magn. Mater., 321, 4001 (2009).

[13] Q. Xu, H. Schmidt, S. Zhou, K. Potzger, M. Helm, H. Hochmuth, M. Lorenz, A. Setzer, P. Esquinazi, C. Meinecke, M. Grundmann, Appl. Phys. Lett. 92, 082508 (2008).

[14] M. Kapilashrami, J. Xu , B. Strom, K. V. Rao, L. Belova, Appl. Phys. Lett. 95, 033104 (2009).

[15] M. A. Garcia, J. M. Merino, P. Fernndez, A. Quesada, J. Venta, M. L. Ruz, G. R. Castro, P. Crespo, J. Llopis, J. M. Gonzlez-Calbet, A. Hernando, Nano.Lett. 7, 1489 (2007).

[16] J. B. Yi , H. Pan, J. Y. Lin, J. Ding, Y. P. Feng, S. Thongmee, T. Liu, H. Gong, L. Wang, Adv. Mater. 20, 1170 (2008).

[17] A. Y. Karen, M. H. Steve, J. B. Anthony, R. N. James, S. S. David, J. B. Harry, A.

G. Gillian, R. B. Will, F. C. Lesley, Phys. Rev. B, 80, 245207 (2009).

[18] P. P. Raghava, P. Kharel, C. Sudakar, C. Naik, R. Suryanarayanan, V. M. Naik , A.G.Petukhov, B. Nadgorny, G. Lawes, Phys. Rev. B,79, 165208 (2009) .

[19] T. S. Herng, S. P. Lau, C. S. Wei, L. Wang, B. C. Zhao, M. Tanemura, Y. Akaike, Appl. Phys. Lett. 95, 133103 (2009).

[20] S. Banerjee, M. Mandal, N. Gayathri, M. Sardar, Appl. Phys. Lett. 91, 182501 (2007).

[21] A. Sunaresan, R. Bhargavi, R. Rangarajian, S. Siddesh, C. N. R. Rao, Phys. Rev. B. 74,161306 (2006).

[22] Q. Wang, Q. Sun, G. Cheng, Y. Kawazoe, P. Jena, Phys. Rev. B 77, 205411 (2008).

[23] N. Sanchez, S. Gallego, M. C. Mu~noz, Phys. Rev. Lett.101, 067206 (2008).

[24] E. Z. Liua, J. Z. Jiang, J. Appl. Phys. 107, 023909 (2010).

[25] R. Podila, W. Queen, A. Nath, T. A. Jeverson, L. S. Aline, A. Fazzio, M. D. Gustavo, J. He, J. H. Shiou, J. S. Malcolm, M. R. Apparao, Nano Lett. 10 (4), 1383 (2010).

[26] H. W. Peng, H. J. Xiang, S. H. Wei, S. S. Li, J. B. Xia, J. B. Li, Phys. Rev. Lett.102, 017201 (2009) .

[27] S. Chawla, K. Jayanthi, R. K. Kotnala, J. Appl. Phys. 106, 113923 (2009); Y. Jin, Q. Cui,G. Wen, Q. Wang, J. Hao, S. Wang, J. Zhang, J. Phys. D: Appl. Phys. 42, 215007 (2009).

[28] X. Zhang, Y. H. Cheng, L. Y. Li, H. Liu, X. Zuo, G. H. Wen, L. Li, R. K. Zheng, S. P. Ringer, Phys. Rev. B, 80, 174427 (2009) .

[29] N. Jedrecy, H. J. Bardeleben, D. Demaille, Phys. Rev. B 80, 205204 (2009).

[30] N. H. Hong, J. Sakai, V. Brize, J. Phys.: Condens. Matter. 19, 036219 (2007); N. H . Hong, J. Sakai, F. Gervais, J. Magn. Magn. Mater. 316, 214 (2007).

[31] J. M. D. Coey, M. Venkatesan, P. Stamenov, C. B. Fitzgerald, L. S. Dorneles, Phys. Rev. B. 72 , 24450 (2005); N. H. Hong, J. Sakai, N. Poirot, V. Briz´e, Phys. Rev. B 73, 132404 (2006).

[32] K. Vanheusden, C. H. Seager, W. L. Warren, D. R. Tallant, J. A. Voigt, Appl. Phys. Lett. 68, 403 (1996); D. C. Oh , S. H. Park, H. Goto, I. H. Im, M. N. Jung, J. H. Chang, T. Yao, J. S. Song, C. H. Bae, C. S. Han, K. W. Koo, Appl. Phys. Lett. 95, 151908 (2009).

[33] Q. Zhao, P. Wu, B. L. Li, Z. M. Lu, E. Y. Jiang, J. Appl. Phys. 104, 073911 (2008).

[34] D. Q. Gao, Z. Zhang, J. Fu, Y. Xu, J. Qi, D. Xue, J. Appl. Phys.105, 113928 (2009).

[35] X. L. Wu, G. G. Siu, C. L. Fu, H. C. Ong, Appl. Phys. Lett. 78 (2001)2285; Y. Y. Peng, T. E. Hsieh, C. H. Hsu, Nanotechnology, 17, 174 (2006).

[36] T. M. Børseth, B. G. Svensson, A. Y. Kuznetsov, P. Klason, Q. X. Zhao, M. Willander, Appl. Phys. Lett. 89, 262112 (2006).

[37] M. D. McCluskey, S. J. Jokela1, J. Appl. Phys.106, 071101 (2009).

[38] Y. F. Tian, J. Antony, R. Souza, S. S.Yan, L. M. Mei, Y. Qiang, Appl. Phys. Lett. 92, 192109 (2008).

[39] A. Poppl, G.Volkel, Status Solidi A. 125, 571 (1991).

[40] T. Tatsumi, M. Fujita, N. Kawamoto, M. Sasajima, Y. Horikoshi, Jpn. J. Appl. Phys. Part 1. 43, 2602 (2004).

[41] D. Karmakar, S. K. Mandal, R. M. Kadam, P. L. Paulose, A. K. Rajarajan, T. K. Nath, A. K. Das, I. Dasgupta, G. P. Das, Phys. Rev. B. 75, 144404 (2007).

[42] J. S. Thakur, G. W. Auner, V. M. Naik, P. Kharel, G. Lawes, R. Suryanarayanan, and R. Naik, J. Appl. Phys. 102, 093904 (2007).

[43] B. B. Straumal, A. A. Mazilkin, S. G. Protasova, A. A. Myatiev, P. B. Straumal, G. Schütz, P. A. van Aken, E. Goering, and B. Baretzky, Phys. Rev. B 79, 205206 (2009).

[44] Z. G. Yin, N. F. Chen, Y. Li, X. W. Zhang, Y. M. Bai, C. L. Chai, Y. N. Xie, and J. Zhang, Appl. Phys. Lett. 93, 142109 (2008).

[45] W. G. Xie, F. Y. Xie, X. L. Yu, K. Xue, J. B. Xu, J. Chen, and R. Zhang, Appl. Phys. Lett. 95, 262506 (2009).

[46] S. Zhou, E. Čižmár, K. Potzger, M. Krause, G. Talut, M. Helm, J. Fassbender, S. A. Zvyagin, J. Wosnitza, and H. Schmidt, Phys. Rev. B 79, 113201 (2009).

[47] P. Hsieh, Y. Chen, K.S. Kao, C. M. Wang, Appl. Phys. A, 90, 317 (2008).

[48] H. Amekura, O. A. Plaksin, M. Yoshitake, Y. Takeda, N. Kishimoto, and C. Buchal, Appl. Phys. Lett. 89, 023115 (2006).

[49] D. Pan, G. Xu, L. Lv, Y. Yong, X. Wang, J. Wan, G. Wang, Appl. Phys. Lett. 89, 082510 (2006).

[50] S. Yang, L. E. Halliburton, A. Manivannan, P. H. Bunton, D. B. Baker, M. Klemm , S. Horn, A. Fujishima, Appl. Phys. Lett. 94, 162114 (2009).

[51] S. M. Evans, N. C. Giles, L. E. Halliburton, L. A. Kappers, J. Appl. Phys. 103 , 043710 (2008).

52 J. P. Perdew, J. A. Chevary, S. H. Vosko, K. A. Jackson, M. R. Pederson, D. J. Singh, and C. Fiolhais, Phys. Rev. B. 46, 6671 (1992).

53 J. P. Perdew, and Y. Wang, Phys. Rev. B .45, 13244 (1992).

54 G. Kresse, and D. Joubert, Phys. Rev. B. 59, 1758 (1999).

55 S. L Dudarev, G. A. Botton, S. Y. Savrasov, C. J. Humphreys, and A. P. Sutton, Phys. Rev. B. 57, 1505 (1998).

56 A. L. AL, and R. Ahuja, J. Phys.: Condens. Matter. 19, 386232 (2007).

57 S. Yang, L. E. Halliburton, A. Manivanan, P. H. Bunton, D. B. Baker, M. Klemm, S. Horn, and A. Fujishima, Appl. Phys. Lett. 94, 162114 (2009).

58 D. Kim, J. Hong, Y. R. Park, and K. J. Kim, J. Phys.: Condens. Matter. 21, 195405 (2009).

59 E. Liu, and J. Z. Jiang, J. Appl. Phys. 107, 023909 (2010).

60 D. Kim, J. Hong, Y. R. Park and K. J. Kim, J. Phys.: Condens. Matter 21, 195405 (2009).

61 X. Zuo, S. Yoon, A. Yang, W. Duan, C. Vittoria, and V. G. Harris, J. Appl. Phys. 105, 07C508 (2009).

62 N. Sanchez, S. Gallego, and M. C. Mun~oz, Phys. Rev. Lett., 101, 067206 (2008)

63 V. Bhoslea, J. Narayan, Appl. Phys. Lett. 93, 021912 (2008)

64 S. Zhou, E. Čižmár, K. Potzger, M. Krause, G. Talut, M. Helm, J. Fassbender, S. A. Zvyagin, J. Wosnitza, H. Schmidt, Phys. Rev. B 79, 113201 (2009).

65 H. Chou, C. P. Lin, H. S. Hsu, S. J. Sun, Appl. Phys. Lett. 96, 092503 (2010).

66 J. M. D. Coey, M. Venkatesan, and C. B. Fitzerald, Nature Mater. 4, 173 (2005)

67 R. Skomski, J. M. D. Coey, *Permanent Magnetism*, IOP Publishing, Bristol, 1999.

68 R. Monnier, B. Delley, Phys. Rev. Lett. 87, 157204 (2001).

69 J. M. D. Coey, Solid State Sciences 7, 660–667 (2005).

70 M. Tay, Y. H. Wu, G. C. Han, T. C. Chong, Y. K. Zheng, S. J. Wang, Y. B. Chen, and X. Q. Pan, J. Appl. Phys. 100, 063910 (2006)

71 G. Xing, D. Wang, J. Yi, L. Yang, M. Gao, M. He, Appl. Phys. Lett. 96, 112511 (2010).

72 S. Lany and A. Zunger, Phys. Rev. Lett. 98, 045501 (2007)

73 F. Oba, S. R. Nishitani, S. Isotani, H. Adachi, and I. Tanaka, J. Appl. Phys.90, 824 (2001).

74 M. Y. Ge, H. Wang,E. Z. Liu, J. F. Liu, Z. Jiang, Y. K. Li, Z. A. Xu, H. Y. Li,

Appl.Phys.Lett. 93 , 062505 (2008).

Chapter 4 Ferromagnetism of Doped ZnO Thin Films

4.1 Introduction

In the preceding chapter, we preliminarily conclude that oxygen vacancy is the dominant defect responsible for the observed room temperature ferromagnetism in un-doped ZnO thin film. There is dispute about whether magnetic doping is necessary or not for ZnO or other oxides to show ferromagnetism. However, our results tend to agree that the magnetic moment may come from the defect itself. Questions still remain whether the magnetic doping makes any profound influence on the ferromagnetic properties of ZnO thin film.

Meanwhile, our previous study focuses on un-doped ZnO thin films, which are less conductive or near insulating from the resistivity measurement in the preceding chapter. It is unknown yet whether there is a different story in the highly conductive region with far larger density of carriers. Moreover, most of the published work on doped ZnO has concentrated on insulating phase [1-4]. The observation of ferromagnetism has been reported in Al doped ZnO thin films where the carrier density is very high [5]. Motivated by this, G. A. Gehring *et al.* [6] made a systematic study on the relationship between the magnetism and conductivity in transition metal (TM) doped ZnO, where three distinct conductivity regimes have been identified: variable range hopping regime in which the least conducting films are the most magnetic; metallic phase at high carrier densities, in which the ferromagnetism depends on the ratio of density of free carriers to the magnetic ion; and an intermediate phase in which the ferromagnetism disappears.

Nevertheless, J. C. A. Huang *et al.* [7] drew a distinct conclusion after closely investigating the magnetic and transport properties of Co doped ZnO single crystalline thin films. Only two disparate ferromagnetism mechanisms in different conductivity regimes are found. In the near insulating regime, carriers tend to be

localized, favoring the formation of bound magnetic polarons, which leads to ferromagnetism. In the metallic regime, however, most carriers are weakly localized and the free carrier-mediated exchange is dominant.

The above two findings broadened our understanding of ferromagnetism in oxides extensively. Various otherwise contradicting outcomes can be unified into the proposed models. However, in addition to abundant findings of ferromagnetism in un-doped ZnO [8,9], SnO_2 [10], CeO_2 [11], TiO_2 [12] and In_2O_3 [13,14] thin films, nonmagnetic doping by carbon [15] or gallium [16] have also been reported to lead to the occurrence of ferromagnetism. The models above apparently can't account for ferromagnetism in these systems. Therefore, it is necessary to investigate relation between the magnetic properties and transport behaviors where no magnetic ions are introduced. In this chapter, we are going to answer the above two questions: a. whether the magnetic doping can significantly increase the magnetization moments even it is not necessary to exhibit ferromagnetism and b. whether similar models based on the relation of magnetism and conductivity can be generalized into the non-magnetically doped system.

4.2 Magnetic properties tuning of ZnO thin films by doping

In this section, the magnetic properties of ZnO thin film is tuned by different doping to examine whether: (a) electrical conductivity or carrier concentration is influencing the magnetic performance; (b) magnetic doping can enhance the ferromagnetism significantly. Gallium in III state is a widely investigated donor, which can markedly increase the carrier concentration in ZnO thin film [17], whereas cobalt (II) is the usual magnetic dopant widely adopted to prepare ZnO based dilute magnetic semiconductors. We study three cases:

(I) Ga singly doped ZnO thin film,

(II) Co singly doped ZnO thin film,

(III) Ga and Co co-doped ZnO thin film.

4.2.1 Ga singly doped ZnO thin film

Ga singly doped ZnO (ZnGaO) thin film is prepared in this way. Gallium nitrate hydrate (99.9%) and zinc acetate (Zn（CH_3COO）$_2$, 99.99%) are dissolved (concentration: 0.7 M) in 2-methoxyethanol (99.9%), with monoethanolamine (MEA, 99.5%) as the stabilizer. The doping concentration is Ga: (Ga + Zn) = 1: 100. A homogeneous solution is obtained after stirring the mixture for 2 hours at 60 °C. The molar ratio of zinc acetate to MEA is kept at 1: 2. The sols are spin coated onto 1 cm × 1 cm Si (100) substrate at 3000 rpm for 30 seconds. Before spin-coating, the substrate is ultrasonically washed consecutively by DI water, ethanol, and acetone for 30 minutes respectively. The precursor films are preheated at 300 °C for 10 minutes to evaporate the organics. This coating and preheating cycle is repeated several times until the desired thickness (~ 120 nm, confirmed by surface profiler). The as-prepared ZnGaO thin film is treated by rapid thermal annealing (RTA) under N_2, O_2 or Ar (with purity of 99.99 %) ambient for 1 minute at about 680 °C.

XPS is employed to check whether Ga is substitutionally doped into ZnO structure or forms a segregated phase. High resolution Ga 2p peaks are shown in Fig.4-2-1. It is found that the positions of Ga 2p3/2 and Ga 2p1/2 peaks are located at 1119.0 and

1146.2 eV, respectively. These peak positions are in good agreement with the previously reported values [17,18], which suggests that Ga exists as Ga^{3+}. No other element is detected. The XRD pattern is almost the same as that of un-doped ZnO thin film, which has been shown in Chapter 3. This indicates that Ga^{3+} occupies Zn substitutional sites and, therefore, can act as an effective donor.
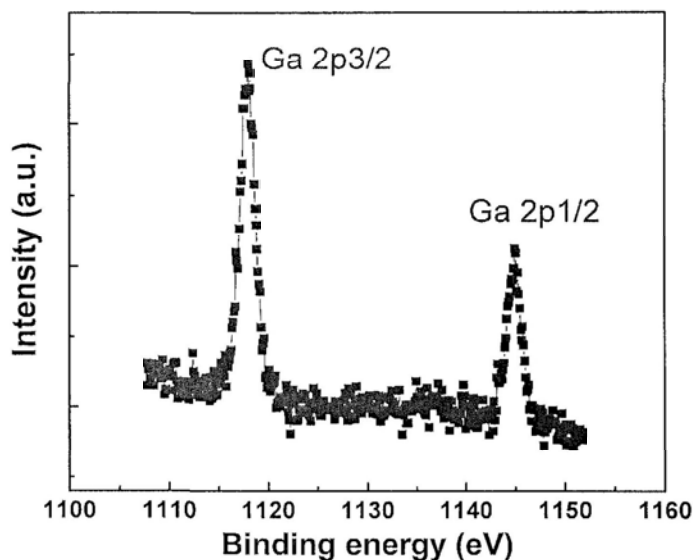
Fig.4-2-1 XPS spectrum of Ga 2*p*.

4.2.2 Co singly doped ZnO thin film

Co singly doped ZnO (ZnCoO) thin film is prepared in the same way. Cobalt acetate (99.99 %) is used as the starting agent. The doping concentration is Co: (Co + Zn) = 5: 100.

Similarly, XPS is employed to check whether Co is substitutionally doped into ZnO structure or forms a segregated phase. High resolution Co 2*p* peaks are shown in Fig.4-2-2.
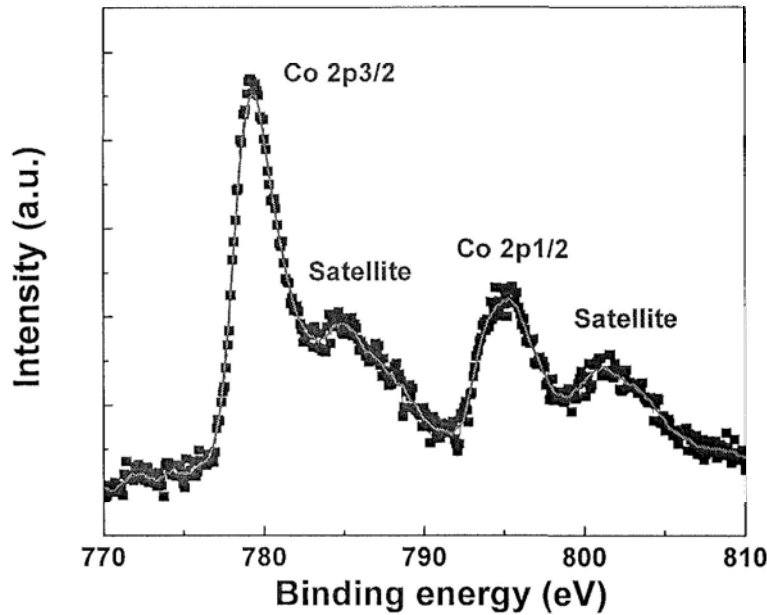
Fig.4-2-2 XPS spectrum of Co 2*p*.

It is observed that there are four peaks present: the 2*p*3/2 and 2*p*1/2 doublet and the shake-up resonance transitions (satellite) of these peaks at higher binding energies. The obtained binding energies for the Co 2*p* 3/2 and 2*p* 1/2 are 781.8 eV and 797.3 eV, respectively. These binding energies are very close to those reported for Co^{2+} in Co – O bonding with the energy difference between Co 2*p* 3/2 and *Co* 2*p* 1/2 being 15.5 eV [19-21]. If Co were in the form of Co clusters this energy difference would have been 15.05 eV [21-24]. Therefore, it is evident that there are no Co clusters present in the samples which could be detected in the XPS data.

4.2.3 Co and Ga co-doped ZnO thin film

Co and Ga co-doped ZnO (ZnGaCoO) thin film is prepared in the same way. The doping concentration is Co: Ga: (Co + Ga + Zn) = 5: 1: 100.

The XPS survey scan is shown in Fig.4-2-3. Compared with that of pure ZnO shown in Chapter 3, Co 2*p* peaks are clearly found. Other discernable peaks are either from Zn, O or C. Because of the low doping concentration of Ga, it can only be clearly found in the high resolution scan. The respective high resolution Ga 2*p* and Co 2*p* XPS spectrum is the same as those with single element doping.
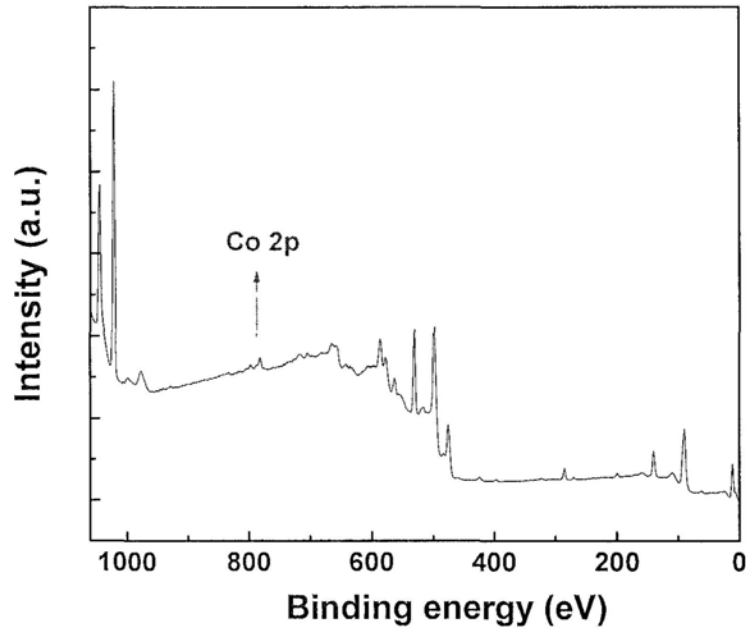
Fig.4-2-3 XPS spectrum of ZnGaCoO thin film.

The magnetization dependence on field of above three kinds of thin films annealed in N_2 is shown in Fig.4-2-4. The annealing in N_2 may help to prevent the oxidation of Co from secondary phase segregation, which has been suspected to happen when it is annealed in O_2 or air. The saturation magnetization moment in unit volume (M_S) of ZnGaO, ZnGaCoO and ZnCoO are 43, 12 and 2.5 $emu \cdot cm^{-3}$. Such a large M_S has been reported previously [25]. The interference from the substrate or unintentionally introduced magnetic impurity can be excluded in the same way as in previous study. We remembered that in Chapter 3, M_S of ZnO thin film annealed in N_2 is 1.6 $emu \cdot cm^{-3}$. Therefore, magnetic doping of Co shows no significant increase of magnetization moment. Interestingly, non-magnetic dopant increases the magnetization moment tremendously. The Hall effect resistivity ratio of ZnGaO: ZnGaCoO: ZnCoO is 0.1: 1: 10. The carrier concentration of ZnGaO thin films annealed in N_2 is on the order of 10^{20} cm^{-3}. Therefore, it could be initially concluded that the ferromagnetic interaction is more closely related to the electron concentration, rather than the concentration of magnetic dopant.
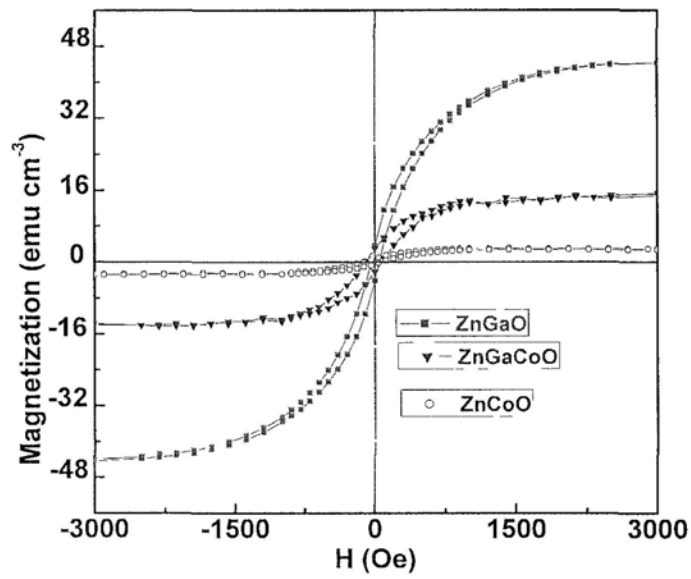
Fig.4-2-4 Hysteresis loops of ZnGaO (red square), ZnGaCoO (blue triangle) and ZnCoO (black circle).

4.3 Comparison study of ferromagnetism in Ga doped and un-doped ZnO thin films

So far, room temperature ferromagnetism has been observed both in highly conductive and less conductive ZnO thin films. In this section, a comparative study is conductive between the Ga-doped and un-doped ZnO thin films.

Similar to the previous study, the ferromagnetic properties of Ga doped ZnO (1 %) thin film annealed in disparate ambients. One piece of ZnGaO thin film prepared in the same way as aforementioned with the size of 10 mm × 10 mm × 120 nm is cut evenly into four pieces, three of which are annealed in N_2, Ar and O_2. Again, the purity is 99.99 %. The annealing temperature is 680 °C, and the time duration is 1 minute. After subtraction of the diamagnetic background of the Si substrate, the hysteresis loops are shown in Fig.4-3-1.
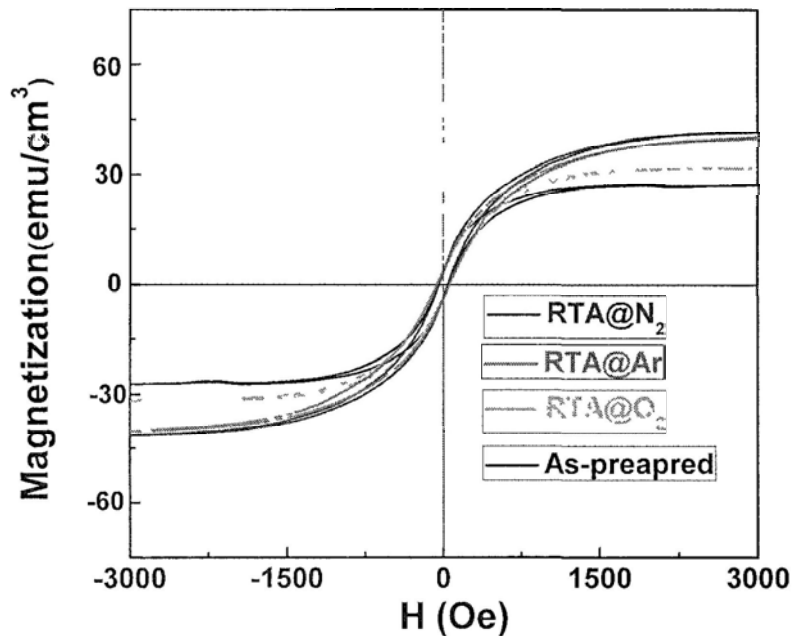
Fig.4-3-1 Hysteresis loops of Ga doped ZnO thin films annealed in different atmosphere.

For comparison convenience, the corresponding ferromagnetic behaviors of un-doped ZnO thin films are shown again in Fig.4-3-2.
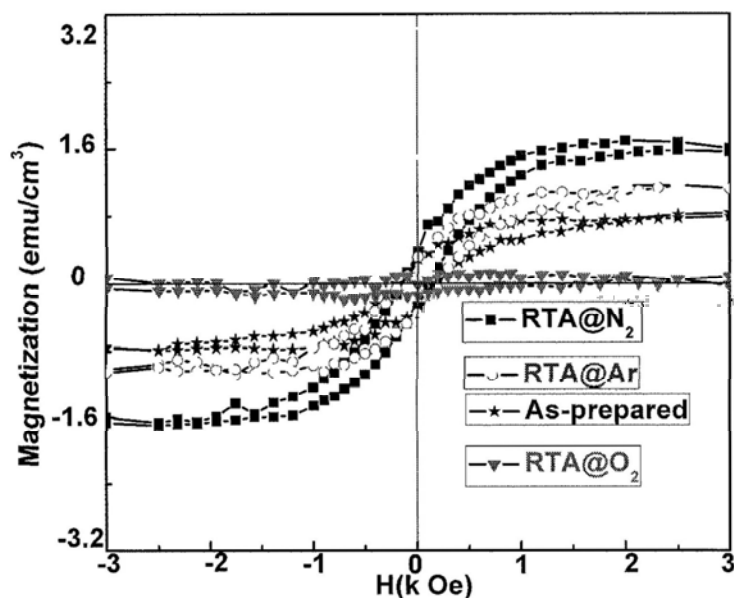
Fig.4-3-2 Hysteresis loops of un-doped ZnO thin films annealed in different atmosphere.

It is easy to observe that the saturation magnetization moments of the Ga doped ZnO thin film is obviously larger than that of the un-doped counterparts. This might be due to significant increase of band conducting electrons by Ga doping, as mentioned previously, which may increase the ferromagnetic coupling tremendously. The relative variation of M_S in ZnGaO thin film is almost the same as that in un-doped ZnO thin film, except that for ZnGaO thin film, M_S in the sample annealed in O_2 is not the smallest. This may be because different donor nature of the two thin films. In Ga doped ZnO thin film, the predominant donors are introduced by the additional doping of nominal Ga atoms, although oxygen vacancy still introduces donors as well. The coercive magnetic field for both is close to 100 Oe, which suggests the identical origin of magnetic moments.

Low temperature ferromagnetic behavior of Ga doped ZnO thin film is measured as well, which is demonstrated in Fig.4-3-3.
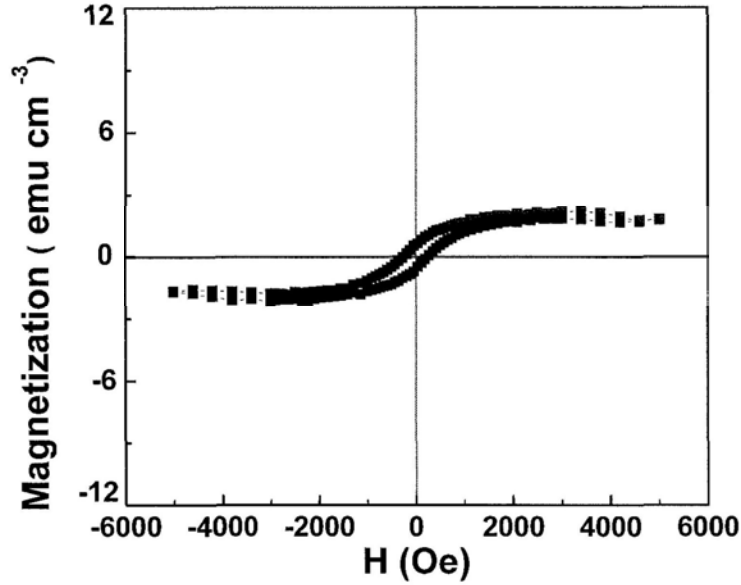
Fig.4-3-3 Hysteresis loop of Ga doped ZnO thin film measured at 5 K. Before low temperature measurement, the thin film is annealed in N_2. The corresponding room temperature M-H loop is shown in Fig.4-3-1.

In comparison with Fig.4-3-1, the saturation magnetization moment at 5 K decreased to less than tenth of that at 300 K. This behavior is totally different from that of un-doped ZnO thin film, where the M_S is found to be changed little when measured at low temperature (5 K). This implies that the mechanism of ferromagnetic coupling at room temperature and low temperature might be different, which is presumably originated from the disparate electrical conducting mechanisms.

The electronic transport can be described by a combination of thermal excitation model, which describes those carriers which have been thermally excited from localized states to the conduction band, and the variable range hoping model (VRH), which describes those carriers hopping between localized states. The resistivity dependence on temperature can be generalized into the following equation [26]:

$$\frac{1}{R}(T) = A\exp(-(C/T)^{1/4}) + B\exp(-E_d/kT)$$

(4-1)

where A and B are constants, E_d is the activation energy, which is the energy gap between the localized states and the lowest point of the conduction band, and C is the constant associated with the localized radius and the hopping radius of carriers around

localized states. The first term depicts the VRH transport model, whereas the seconds depicts the thermal excitation model. For the former model, a linear relation can be observed if ln $(1/R)$ is plotted against $(1/T)^{1/4}$, while for the latter, a linear relation is obtained by plotting ln $(1/R)$ against $1/T$.

In order to study the electrical conduction mechanism, resistivity dependence on temperature of Ga doped and un-doped ZnO thin films annealed in N_2 are measured. Fig.4-3-4 shows the ln $(1/R)$ against $(1/T)^{1/4}$ from 50 K ~ 4 K in Ga doped ZnO thin film.
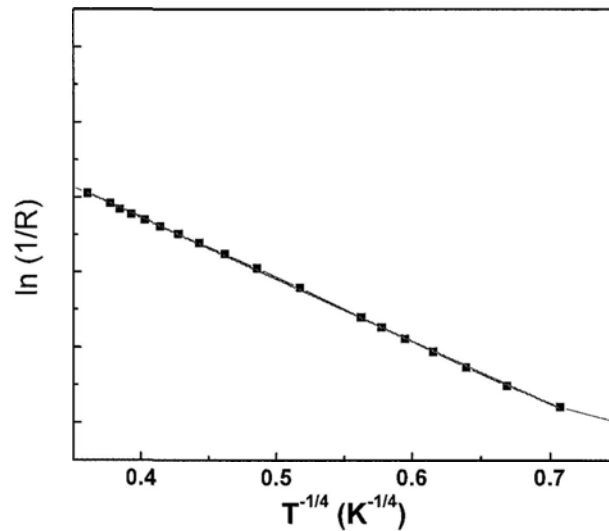
Fig.4-3-4 Linear fitting of ln $(1/R)$ against $(1/T)^{1/41/4}$ from 50 K ~ 4 K.

It can be found that excellent linear fitting is obtained in the temperature range of 4 K ~ 50 K for the relation of ln $(1/R)$ against $(1/T)^{1/4}$, which indicates that below 50 K, the electronic transport is following the VRH model. The ferromagnetic coupling may be via the hopping of electrons between the localized states mainly.

Fig.4-3-5 shows the plot of ln $(1/R)$ dependence on $1/T$ from 300 K to 100 K in the Ga doped ZnO thin film. It can be seen that in the range of 300 K ~ 150 K, the linear fitting is excellent, which indicates that above 200 K, the electronic transport in Ga doped ZnO thin film is following the thermal excitation model dominantly. In other temperature regions, the electronic conduction is the combination of both models.
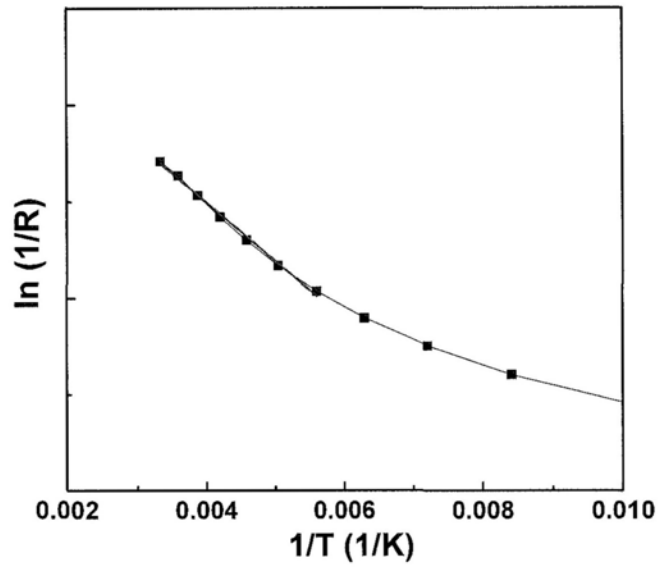
Fig.4-3-5 Linear fitting of ln (1/R) against 1/T from 300 K ~ 100 K.

Similar study has been conducted for un-doped ZnO thin film after annealing in N_2 in the same way. As expected, in the low temperature region, excellent linear fitting is obtained in the temperature range of 17 K ~ 60 K for the relation of ln (1/R) against $(1/T)^{1/4}$. Below 20 K, the measurement is aborted because of too large resistance of the thin film. It can be concluded that in the low temperature region, the electronic transport in un-doped ZnO thin film is mainly obeying the law of the VRH model.
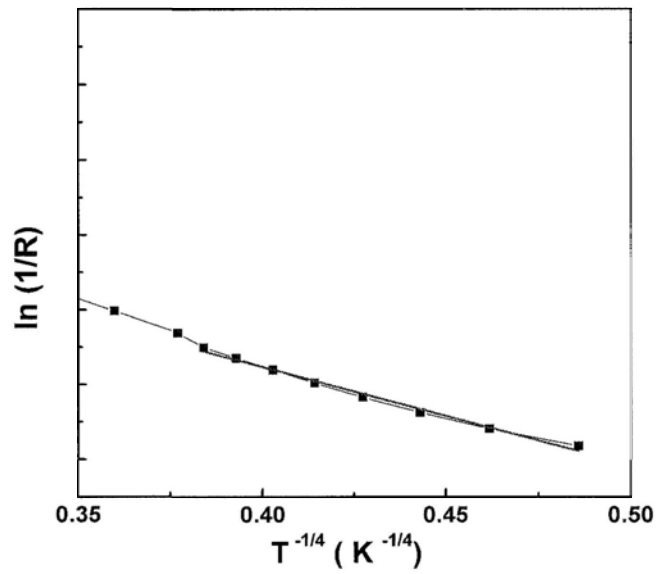
Fig.4-3-6 Linear fitting of ln $(1/R)$ against $(1/T)^{1/4}$ from 60 K ~ 20 K.

In the near room temperature region, the fitting result is also supporting a VRH model, as shown in Fig.4-3-7.
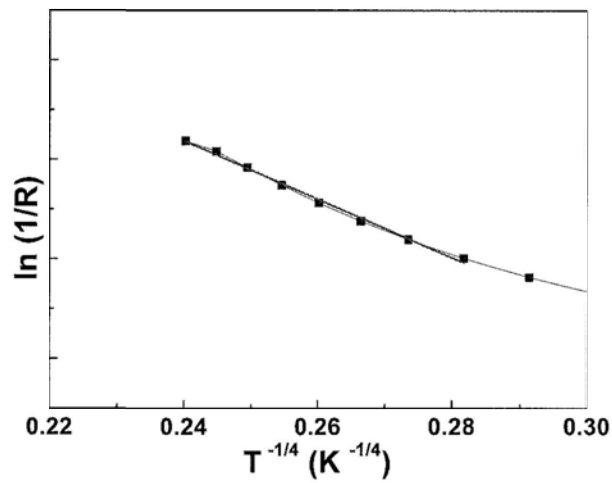
Fig.4-3- 7 Linear fitting of ln $(1/R)$ against $(1/T)^{1/4}$ in the near room temperature region.

85

It is assumed that the ferromagnetic coupling can be mediated by both localized electrons and conduction band electrons. The ferromagnetic coupling is much stronger by the mediation of band electrons than that of the localized electrons. The magnetic moment is intrinsic, rather than imported from the doping of magnetic ions. In the VRH conducting region, the mechanism can be well explained by the bound magnetic polaron model. A localized carrier is trapped by oxygen vacancy, which induces magnetic moment nearby as well. The exchange interaction aligns the moment of the localized carrier and the moment induced by the oxygen vacancy. Magnetic moments falling within the same localization radius of the localized electrons can be ferromagnetically coupled indirectly. This agrees very well with what has been proposed in single crystalline Co doped ZnO [7], in which the magnetic moment originates from transition metal Co, whereas in our case, the magnetic moment may originate from oxygen vacancy clusters [9], or d moment from Zn atom due to charge transfer with oxygen vacancy present around.

Carrier mediated ferromagnetism is possible in the highly conductive region. The ferromagnetic exchange interaction can be significantly increased due to a large carrier concentration.

4.4 Carrier mediated ferromagnetism in high conduction regime

In dilute magnetic semiconductors, the mechanism of carrier mediated ferromagnetism is based on the models in which the local magnetic moments are assumed to interact with each other via RKKY interactions. The basic idea behind the RKKY interaction is based on the exchange coupling between the magnetic moments and the conduction band free electrons [27]. The conduction electron is magnetized in the vicinity of the magnetic moment, with the polarization decaying with distance from the local moment in an oscillatory fashion. This oscillation causes an indirect superexchange interaction (RKKY) between two magnetic moments on the nearest or next nearest magnetic neighbors. This coupling may result in a parallel (ferromagnetic) or an anti-parallel (antiferromagnetic) setting of the moments dependent on the separation of the interacting atoms. The model becomes efficient when a high concentration of free carriers is present especially at higher temperatures.

There are two major ways of identifying the carrier spin polarization, x-ray magnetic circular dichroism (XMCD) and anomalous Hall effect (AHE), although a minority has questioned the latter [28]. XMCD is a difference spectrum of two x-ray absorption spectra (XAS) taken in a magnetic field, one taken with left circularly polarized light, and one with right circularly polarized light. By closely analyzing the difference in the XMCD spectrum, information can be obtained on the magnetic properties of the atom, such as its spin and orbital magnetic moment. In ferromagnetic materials (and paramagnetic materials in a magnetic field), the Hall resistivity includes an additional contribution, known as the anomalous Hall effect (or the Extraordinary Hall Effect), which depends directly on the magnetization of the material, and is often much larger than the ordinary Hall effect. Although a consensus about the origin has not been reached, it is widely attributed to the spin-dependent scattering of charge carriers.

In the preceding chapter, we have discussed about the ferromagnetic interaction in un-doped ZnO in terms of the bound magnetic polaron models (BMP), where the electrical conductivity is often very poor or they are even insulating, following the

VRH transport model. Whilst in this chapter, room ferromagnetism is also observed in the highly conduction regime, following the thermal excitation model. This ferromagnetic ordering is mediated by the band conduction electrons. This two-regime mechanism of ferromagnetism has been first proposed by Behan *et al.* [29] in the magnetically doped ZnO. Here we extend this theory to the case without magnetic doping. The only difference is that the magnetic moment is provided by the magnetic dopant or the defect itself. Similar to the conclusion of Behan *et al.* in the poor conduction regime, the exchange is mediated by occupied polaron orbits, and ferromagnetism occurs when the polaronic density reaches the percolation limit. As the electron density exceeds some threshold value (e.g. 10^{20} cm^{-3}), the carrier mediated ferromagnetism is possible. Very large magnetic circular dichroism (MCD) signal has been measured at the ZnO band edge (3.35 eV), which suggests that the ZnO band electrons are spin-polarized and contribute to the ferromagnetic ordering [29].
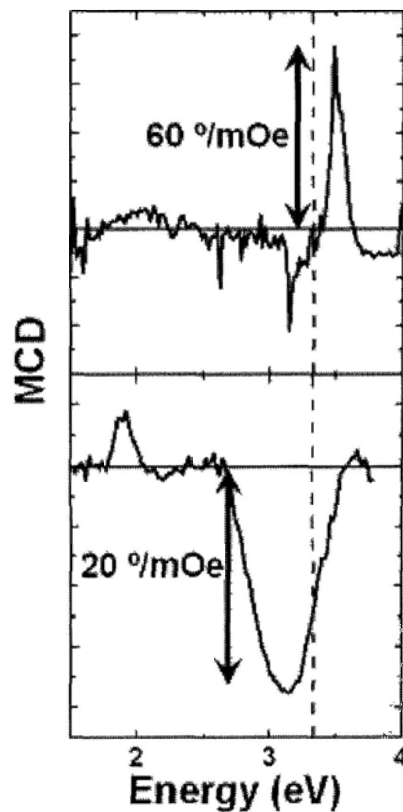
Fig.4-4-1 Room temperature magnetic circular dichroism spectra for the highly conductive ZnO by co-doping [29].

In the single crystalline ZnO, this carrier mediated ferromagnetic ordering has also been found [30], where the electron concentration is over 5×10^{19} cm^{-3}. The magnetization is found to be significantly increased as the electron concentration increases further. The anomalous Hall resisitivity follows the magnetization curve. The increase of anomalous Hall conductivity is due to the strengthened spin scattering due to spin-orbit interaction as the electron concentration increases in the high conduction regime, which is a strong evidence of carrier mediated ferromagnetism [30]. Based on this conception, this anomalous Hall effect can be electrically tuned by a gate voltage across a dielectric material, which modulates the carrier concentration in the semiconductor below the gate. This has been successfully first observed in the single crystalline ZnO by F. Hellman *et al.* [31]. As shown in Fig.4-4-2, as the gate voltage scans from negative to positive, the electron concentration increases accordingly. Therefore, the anomalous Hall effect becomes stronger as well. The electron concentration increase drives the sample into ferromagnetic state, which shows that the ferromagnetism originates from the electron mediated exchange interaction.
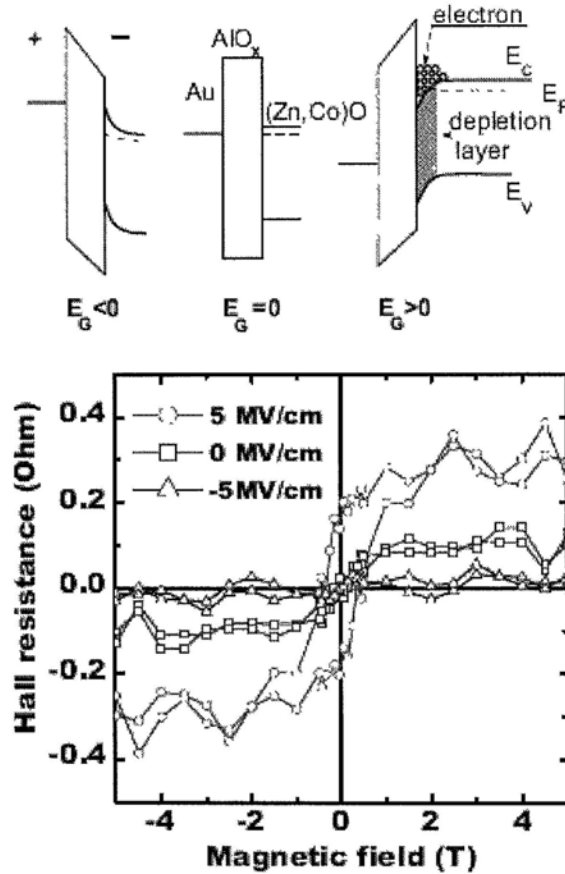
Fig.4-4-2 (Upper) Schematic band diagram and carrier concentration in the semiconductor; (Bottom) Electrode field controlled AHE in single crystalline ZnO [31].

It is worthy of noting that without magnetic doping, clear AHE [32-33] have also been reported. Therefore, the magnetic moments do not rely on the incorporation of magnetic ions. It is interesting to note that in these studies, hole-mediated exchange coupling has been claimed, which is rarely reported.

In addition to ZnO, carrier mediated room temperature ferromagnetism has also been found in other oxides, such as pure In_2O_3 [34]. Without any magnetic doping, clear room temperature ferromagnetism has been found once annealed in the vacuum condition. The magnetic moment has been ascribed to the presence of oxygen vacancies similarly. The electron concentration is 6×10^{19} cm^{-3}. In order to investigate the coupling between the charge carriers and the ferromagnetic moment in the In_2O_3 thin films, point contact Andreev reflection (PCAR) spectroscopy [35-36] has been used , which has recently emerged as a viable technique to directly measure the

transport spin polarization in magnetic materials [37] including dilute magnetic semiconductors [38-39]. The PCAR technique is based on the sensitivity of the quasiparticlesupercurrent conversion process (Andreev reflection) at a superconductor/normal contact to the degree of spin imbalance. It is found that in un-doped In_2O_3, the spin polarization is about 56 %. The high density of carriers is provided by oxygen vacancies. The exchange interaction between the electron spin s_i and the local magnetic moments J_j can be given in the following way

$$H_{ex} = -\Gamma_{ex} \sum_{i,j} \delta(r_i - R_j) s_i \bullet J_j$$

(4-2)

where Γ_{ex} is the exchange coupling, r_i and R_j are the position vector of electron spin s_i and the magnetic moment J_j. The donors can reside in the delocalized conduction band. The ordering of the localized spin moments will split the conduction band, resulting in a net spin polarization of conduction band electrons. The high density of states at the Fermi level accounts for the high Curie temperature [40], which is formed by the quasilocalized donor states. Because of self-compensation, a carrier concentration threshold is needed to overcome to mediate the magnetic moments [34].

From all of these results, it can be concluded that a high carrier concentration near 10^{20} cm^{-3} is needed to realize the long range ferromagnetic coupling. In the present study, by doping with Ga, the electron concentration in ZnO can be significantly increased to a few 10^{20} cm^{-3} , and we have observed clear magnetization hysteresis. A band conduction has been confirmed by the study of resistivity dependence on temperature. Therefore, it is reasonable to attribute the ferromagnetism to the carrier mediated exchange coupling without magnetic doping. However, because of unavailablity of equipment, we can't obtain XMCD, AHE or PCAR data to verify that the electrons are indeed spin-polarized. Obviously, a thorough and complete study will be necessary to continue to confirm the carrier mediated ferromagnetic ordering in the future.

4.5 Summary

By summarizing these two chapters discussing about ferromagnetic properties of ZnO thin films, we draw conclusions below:

(a) Room temperature ferromagnetism can be observed in un-doped ZnO thin films, even without the magnetic doping. It is intrinsic, rather than from foreign impurities or substrates.

(b) The observed ferromagnetism is closely related to defects. By electrical and spectroscopic investigation, evidences are collected to tentatively attribute the main origin to oxygen vacancy defect, by which we include oxygen vacancy clusters and oxygen vacancy related complex defects. The magnetic moment is more likely induced in a charge transfer process of Zn and surrounding oxygen vacancy.

(c) Grain boundary and interface are not the main origin of ferromagnetism, because even in single crystalline ZnO, the ferromagnetism can be observed as well.

(d) The magnetization moment can be tuned by additional donor doping, which is not necessarily magnetic ion. Both in the cases of highly conductive (Ga doped) and nearly insulating ZnO thin films, ferromagnetism can be observed, which indicates disparate mechanisms of ferromagnetic coupling in different electrical conduction regimes. Carrier mediated ferromagnetism through band conduction electrons is possible in the highly conductive region, whereas a bound magnetic polaron model through localized electron states is attributed to account for the mechanism in the less conductive or nearly insulating region.

It is important to note that due to the complexity of defect scenario in ZnO and other oxides, without a definitive way to distinguish different kinds of defects, and then measure the exact density of them, it is difficult to completely to shape an intact and explicable theory about the mechanism of ferromagnetism. Because of the poor reproducibility, the exact mechanism is still not clearly understood, although the evidence presented here supports the role of oxygen vacancies as the origin. Similar to

works of other groups, a direct and causal relationship between the ferromagnetism and any kind of defects has not been found, therefore the coincident observation of ferromagnetic, electrical and spectroscopic evolution can't be excluded to be occasional cases, the controversy still continues. To be more general, Table 4-5-1 lists all of the experiments we have conducted, showing the issues present in our work and this field.

Table 4-5-1 Experimental matrix showing the major conducted experiments and remarks.

Experiment Planned	Measurement/ characterization	Outcome / remark
Composition structure analysis	XRD of ZnO, Co-doped, Ga-doped ZnO.	C axis orientation preferred, reproducible.
	Surface morphology by SEM, AFM of ZnO, Ga-doped ZnO.	Homogeneous polycrystalline structure
	Surface profile for thickness determination.	In agreement with other thickness measurement, like SEM, XPS
	Cross section view by SEM of ZnO and doped ZnO.	NA
	XPS study of ZnO annealed in O_2, N_2 and Ar	No foreign impurities observed
	PL, CL study of ZnO thin films annealed in different conditions.	The typical band peak at 370 nm is observed, and can be reproduced most of the times. The defect emission is poorly reproducible from piece to piece.
Magnetic performance	Diamagnetic substrate.	Confirmed by a second time test.
	FC/ZFC of ZnO thin films.	In agreement with reported results [20].

	300 K, 5 K *M-H* loops of ZnO thin films.	The M-H hysteresis can be reproduced, the calculated M_S is in agreement with some reports [13], and different from some others [21]. The reported M_S ranges very broadly. The change of M_S at different temperatures find support in either doped or un-doped, prepared differently.
	300 K, 25 K, 5 K *M-H* loops of Ga-doped ZnO thin films.	As temperature decreases, the magnetization decreases, in agreement with reported results [30].
	M-H loop of ZnO with normal field	The reduction measured with normal magnetic field agrees with other reporting [30].
	M-H loop of ZnO with different thickness (120 nm /260 nm).	Confirmed and in agreement with the reported result [41].
Designed experiment	ZnO thin film annealed in O_2, N_2 and Ar.	Intended to study the defect change and M_S. All pieces are cut from the single sample to avoid the problem of film inhomogeneity to the largest extent. The amplitude relation between annealing in N_2, O_2 and Ar can find support in ZnO nanostructures fabricated differently. But the reproducibility needs to be confirmed.

		Intended to confirm the change of M_S annealed in N_2 and O_2 in N_2 and O_2. The measured Ms agrees well with above group. The regeneration of M_S in N_2 coincides with the electrical and CL evolution. Again, the reproducibility needs to be confirmed.
	Sequential annealing in O_2 and N_2.	
	Sequential annealing in H_2O_2 and H_3PO_3.	Intended to study the oxidization and reduction treatment on the FM performance. This experiment failed, possibly due to the magnetic impurities introduced from the solutions.
	Doping by N or Li to compensate the oxygen vacancy donors.	Intended to confirm whether the FM is reduced as the acceptor-type defects are introduced. The comparison has failed, possibly because of complex defects introduced, or acceptor defects not activated.
	Surface treatment by different functional groups,-SH or –NH.	Intended to study the charge transfer process and FM properties. The charge transfer may have influence on the chemical environment of oxygen vacancies. Unfortunately, no clear conclusion can be withdrawn. This is possibly due to weak interaction between

		the organic function group and is covered by experimental or measurement error.
	Co doped ZnO thin film annealed in O$_2$, N$_2$ and Ar.	In agreement with the case of un-doped ZnO.
	Ga doped ZnO thin film annealed in O$_2$, N$_2$ and Ar.	The M_S is largely increased and confirmed by the second time measurement. Hall effect and 4 point probe method confirmed that the resistivity is about two orders smaller than un-doped ZnO.

The poor reproducibility of defect study by PL and CL has plagued various researchers, which is straightforward for the very controversial scenario of the magnetic properties of ZnO. For a simple comparison, Table 4-5-2 summarizes parts of reported ferromagnetism in non-magnetically doped oxides. Although our evidences are not sufficient to completely affirm that the ferromagnetism is induced by oxygen vacancies, we extend the traditional understanding further, showing that the ferromagnetism can be found in both near insulating or highly conductive regime without magnetic doping. Further intensive investigation is needed to study the direct interaction between defects, carriers and the magnetic moments. What is encouraging is that spin Hall effect transistors have been experimentally realized in the most recent breakthrough work [42], which is assumed to bring further intensive study on the ZnO based spin field effect transistors.

Table 4-5-2 Summary of reported ferromagnetism in several typical non-magnetically doped oxides.

Materials	Resistivity ($\Omega \cdot cm$)	M_S (emu·cm^{-3})	Possible origin	References
ZnO	~ 1	~ 1	Oxygen vacancy	This work
ZnO	NA	0.5	Oxygen vacancy	43
ZnO	NA	~ 1	Zinc interstitial	28
ZnO	NA	~0.03	Oxygen vacancy	9
In$_2$O$_3$	0.01	~ 0.5	Carrier mediated (oxygen vacancy for the weak ferromagnetism)	41
ZnO (Ga)	conductive	~ 16	Oxygen vacancies	16
ZnO	> 2000	~ 1	Zn related factors	44
ZnO (C)	conductive	~ 2.16	C related factors	15

References

[1] J. M. D. Coey, Curr. Opin. Solid State Mater. Sci. 10, 83 (2006).

[2] C. Song, K. W. Geng, F. Zeng, X. B. Wang, Y. X. Shen, F. Pan, Y. N. Xie, T. Liu, H. T. Zhou, and Z. Fan, Phys. Rev. B 73, 024405 (2006).

[3] N. Khare , M. J. Kappers , M. Wei , M. G. Blamire , J. L. MacManus-Driscoll, Adv. Mater. 18, 1449 (2006).

[4] D. McManus, Adv. Mater. 56, 0472 (2008).

[5] X. H. Xu , H. J. Blythe , M. Ziese , A. J. Behan , J. R. Neal , A. Mokhtari , R. M. Ibrahim , A. M .Fox, and G. A. Gehring , New J. Phys. 8, 135 (2006).

[6] A. J. Behan, A. Mokhtari, H. J. Blythe, D. Score, X.H. Xu, J. R. Neal, A. M. Fox, and G. A. Gehring, Phys. Rev. Lett. 100, 047206 (2008)

[7] Z. L. Lu, H. S. Hsu, Y. H. Tzeng, F. M. Zhang, Y. W. Du, and J. C. A. Huang, Appl. Phys. Lett. 95, 102501 (2009).

[8] M. Kapilashrami, J. Xu, V. Ström, K. V. Rao, and L. Belova, Appl. Phys. Lett. 95, 033104 (2009).

[9] S. Banerjee, M. Mandal, N. Gayathrib and M. Sardar, Appl. Phys. Lett. 91, 182501 (2007).

[10] N. H. Hong, N. Poirot, and J. Sakai, Phys. Rev. B 77, 033205 (2008).

[11] V. Fernandes, R. J. O. Mossanek, P. Schio, J. J. Klein, A. J. A. de Oliveira, W. A. Ortiz, N. Mattoso, J. Varalda, W. H. Schreiner, M. Abbate, and D. H. Mosca, Phys. Rev. B 80, 035202 (2009).

[12] H. W. Peng, J. Li, S. Li, and J. Xia, Phys. Rev. B 79, 092411 (2009).

[13] A. Sundaresan, R. Bhargavi, N. Rangarajan, U. Siddesh, and C. N. R. Rao, Phys. Rev. B 74, 161306(R) (2006).

[14] R. P. Panguluri, P. Kharel, C. Sudakar, R. Naik, R. Suryanarayanan, V. M. Naik, A. G. Petukhov, B. Nadgorny, and G. Lawes, Phys. Rev. B 79, 165208 (2009)

[15] T. S. Herng, S. P. Lau, C. S. Wei, L. Wang, B. C. Zhao, M. Tanemura, and Y. Akaike, Appl. Phys. Lett. 95, 133103 (2009).

[16] V. Bhoslea, and J. Narayan, Appl. Phys. Lett. 93, 021912 (2008).

[17] V. Bhosle, A. Tiwari, and J. Narayan, J. Appl. Phys. 100, 033713 (2006).

[18] M. Passlack, E. F. Schubert, W. S. Hobson, M. Hong, N. Moriya, S. N. G. Chu, K. Konstadinidis, J. P. Mannaerts, M. L. Schnoes, and G. J. Zydzik, J. Appl. Phys. 77,

686 (1995).

[19] G. L. Liu, Q. Cao, J. X. Deng, P. F. Xing, Y. F. Tian, Y. X. Chen, S. S. Yan, and L. M. Mei, Appl. Phys. Lett. 90, 052504 (2007)

[20] L. F. Liu, J. F. Kang, Y. Wang, H. Tang, L. G. Kong, X. Zhang, and R. Q. Han, Solid State Commun. 139, 263 (2006).

[21] H. J. Lee, S. Y. Jeong, C. R. Cho, and C. H. Park, Appl. Phys.Lett. 81, 4020 (2002).

[22] C. D. Wagner, W. M. Riggs, L. E. Davis, and J. F. Moulder, *Handbook of X-ray Photoelectron Spectroscopy (Eden Prairie, MN: Perkin-Elmer)* 78, 1979.

[23] C. H. Choi, and S. H. Kim, Thin Solid Films, 515, 2864 (2007).

[24] Y. B. Zhang, Q. Liu, T. Sritharan, C. L. Gan, and S. Li, Appl. Phys. Lett. 89, 042510 (2006).

[25] N. H. Hong, J. Sakai, and V. Brizé, J. Phys.: Condens. Matter, 19, 036219 (2007).

[26] H. Chou, C. P. Lin, H. S. Hsu, and S. J. Sun, Appl. Phys. Lett. 96, 092503 (2010).

[27] C. Liu, F. Yun, H. Morkoc, J. Mater.Sci.: Materials in Electronics 16, 555– 597 (2005).

[28] Q. Xu, H. Schmidt, S. Zhou, K. Potzger, M. Helm, H. Hochmuth, M. Lorenz, A. Setzer, P. Esquinazi, C. Meinecke, and M. Grundmann, Appl. Phys. Lett. 92, 082508 (2008).

[29] A. J. Behan, A. Mokhtari, H. J. Blythe, D. Score, X-H. Xu, J. R. Neal, A. M. Fox, and G. A. Gehring, Phys. Rev. Lett 100, 047206 (2008).

[30] Z. L. Lu, H. S. Hsu, Y. H. Tzeng, F. M. Zhang, Y. W. Du, and J. C. A. Huang, Appl. Phys. Lett. 95, 102501 (2009).

[31] H. J. Lee, E. Helgren, and F. Hellman, Appl. Phys. Lett. 94, 212106 (2009).

[32] T. S. Herng, S. P. Lau, L. Wang, B. C. Zhao, S. F. Yu, M. Tanemura, A. Akaike, and K. S. Teng, Appl. Phys. Lett. 95, 012505 (2009).

[33] T. S. Herng, S. P. Lau, C. S. Wei, L. Wang, B. C. Zhao, M. Tanemura, and Y. Akaike, Appl. Phys. Lett. 95, 133103 (2009).

[34] R. P. Panguluri, P. Kharel, C. Sudakar, R. Naik, R. Suryanarayanan, V. M. Naik, A. G. Petukhov, B. Nadgorny, and G. Lawes, Phys. Rev. B. 79, 165208 (2009).

[35] R. J. Soulen Jr., J. M. Byers, M. S. Osofsky, B. Nadgorny, T.Ambrose, S. F. Cheng, P. R. Broussard, C. T. Tanaka, J. Nowak, J. S. Moodera, A. Barry, and J. M. D. Coey, Science 282, 85 (1998).

[36] S. K. Upadhyay, A. Palanisami, R. N. Louie, and R. A. Buhrman, Phys. Rev. Lett.

81, 3247 (1998).

[37] P. Chalsani, S. K. Upadhyay, O. Ozatay, and R. A. Buhrman, Phys. Rev. B 75, 094417 (2007).

[38] R. P. Panguluri, K. C. Ku, T. Wojtowicz, X. Liu, J. K. Furdyna, Y. B. Lyanda-Geller, N. Samarth, and B. Nadgorny, Phys. Rev. B 72, 054510 (2005).

[39] J. G. Braden, J. S. Parker, P. Xiong, S. H. Chun, and N. Samarth, Phys. Rev. Lett. 91, 056602 (2003).

[40] J. F. Janak, Phys. Rev. B 16, 255 (1977).

[41] R. P. Panguluri, P. Kharel, C. Sudakar, R. Naik, R. Suryanarayanan, V. M. Naik, A. G. Petukhov, B. Nadgorny, and G. Lawes, Phys. Rev. B 79, 165208 (2009).

[42] J. Wunderlich, B. G. Park, A. C. Irvine, L. P. Zârbo, E. Rozkotová, P. Nemec, V. Novák, J. Sinova, T. Jungwirth, Science, 24, 1801 (2010).

[43] G. Xing, D. Wang, J. Yi, L. Yang, M. Gao, M. He, J. Yang, J. Ding, T. Chien, and T. Wu, Appl. Phys. Lett. 96, 112511 (2010).

[44] J. B. Yi, H. Pan, J. Y. Lin, J. Ding, Y. P. Feng, S. Thongmee, T. Liu, H. Gong, and L. Wang, Adv. Mater. 20, 1170 (2008).

Chapter 5 ZnO-based Thin Film Transistors on SiO$_2$/Si Substrate

5.1 Introduction

Solution-processed thin-film semiconductors can potentially enable low-cost thin-film transistor (TFT) arrays/circuits via mass manufacturing roll-to-roll processes using a combination of conventional coating and printing techniques (e.g., blade and dip coating, screen and inkjet printing, etc) [1-7]. Many soluble organic semiconductors have thus been explored for this purpose, but their functional performances generally fall short of expectation in addition to other process complications. Low mobility, low current density, process-dependent performance variations, and reliability issues are among the critical deficiencies with these materials. On the other hand, inorganic materials such as metal chalcogenides [4-6] have been solution processed into high-mobility thin-film semiconductors, but their inherent toxicity and extreme sensitivities to ambient oxygen and moisture overshadow their performance attributes. Most recently, a thin-film polysilicon semiconductor via thermal decomposition of a solution-deposited silane precursor has been reported [7]. High field-effect transistor (FET) mobilities reaching ~ 6.5 cm^2 V^{-1} s^{-1} and ~ 100 cm^2 V^{-1} s^{-1} were achieved for ink-jet printed and spin-coated devices, respectively. However, the attainment of high mobility in this approach relied on a post-deposition laser-induced crystallization of amorphous silicon films generated from thermal decomposition of a silane precursor. Accordingly, this process is essentially similar to conventional polysilicon technology which is still beset with process complications such as uniformity issues.

ZnO is a nontoxic inorganic semiconductor which may also offer such salient features as high mobility, excellent environmental stability, and high transparency. ZnO thin-film semiconductors prepared by radio frequency magnetron sputtering in delicately controlled environments [8] have shown high FET mobility (> 30 cm^2 V^{-1}

s^{-1}), but this technique is not likely to be compatible with low-cost TFT manufacturing processes. In addition, TFTs fabricated by this technique generally failed after several measurements. Most recently, solution- processed zinc oxide FET electron mobility reached 5.25 $cm^2 V^{-1}s^{-1}$ with a high on-off ratio [9]. This was achieved using processes including three high-temperature annealing steps, a proprietary sputtered mixed oxide dielectric (aluminum titanium oxide), and a less stable, more difficult to deposit source/drain metal (Zn). In another study, a more complex oxide semiconductor FET reached a mobility of 16.0 $cm^2 V^{-1} s^{-1}$ [10].

In this chapter, we use the common SiO_2 as the gate dielectric, which is a mature and widely studied material. What is more important, utilizing SiO_2 as the gate dielectric is much more easily incorporated into current Si industry. Unlike previous TFTs obtained by the spin-coating which requires multiple spin-coatings (3 times or more) of semiconductor precursor with different concentrations and each spin-coating must be followed by a high temperature annealing process, this work is going to find out the easiest and most simplified fabrication process. A careful investigation on the influence exerted on TFT performance by precursor concentration, times of spin-coating, annealing ambient and annealing temperature is conducted. Although the mobility is slightly compromised, it concentrates on facile and practical fabrication process rather than single parameter of the mobility alone. It is of great significance in future applications. In addition, various dopants are tried to improve the mobility while maintaining the process simplicity.

5.2 Parameters influencing field effect properties of un-doped ZnO thin films

To be compatible with present silicon based technology, we use thermally oxidized Si as the gate dielectric. The thickness is 300 nm, and the unit area capacitance is calculated to be 10 nF·cm^{-2}. Highly doped Si is used as the global gate and the resistivity is 0.001 Ω-cm. The whole device fabrication flow chart is shown in Fig.5-2-1.
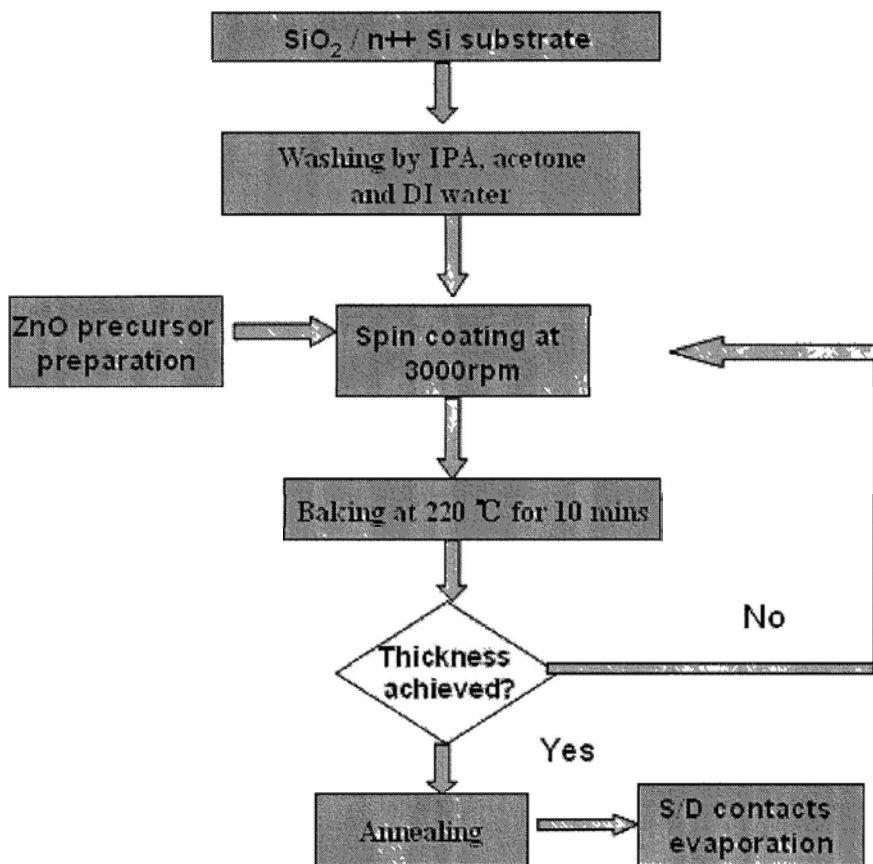
Fig.5-2-1 ZnO TFT device fabrication process.

The typical bottom gate top contact structure is schematically shown in Fig. 5-2-2.
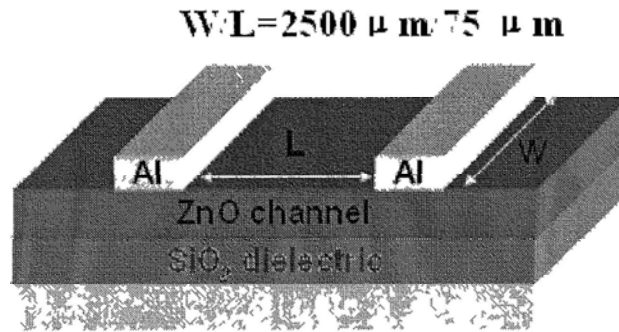
Fig.5-2-2 Schematic diagram of ZnO thin film transistor. The channel layer is prepared by spin-coating method.

To get the optimized conditions for the best device performance, the factors including these below would be discussed, respectively.

a annealing temperatures;

b annealing ambient;

c precursor concentration;

d repeating times of coatings.

5.2.1 Annealing temperature

0.1 M ZnO precursor is prepared in the following way. 0.4585g zinc acetate (99.99 %) is dissolved in 2-methoxyethanol. A transparent clear solution is obtained after stirring it at 55 °C for 2 hours. Three devices are fabricated by twice spin-coating of the active ZnO layer. Three such prepared thin films are annealed at 400 °C, 500 °C and 600 °C for one hour in air, respectively. The whole process is shown clearly in Fig.5-2-1. The channel dimension is $W/L= 2500$ μm/75 μm in all of the TFT studies, unless stated specifically. The thickness of the aluminum electrodes is approximately equal to 150 nm.

The largest mobility is obtained at 600 °C. Its output and transfer characteristics are shown in Fig.5-2-3.
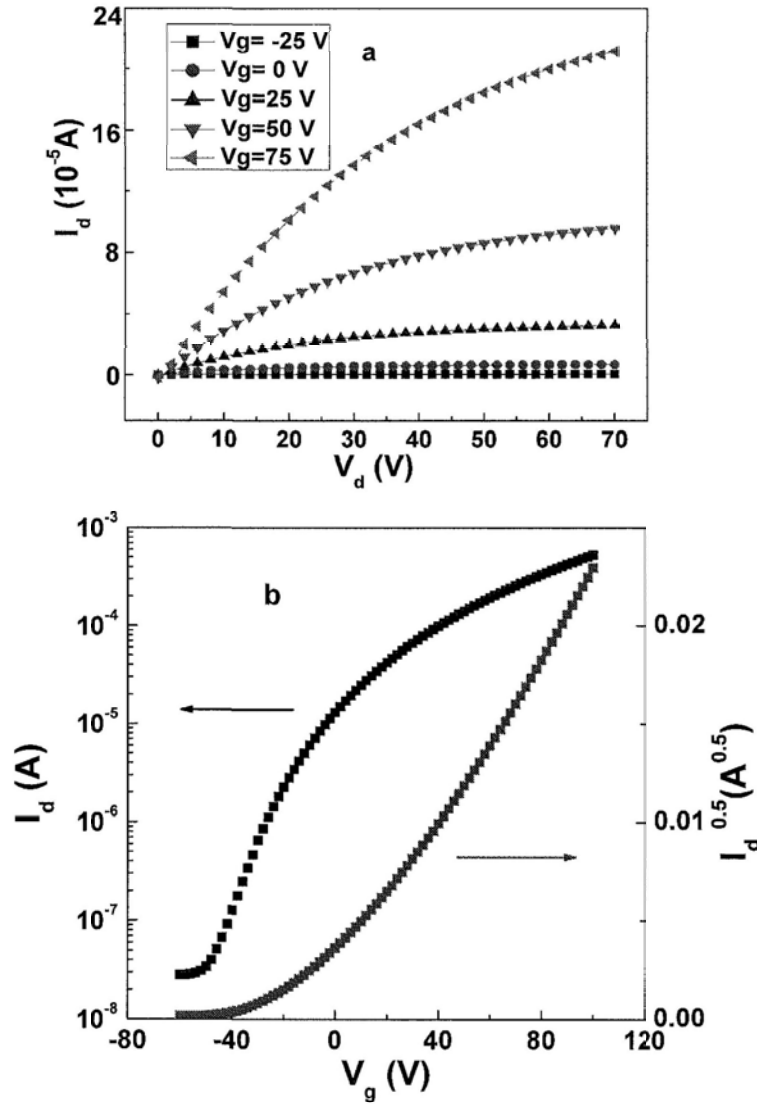
Fig.5-2-3 Output (a) and transfer (b) plots of ZnO TFT. The ZnO thin film is annealed at 600 °C for 1 hour in air.

The carrier mobility can be calculated with the conventional metal-oxide-semiconductor field effect transistor model for drain-source current I_d:

$$I_d = \frac{W}{2L} \mu C_i (V_g - V_{th})^2$$

$$(5\text{-}1)$$

where W and L are the width and length of the channel, respectively, V_g is gate voltage, V_{th} is threshold voltage and C_i is the capacitance per unit area, and μ is the saturation field effect mobility, which is extracted from the saturation region of the transfer curves. The slope of $I_d^{1/2}$ versus V_g gives the mobility and the intercept at $I_d^{1/2} = 0$ determines the threshold voltage.

Respective transfer plot of ZnO TFTs annealed at 400 °C and 500 °C are shown in Fig.5-2-4.
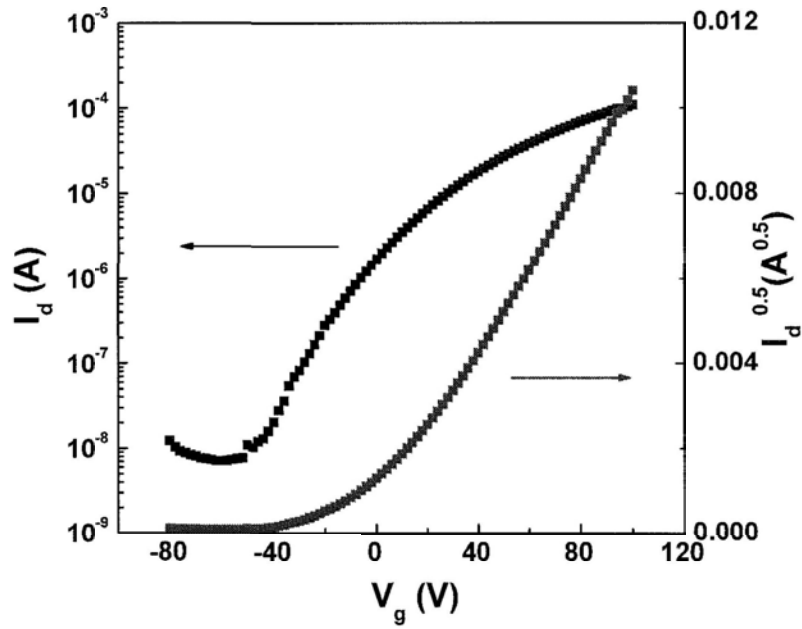
Fig.5-2-4 Transfer characteristics of ZnO TFT with the active layer annealed at 400 °C for 1 hour in air.
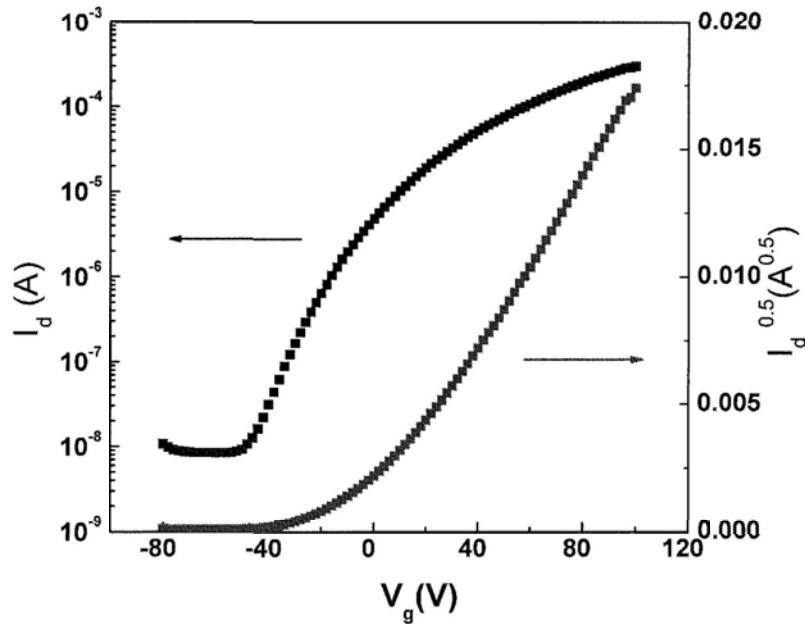
Fig.5-2-5 Transfer characteristics of ZnO TFT with the active layer annealed at 500 °C for 1 hour in air.

Table 5-2-1 shows the summary of extracted mobility, threshold voltage, and on-off ratio annealed at 400 °C, 500 °C and 600 °C respectively.

Table 5-2-1 Field effect properties of ZnO thin films annealed at various temperatures.

Annealing temperature (°C)	μ, mobility $(cm^2V^{-1}s^{-1})$	V_{th}, threshold voltage (V)	On-off ratio
400	0.06	3	2×10^4
500	0.11	3	4×10^4
600	0.27	0	2×10^4

It is obvious that, as the annealing temperature increases, the mobility increases markedly. This is due to better crystallization at higher annealing temperatures. Contributions due to scattering by defects or grain boundaries are diminished. Although the mobility is not very large, it might be improved with proper annealing process controls, as reported in Ref. [9]. However, the complex process is not compatible with cost effectiveness and throughput requirements.

5.2.2 Annealing ambient.

The annealing environment is very important for the crystallization process and the electrical performance is significantly influenced by annealing ambient. In this section, ZnO thin films are prepared in the same way as aforementioned in Section 5.2.1. Additional two pieces are annealed in N_2 (99.99%) and Ar (99.99%), respectively. The annealing temperature is kept the same at 600 °C, and the duration is one hour.

Fig. 5-2-6 and Fig. 5-2-7 show the transfer plots of ZnO TFTs annealed in N_2 and Ar, respectively.
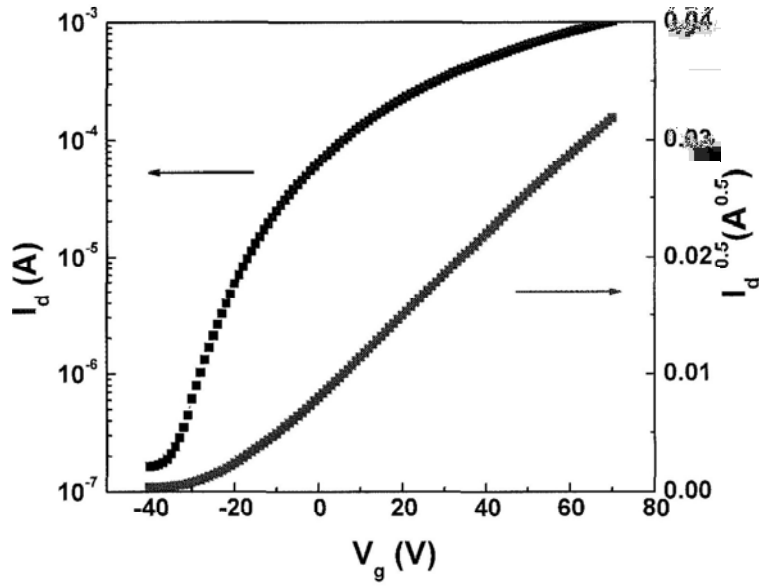
Fig.5-2-6 Transfer characteristics of ZnO TFT with the active layer annealed in N_2 for 1 hour at 600 °C.
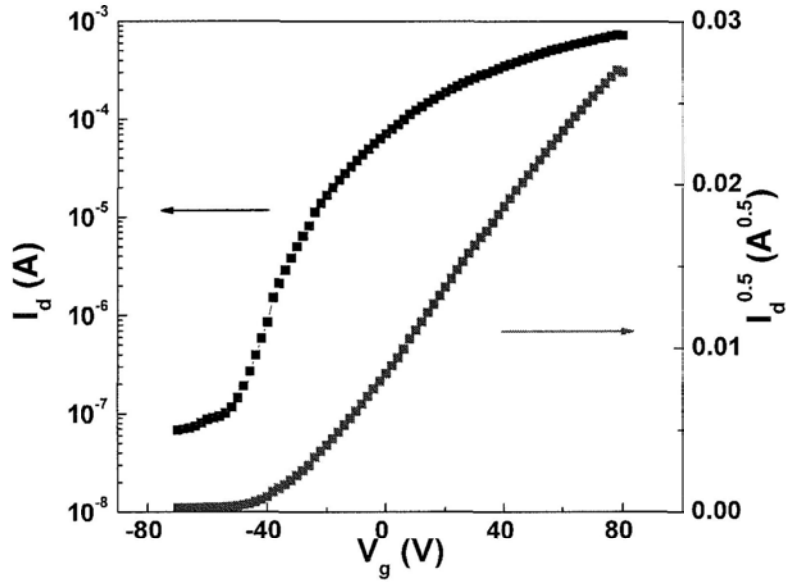
Fig.5-2-7 Transfer characteristics of ZnO TFT with the active layer annealed in Ar for 1 hour at 600 °C.

The mobility, threshold voltage and on-off ratio are summarized in Table 5-2-2, in comparison with the annealing in air, as discussed in Section 5.2.1.

Table 5-2-2 Field effect properties of ZnO thin films annealed with different gases.

Annealing ambient	μ, mobility $(cm^2V^{-1}s^{-1})$	V_{th}, threshold voltage (V)	On-off ratio
air	0.27	0	2×10^4
N$_2$	0.46	-22	0.7×10^4
Ar	0.33	-30	0.8×10^4

It can be observed that the mobility increases in annealing in N$_2$ and Ar, compared with that in air. This is in qualitative agreement with the discussion in Section 3.3 in Chapter 3. More oxygen vacancies are created when annealed in N$_2$ or Ar, which serve as the one of main donor defects in ZnO. Therefore, the electron concentration is expected to increase, and the mobility increases when ZnO thin films are annealed in N$_2$ or Ar. However, it is noted that the threshold voltage is shifted negatively greatly, and the current on-off ratio decreases accordingly.

In practical applications, the threshold voltage is required to be positively close to 0 to save the static energy consumption. Therefore, the overall device performance of ZnO annealed in air is more appealing, although the mobility is slightly smaller.

5.2.3 Precursor concentration

The interface between the active channel layer and SiO$_2$ dielectric is crucial for transistor performance. The precursor concentration and repeating times have much impact on the interface quality. ZnO TFTs are fabricated with precursors of different concentrations, 0.05 M, 0.1 M and 0.2 M, following the method mentioned in Section 5.2.1. After completion of spin-coatings, films are annealed in air for one hour, and the temperature is kept at 600 °C. Results of the device prepared with the concentr-
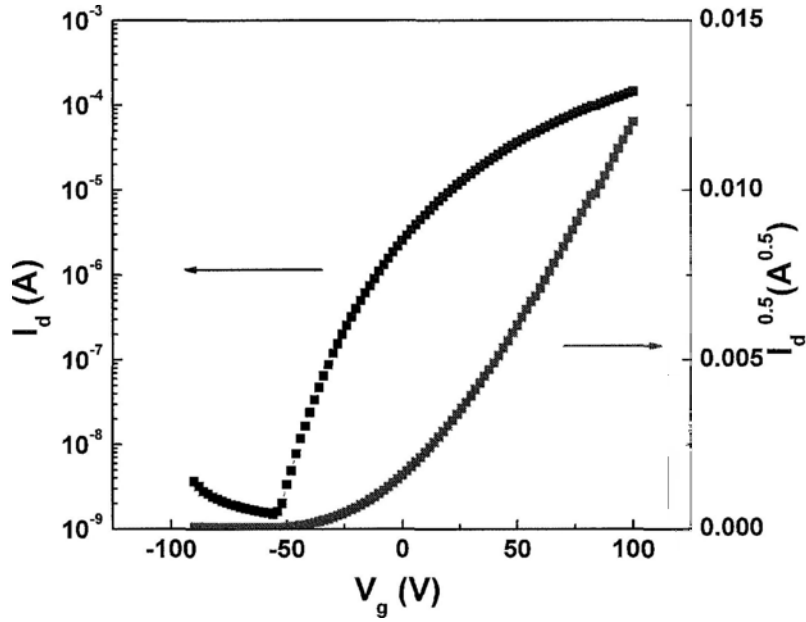
Fig.5-2-8 Transfer characteristics of ZnO TFT. The precursor concentration is 0.05 M. After spin-coating, the thin film is annealed in air at 600 °C for 1 hour.
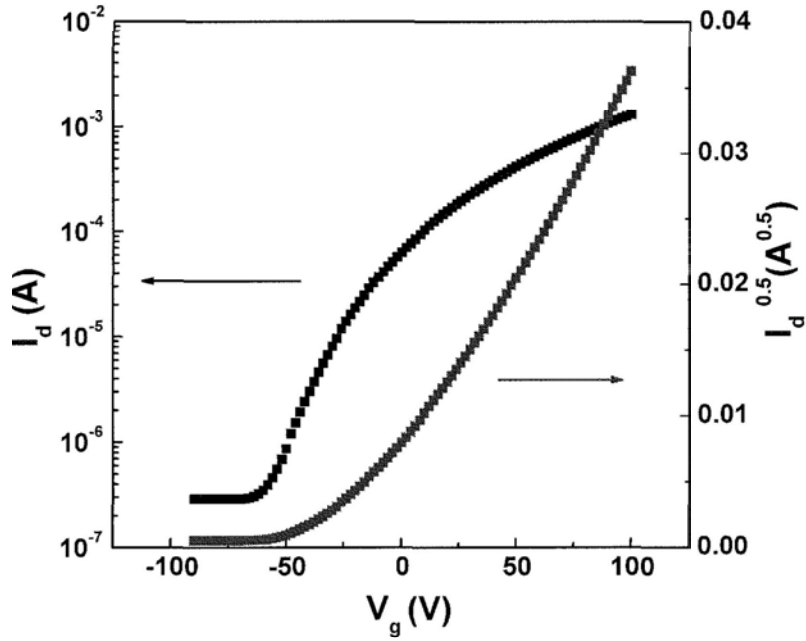
Fig.5-2-9 Transfer characteristics of ZnO TFT. The precursor concentration is 0.2 M. After spin-coating, the thin film is annealed in air at 600 °C for 1 hour.

-ation of 0.1 M has been provided previously. The transfer plots of devices prepared with the concentration of 0.05 M and 0.2 M are demonstrated in Figs. 5-2-8 and 5-2-9.

The field effect mobility, threshold voltage and on-off ratio can be calculated in the same way as aforementioned, which are summarized in Table 5-2-3.

Table 5-2-3 Field effect properties of ZnO thin films prepared with different precursor concentrations.

Precursor Concentration (M)	μ, mobility $(cm^2V^{-1}s^{-1})$	V_{th}, threshold voltage (V)	On-off ratio
0.05	0.07	0	7×10^4
0.1	0.27	0	2×10^4
0.2	0.32	-22	0.6×10^4

It can be found that the mobility increases with increasing the precursor concentration. However, beyond 0.1 M, the increase almost saturates. The coverage and film formation might be deteriorated, if the concentration is too low. It is noted that the baking temperature in the present study is high compared to other work. The high baking temperature induces fast nucleation and crystallization. The influence of baking temperature on nucleation and crystallization has been reported previously [11]. Beyond 0.1 M, the coverage and the nucleation process changes little with the increase of precursor concentration. It is also noted that at the concentration of 0.2 M, the current on-off ratio is diminished, and the threshold voltage is shifted to the negative markedly. This may be due to the fact that a larger concentration leads to a thicker ZnO thin film. As the bulk resistance decreases significantly, a more negative gate bias is needed to turn the device off. Therefore, we conclude that from this section, 0.1 M yields the best device with the overall performance parameters.

5.2.4 Repeating times of spin-coating

The coverage and film formation are not only related to the precursor concentration, but also subjected to the times of spin-coatings. In this section, ZnO thin film

transistors are fabricated by the fixed precursor concentration (0.1 M), and the time of spin-coating ranged from 1, 2 and 4. All films are annealed in air at 600 °C or one hour. Other conditions remain unchanged as that in Section 5.2.1. We directly cite the result of twice spin-coating (Fig.5-2-3). Transfer plots of single spin-coating and four times of spin-coating are presented in Fig.5-2-10.
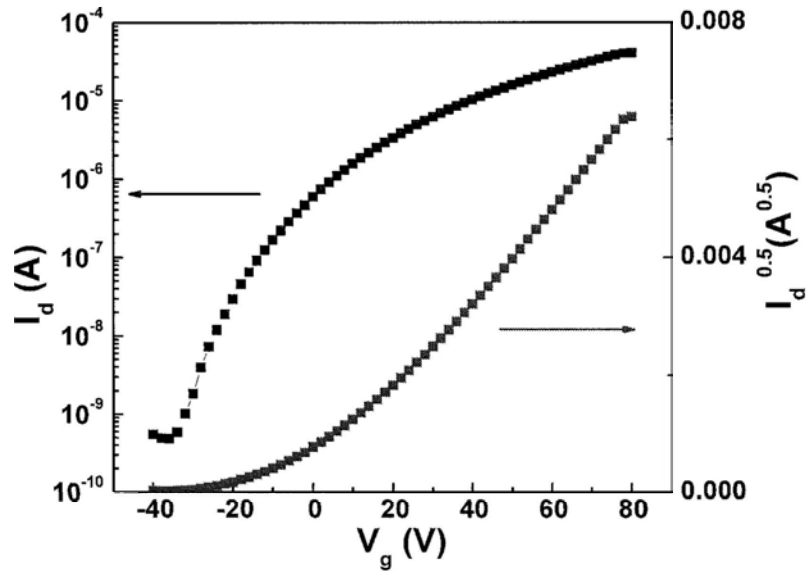
Fig.5-2-10 Transfer characteristics of ZnO TFT. The active layer is formed by one time spin-coating
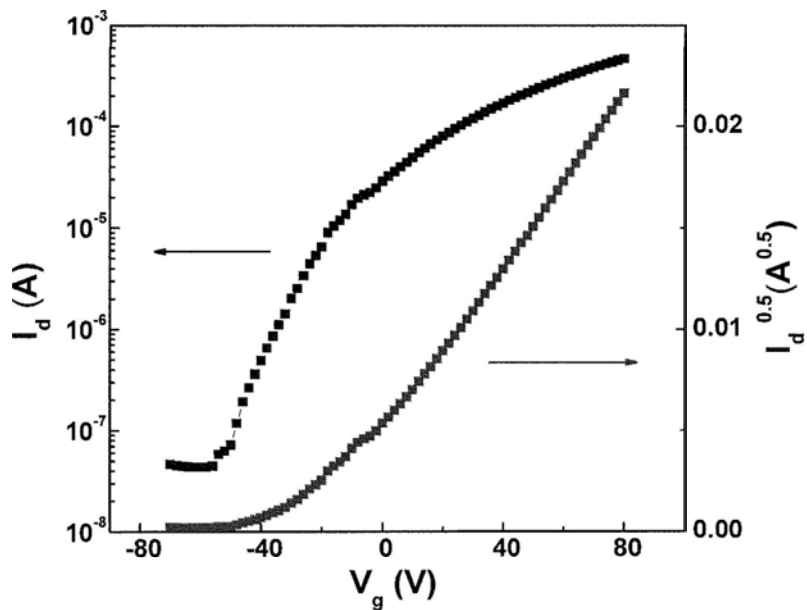
Fig.5-2-11 Transfer characteristics of ZnO TFT. The active layer is formed by four times of

spin-coating.

The field effect mobility, threshold voltage, and on-off ratio are summarized in Table 5-2-4.

Table 5-2-4 Field effect properties of ZnO thin films prepared with different spin coating layers.

Repeating times	μ, mobility $(cm^2V^{-1}s^{-1})$	V_{th}, threshold voltage (V)	On-off ratio
1	0.04	3	9×10^4
2	0.27	0	2×10^4
4	0.30	-18	1×10^4

Similarly, poor coverage and film formation lead to smaller mobility with a single spin-coating layer. With four-times of spin-coating, the mobility increases little, but the on-off ratio diminishes and the threshold voltage shifts negatively seriously due to the increase of film thickness and bulk conductivity. We can find that two-time spin-coating is proper when considering the field effect mobility, the threshold voltage and the current on-off ratio. Similar results have been reported in Ref. [11].

In summary, from previous four sections, we can extract the optimized conditions in Table 5-2-5.

Table 5-2-5 Summary of optimized preparation conditions to achieve the best field effect performance.

Annealing temperature	600 °C
Annealing ambient	air
Precursor concentration	0.1 M
Times of spin-coating	2

5.3 Doped ZnO thin film transistors

In our previous study, the highest mobility of un-doped ZnO thin film transistors is less than one, which is far smaller than other devices fabricated by vacuum based technology, such as pulsed laser deposition and magnetron sputtering. Although the mobility obtained by solution method may not compete against vacuum based technology, it can be improved significantly. Doping is an effective way to increase the mobility, because the mobility increases with the carrier concentration in the following way:

$$\mu = \mu_0 \, (n/n_0) \tag{5-2}$$

where μ_0 is the free carrier mobility, n is the free carrier concentration, and n_0 is the total induced charge carriers. [12]. Meanwhile, p-type doping in ZnO has been a big challenge ever since. Although doping by N or Li has been reported to show p-type conductivity [13,14], however its reproducibility is very poor. What is more, p-type field effect performance in ZnO thin film transistors has never been reported yet. Therefore, we chose Li and N to confirm if p-type field effect could be observed. These two elements have been reported to be effective in inducing p-type conductivity by hall-effect measurement.

Li doped ZnO thin film transistor is fabricated following the optimized conditions in previous parts for un-doped ZnO thin film transistors except the composition of the precursor, which is prepared by dissolving zinc acetate (99.99 %) and lithium acetate dihydrate (99.999 %) in 2-methoxyethanol before stirring for two hours at 55 °C. The total metal concentration is 0.1 M, and the ratio of Zn to Li is 95: 5. The precursor is spin-coated onto the cleaned substrate, followed by baking at 220 °C for 10 minutes. The coating and baking cycle is repeated once more. Then, the film is annealed at 600 °C for one hour in air. Source and drain contacts are deposited by thermal evaporation of Al as aforementioned.

The precursor for N doped ZnO thin film transistor is prepared in the following way. Zinc acetate (99.99 %) and ammonium acetate (99.99 %) are dissolved in 2-methoxyethanol before stirring for two hours at 55 °C. The ratio of zinc to

ammonium is 0.1 M: 0.3 M. Other conditions for device fabrication are the same as above.

Figs. 5-3-1 and 5-3-2 show the output and transfer characteristics of Li-doped and N-doped ZnO thin film transistors, respectively.
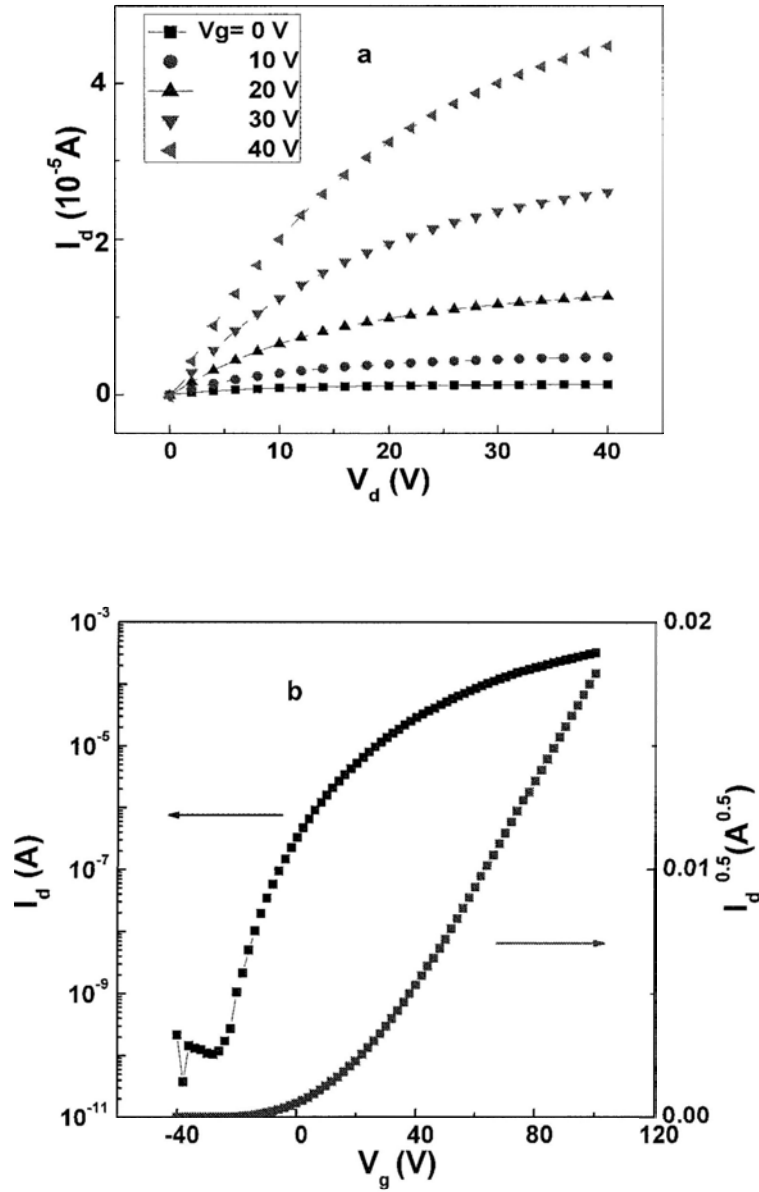
Fig.5-3-1 Output (a) and transfer (b) plots of ZnLiO TFT. The doping concentration is 5 %. The film is annealed in air at 600 °C for one hour.
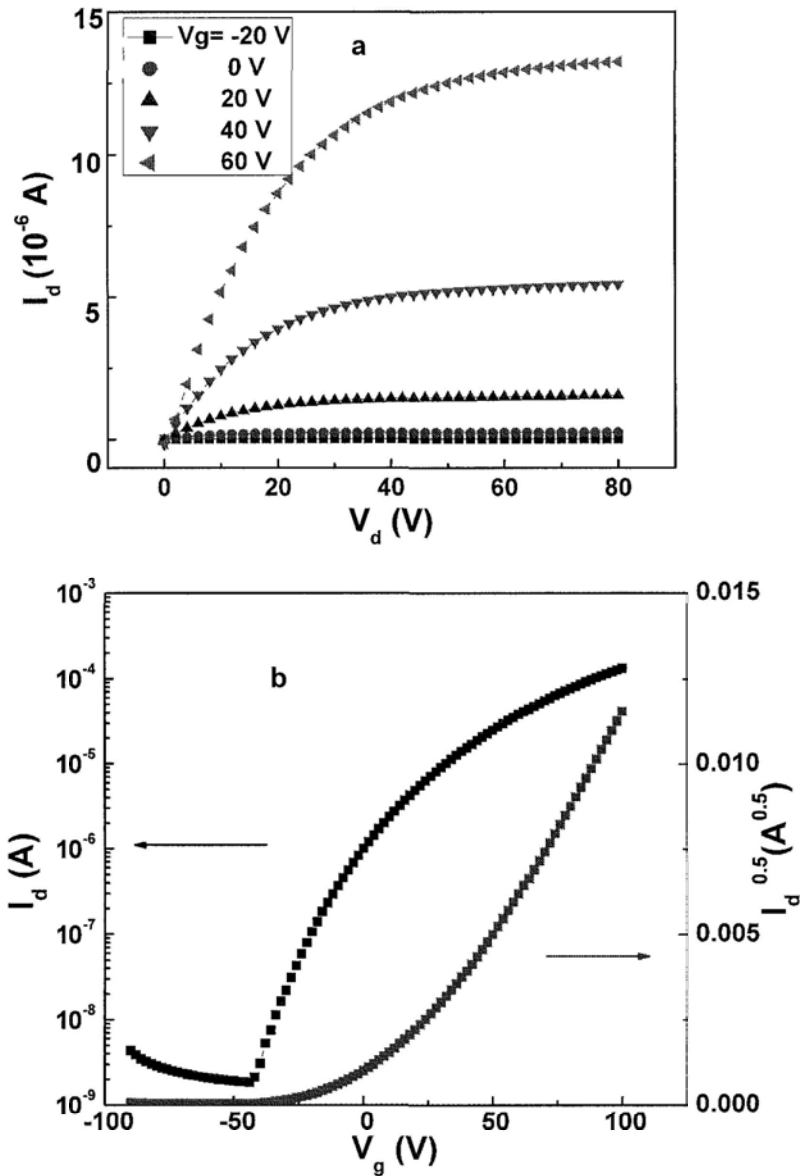
Fig.5-3-2 Output (a) and transfer (b) characteristics of N doped ZnO TFT.

From both output curves of Li-doped and N doped ZnO TFT, typical n-type field effect could be clearly observed, opposite to the findings of previously mentioned in Refs. [13,14]. The reason may be the deactivation of the acceptors, or compensation effects by donor defects. Both devices work in enhancement mode.

The field effect mobility, threshold voltage and current on-off ratio of both devices are summarized in Table 5-3-1.

Table 5-3-1 Field effect properties of ZnO thin films by different element doping

	μ, mobility (cm^2 V^{-1}s^{-1})	V_{th}, threshold voltage (V)	On-off ratio
Li-doped	0.24	16	3×10^6
N-doped	0.08	15	5×10^4

Compared with un-doped ZnO TFT, the mobility is not improved, or even diminished. Attempts by Hall effect (Machine model: HL5500) to confirm the carrier nature are tried, but failed, because of too large resistance of these samples. Four point probe measurement of Li-doped ZnO gave typical resistivity of ~ 500 Ω-cm, which is on the same order of magnitude as that of un-doped ZnO. For N-doped ZnO, the resistivity is even larger. It is noted that after doping by N or Li, the threshold voltage is shifted to the positive side greatly. This may serve as evidence that acceptor energy levels have been introduced by N or Li. When the gate voltage increases, these acceptor levels should be filled in before the channel is turned on, therefore the threshold voltage of Li or N doped ZnO increases as compared to the un-doped ZnO. This finding is in good agreement with the previous report [15]. Although we adopted similar preparation method, because of the complex defect scenario or poor reproducibility of ZnO, p-type acceptors might be introduced, but not enough to exhibit p-type field-effect performance, which still needs tremendous efforts to be accomplished.

On the other hand, the role of doping by Li can be obtained by comparing the subthreshold voltage swing before and after the doping. Through calculation, the respective values are 16 V/decade and 8 V/decade for un-doped and Li-doped ZnO thin films.

$$S = \frac{dV_g}{d(\log I_d)} \quad (5\text{-}3)$$

The subthreshold voltage swing serves as an indicator of the interface quality between the semiconductor channel and the dielectric materials [15]. Therefore,

although doping by Li cannot increase the electron mobility, it is helpful to improve the interface quality between the channel and the dielectric.

To study the role of Li on the field-effect performance, we measured the same Li doped and un-doped ZnO TFT after they have been stored in a dry cabinet for 6 months. The transfer plots are shown in Fig. 5-3-3.
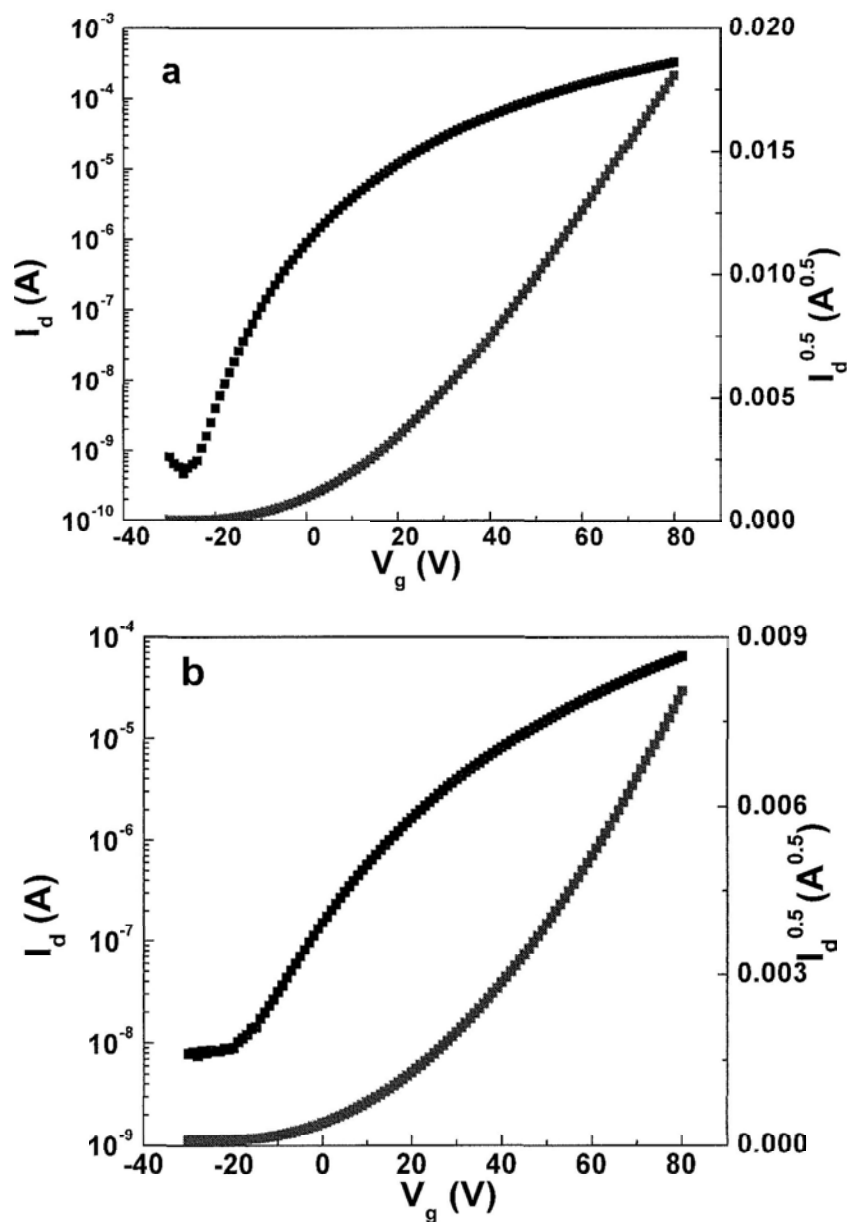
Fig.5-3-3 Transfer plots of Li-doped and un-doped ZnO TFTs measured 6 months after the fabrication.

As a comparison, the field effect properties can be summarized in the Table 5-3-2.

118

Table 5-3-2 Summary of field effect properties of un-doped and Li-doped ZnO thin films measured after the initial fabrication and 6 months later.

	μ, mobility $(cm^2V^{-1}s^{-1})$	V_{th}, threshold voltage (V)	On-off ratio
Un-doped ZnO	0.27	0	2×10^4
Un-doped ZnO (after 6 months)	0.13	17	1×10^4
Li doped ZnO	0.24	16	3×10^6
Li doped (after 6 months)	0.22	14	7×10^5

It can be found that with Li doping, the field effect performances show much smaller degradation than that of the un-doped after 6 months storage. Therefore, the doping of Li can increase the stability of devices, which is due to the larger background conductivity after doping by Li, and it also may be attributed to the formation of a better channel and gate dielectric interface due to Li doping [15].

To increase the mobility, n-type doping is necessary to increase the electron concentration. Gallium is a commonly used donor. Ga singly doped ZnO can be either metallic or semiconducting [12]. Co-doping by Li can ensure its semiconducting nature.

Ga and Li co-doped ZnO TFT is fabricated in the similar way. The precursor is prepared by dissolving zinc acetate (99.99 %), gallium nitrate hydrate (99.9 %) and lithium acetate dihydrate (99.999 %) in 2-methoxyethanol before stirring for two hours at 55 °C. The total metal concentration is 0.1 M, and Zn: Ga: Li= 93: 2: 5. The film is annealed in air at 600 °C for one hour. Its output and transfer characteristics are shown in Fig.5-3-4.
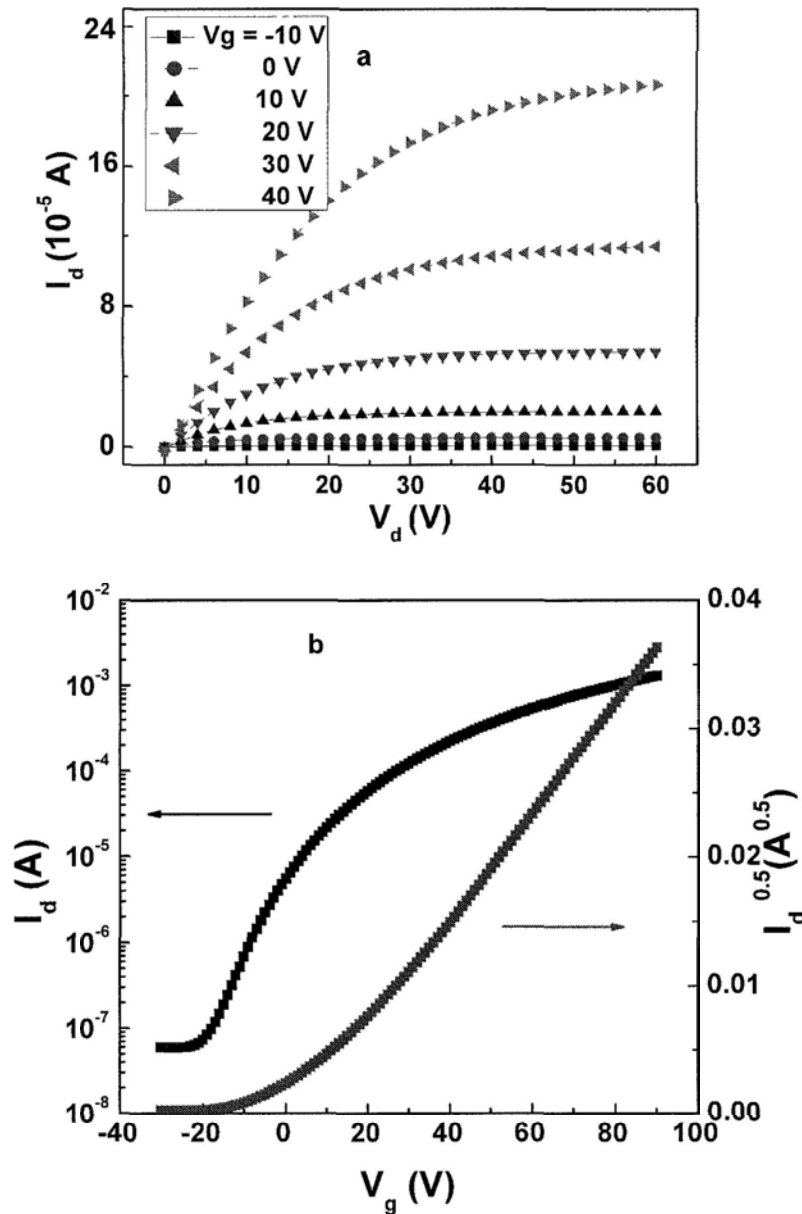
Fig.5-3-4 Output (a) and transfer (b) characteristics of Ga and Li co-doped ZnO TFT.

The field effect mobility, threshold voltage and current on-off ratio are 1.6 cm^2 V^{-1}s^{-1}, 1 V and 3×10^4, respectively. It can be seen that with a small amount of doping by Ga (2 %), the carrier mobility is increased significantly, compared with that of un-doped ZnO based device, which is revealed by the significant decrease of resistivity after doping by Ga. This obtained mobility is comparable or even larger than many other reported values by solution (aqueous) method. [12,16,17]. It is noted that the doping ratio is not optimized yet. By optimizing the doping concentration of each dopant, the mobility may be increased even larger. The process presented is

much easier than most of reported solution method. Only two times of spin-coating are needed, and the annealing control is not stringent, as required in other reports [9].

To conclude this chapter, the field effect performance of the pure ZnO TFT and doped ZnO TFTs prepared under optimized conditions are summarized in Table 5-3-3.

Table 5-3-3 Summary of field effect properties of un-doped and doped ZnO thin films.

	μ, mobility ($cm^2V^{-1}s^{-1}$)	V_{th}, threshold voltage (V)	On-off ratio
Pure ZnO	0.27	0	2×10^4
Li doped ZnO	0.24	16	3×10^6
N doped ZnO	0.08	15	5×10^4
Ga and Li co-doped	1.6	1	3×10^4

References

[1] H. Klauk, *Organic Electronics: Materials, Manufacturing, and Applications*, Wiley-VCH: Weinheim, Germany, 2006.

[2] H. Sirringhaus, Adv. Mater. 17, 2411 (2005).

[3] C. D. Dimitrakopoulos, P. R. Malenfant, AdV. Mater. 14, 99 (2002).

[4] B. A .Ridley, B. Nivi, J. M. Jacobson, Science, 286, 746 (1999).

[5] D. B. Mitzi, L. L. Kosbar, C. E. Murray, M. Copel, A. Afzali, Nature, 428, 299 (2004).

[6] D. V. Talapin, C. B. Murray, Science, 310, 86 (2005).

[7] T. Shimoda, Y. Matsuki, M. Furusawa, T. Aoki, I. Yudasaka, H. Tanaka, H. Iwasawa, D. Wang, M. Miyasaka, Y. Takeuchi, Nature, 440, 784 (2006).

[8] E. Fortunato, P. Barquinha, A. Pimentel, A. Goncalves, A. Marques, L. Pereira, R. Martins, Thin Solid Films, 487, 205 (2005).

[9] B. S. Ong, C. Li, Y. Li, Y. Wu, and R. Loutfy, J. Am. Chem. Soc., 129, 2750 (2007).

[10] Y. J. Chang, D.H. Lee, G. S. Herman, C.H. Chang, Electrochem. Solid State Lett., 10, H135 (2007)

[11] M. Ohyama, H. Kozuka, T. Yoko, Thin Solid Films 306, 78 (1997); B. N. Pal, P. Trottman, J. Sun, and H. E. Katz, Adv. Funct. Mater., 18, 1832 (2008).

[12] W. J. Park, H. S. Shin, B. D. Ahn, G. H. Kim, S. M. Lee, K. H. Kim, and H. J. Kima, Appl. Phys. Lett. 93, 083508 (2008).

[13] Y. Cao, L. Miao, S. Tanemura, M. Tanemura, Y. Kuno, and Y. Hayashi, Appl. Phys. Lett. 88, 251116 (2006).

[14] J. Sann, A. Hofstaetter, D. Pfisterer, J. Stehr, and B. K. Meyer, phys. stat. sol. (c) 3, No. 4, 952 (2006)

[15] P. K. Nayak, J. Jang, C. Lee, Y. Hong, Appl. Phys. Lett. 95, 193503 (2009).

[16] B. J. Norris1, J. Anderson, J. F. Wager, and D. A. Keszler, J. Phys. D: Appl. Phys. 36, L105 (2003).

[17] C. Lia, Y. Li, Y. Wu, B. S. Ong, and R. O. Loutfy, J. Appl. Phys. 102, 076101 (2007).

Chapter 6 Low Voltage Thin Film Transistors with Spin-Coated

Alumina as Gate Dielectric

6.1 Introduction

We have investigated the field effect properties of ZnO based thin film transistors gated by SiO_2 in the preceding chapter. Although a considerably large mobility is obtained by the co-doping of Ga and Li, the device needs to be driven by a high gate bias, which is due to the small unit area capacitance of the SiO_2 dielectric. Supposedly we have a high-k dielectric, the capacitance would be increased. Therefore, with a small gate bias, equivalent amount of carriers can be induced in the active channel layer. The bias needed to drive the device can be significantly reduced, which may lead to the reduction of power consumption tremendously.

In fact, according to the International Technology Roadmap for Semiconductors, the introduction of a high-k material within the gate stack in complementary metal-oxide semiconductor (CMOS) baseline is mandatory in the near future for any kind of application [1]. Previous efforts in search of high-k materials have been focused on metal oxides with a high permittivity such as TiO_2, Ta_2O_5, In_2O_3, HfO_2 and ZrO_2. However, these metal oxides tend to have a narrow bandgap, which leads to a large leakage current [2]. Meanwhile, various organic dielectric materials have been reported to show excellent dielectric properties with a moderate leakage current when incorporated into thin film transistor devices [3,4]. Nevertheless, the preparation of this type of dielectrics usually involves complicated steps and a certain number of chemicals, which are often environmentally unfriendly, and what is even worse, the dielectric itself is poisonous sometimes. Another drawback of these dielectric materials is their poor thermal resistance to high temperature.

Alumina has a dielectric constant almost three times of SiO_2, and it owns

attributes such as non-toxity, transparency, high ambient and thermal stability. The raw materials needed to prepare it are abundant. However, probably due to its relatively small permittivity, alumina has often been ignored in previous research to be used solely as the gate dielectric. Although people have tried to prepare alumina dielectric by atomic layer deposition [5], magnetron sputtering [6] and anodization [7,8], each of these methods suffers from either one or several of the following problems: low throughput, high cost, large leakage current, large driven-voltage, etc.

Solution processed alumina offers many advantages such as equipment simplicity, low cost, and high throughput. To keep the uniformity in the preparation of the channel layer, we choose to prepare alumina as the gate dielectric by spin-coating method. To the best of our knowledge, there have been very few reports of TFTs with spin-coated alumina as the gate dielectric.

6.2 Dielectric properties of spin-coated alumina as the gate dielectric.

Aluminum nitrate nonahydrate (≥98%) is used to prepare alumina precursor Similar to the preparation of ZnO precursor, aluminum nitrate nonahydrate is dissolved in 2-methoxyethanol (≥99.9%) with the concentration of 0.5 M, followed by stirring for 30 minutes at room temperature to form a transparent and clear solution. As the global gate, n-type highly doped Si (n^{++} Si) substrate is ultrasonically washed by iso-propanol for about 15 minutes, before being blown to dry in high purity N$_2$. Alumina precursor is then spin-coated onto n^{++} Si substrate at 3000 rpm for 10 seconds, and then it is baked on a hotplate at 220 °C for 10 minutes. This coating and baking process is repeated once more to form the amorphous alumina. A batch of such samples is such prepared under identical conditions for capacitance measurement,
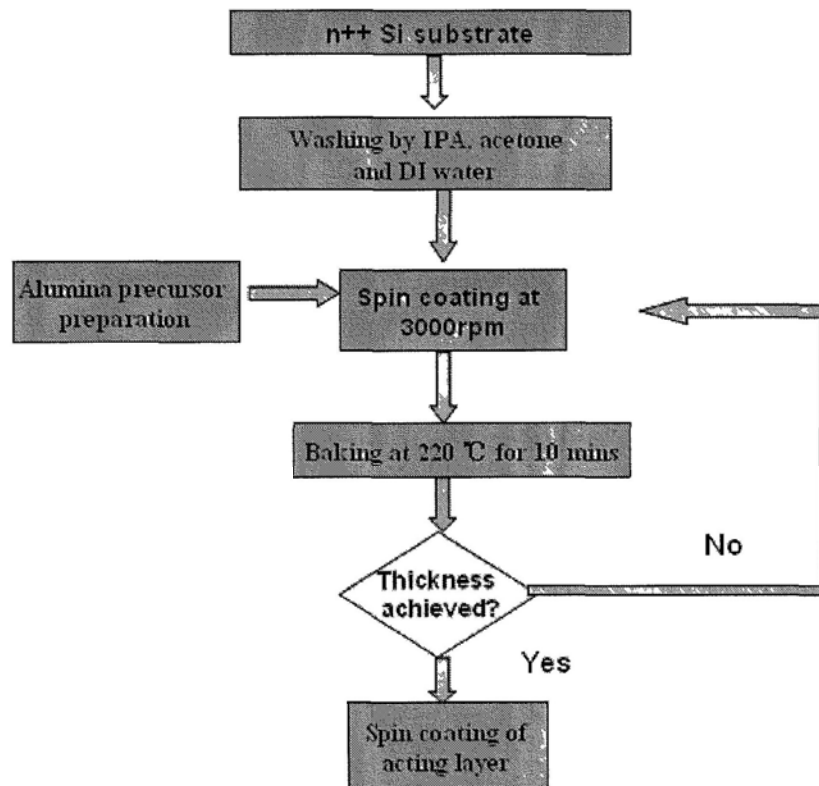
Fig.6-2-1 Alumina dielectric preparation flow chart.

surface morphology observation by atomic force microscopy, or subsequent spin-coating of semiconducting channel layers. The preparation process is schematically shown in Fig. 6-2-1.

The amorphous nature of the prepared alumina thin film is confirmed by x-ray diffraction as shown in Fig.6-2-2. No characteristic peaks can be found.
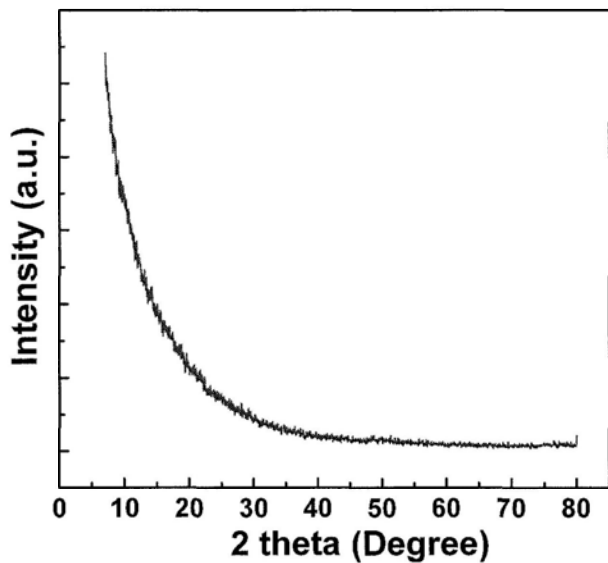
Fig.6-2-2 XRD pattern of spin-coated alumina

Typical surface morphology observed by atomic force microscopy is shown in Fig.6-2-3.
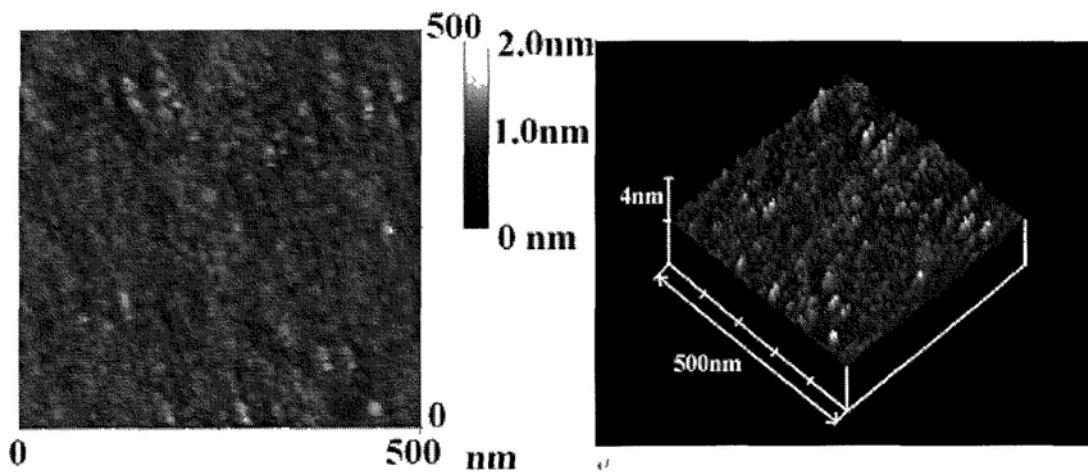
Fig.6-2-3 Surface morphology of spin-coated alumina

The surface morphology is typical of amorphous nature, in agreement with the XRD characterization. The surface is very smooth with the root mean square (rms) roughness of 0.12 nm in the area of 500 nm×500 nm.
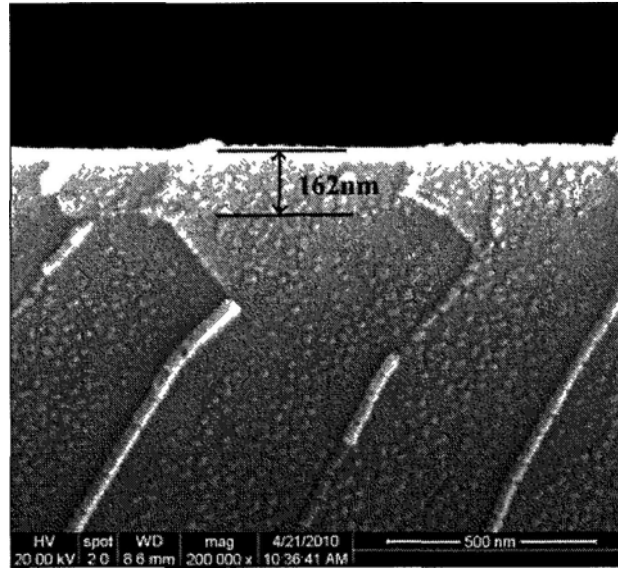
Fig.6-2-4 Cross section view of spin-coated alumina on n^{++} Si

In order to determine the thickness of the prepared alumina layer, field-emission scanning electron microscopy (FE-SEM) is performed for the cross section view, as shown in Fig.6-2-4. It can be found that the thickness is close to 160 nm.

To measure the capacitance of spin-coated alumina, aluminum is thermally evaporated onto alumina as top electrode through shadow masks. n^{++} Si served as the bottom electrode. The diameter of the top electrode is 1 mm. We measured several pieces to examine the reproducibility.
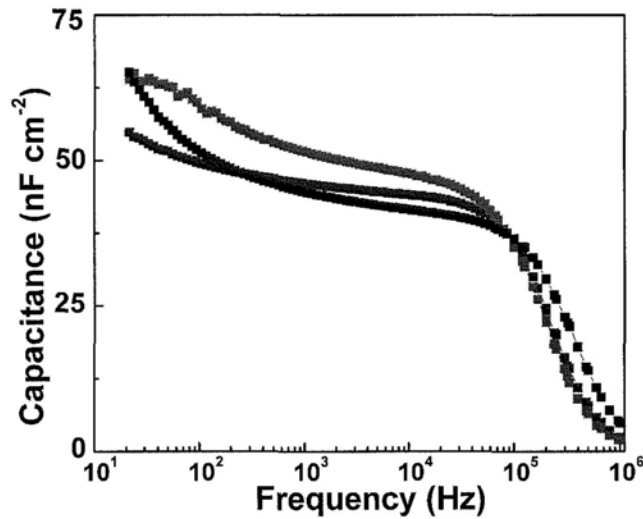
Fig.6-2-5 Unit area capacitance dependence on frequency of spin-coated alumina in Al/Al$_2$O$_3$/n^{++} Si

We take the average value of capacitance at 20 Hz, which is 57 nF·cm^{-2}. Taking into account the thickness obtained by SEM, we can calculate the dielectric constant of the spin-coated alumina, which is found to be 10. The dielectric constant of alumina usually referred to is 9.2. They are in close agreement.

As a gate dielectric, the leakage current should be as small as possible to achieve the best performance of field effect transistors. The current density dependence on voltage in the same Al/Al$_2$O$_3$/n^{++} Si structure is shown in Fig.6-2-6. The electrode is a circle with the diameter of 1 mm as aforementioned.
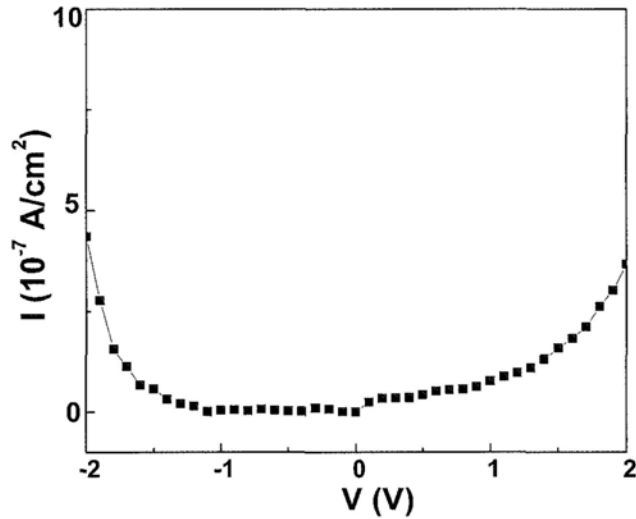
Fig.6-2-6 Current density dependence on voltage in Al/Al$_2$O$_3$/n^{++} Si.

It can be seen that when the bias is below 2 V, the leakage current density is no larger than 5 $\times 10^{-7}$ A $\cdot$cm^{-2}. This leakage current density is comparable to that of many reported dielectric used for low driven-voltage applications [9,10].

It is interesting to note that we find the capacitance of spin-coated alumina changes when the prepared precursor solution is aged for different periods of time. We also conducted the spin-coating of alumina after the prepared precursor is aged for 24 hours and 48 hours. Three or two pieces in each batch are measured. The results are shown in Figs. 6-2-7 and 6-2-8, respectively. These three kinds of dielectrics are named Dielectrics A, B and C respectively.
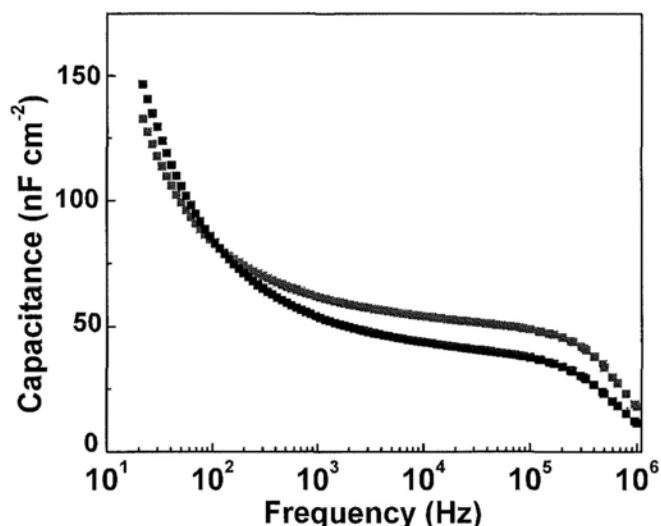
Fig.6-2-7 Capacitance dependence on frequency of alumina spin-coated after 24 hour age of the prepared alumina precursor (Dielectric B)
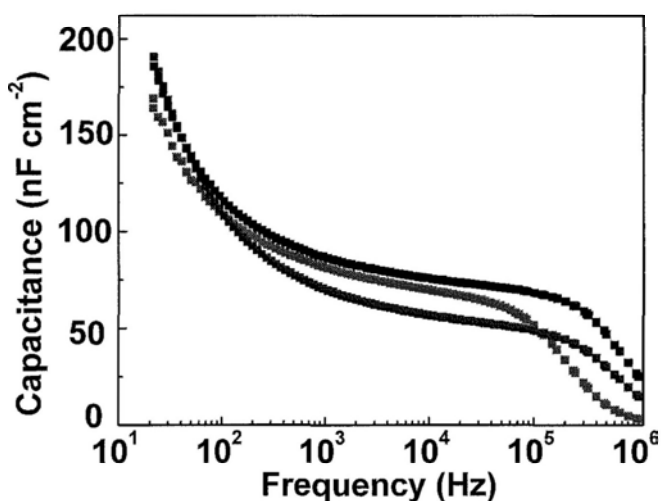
Fig.6-2-8 Capacitance dependence on frequency of alumina spin-coated after 48 hour aging of the prepared alumina precursor (Dielectric C).

It can be found that the respective average capacitance at 20 Hz after 24 hour aging and 48 hour aging is 133 nF·cm^{-2} and 170 nF·cm^{-2}. For every single batch prepared at the same time, the capacitance is still quite stable, and the error is no larger than 10 %. The reason of the frequency discrepancy is not clear yet. It is speculated that the precursor may undergo gelation or agglomeration during the aging process, which implies that a proper stabilizer may be useful to keep the precursor stable. Another interesting feature of the capacitance versus frequency curves is that at

medium frequency (between 100 Hz to 100000 Hz), the capacitance changes little, while at frequency below 100 Hz , the capacitance changes dramatically. Similar capacitance dependence on frequency has been reported before [11,12]. The reason has been possibly attributed to the presence of protons. More evidence in favor of this assumption will be provided in the following discussion.

6.3 ZnO-based thin film transistors with spin-coated alumina as gate dielectric

After alumina is spin-coated onto n^{++} Si substrate, ZnO-based semiconducting layers can be deposited by the similar spin-coating method. From the conclusions drawn in the preceding chapter, it is known that doped ZnO TFTs exhibit larger mobilities. We use Ga singly doped and Ga, Li co-doped ZnO as the semiconducting channel layers to fabricate devices, respectively.

0.1M (total metal concentration) Ga and Li doped ZnO (ZnGaO and ZnGaLiO) precursor is obtained by dissolving zinc acetate (99.99%), gallium nitrate hydrate (99.9%) and lithium acetate dihydrate (99.999 %) in 2-methoxyethanol before stirring for two hours at 55 °C. For Ga singly doped ZnO (ZnGaO), as well as Ga and Li co-doped ZnO (ZnGaLiO), the metal ratios are Zn: Ga = 98 %: 2 % and Zn: Ga: Li = 93%: 2%: 5%, respectively. ZnGaO or ZnGaLiO precursor is carefully spin-coated onto alumina dielectric at 3000 rpm for 10 seconds, and then it is baked at 220 °C for 10 minutes. The coating and baking process is repeated once more to form the required semiconducting layer. The condition and process of the active channel layer formation and alumina dielectric layer are identical, which is beneficial to increase the throughput tremendously, and greatly simplifed the whole device fabrication. Both ZnGaO and ZnGaLiO thin films are annealed in air at 600 °C for half an hour. Aluminum is thermally evaporated onto doped ZnO thin films by shadow masks to form source and drain contacts.

The whole device fabrication starting from alumina coated n^{++} Si substrate is schematically shown in Fig.6-3-1.
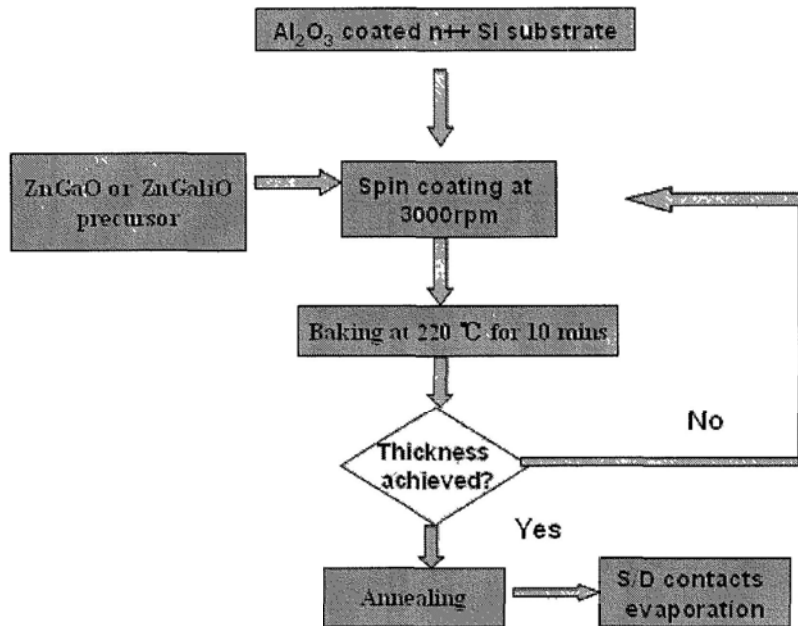
Fig.6-3-1 Schematic diagram of device fabrication process starting from alumina coated n^{++} Si substrate

The typical device structure is shown in Fig.6-3-2.
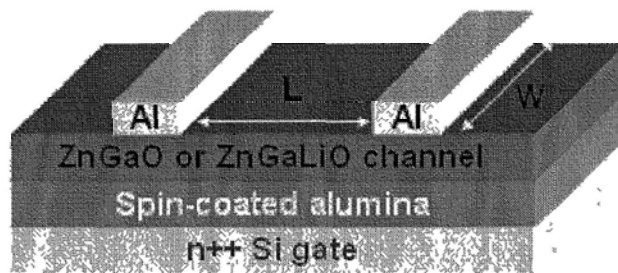
Fig.6-3-2 Typical transistor structure with spin-coated alumina as gate dielectric.

The output curve and transfer characteristics of ZnGaO based TFT and ZnGaLiO based TFT are shown respectively in Fig.6-3-3 and Fig.6-3-4.
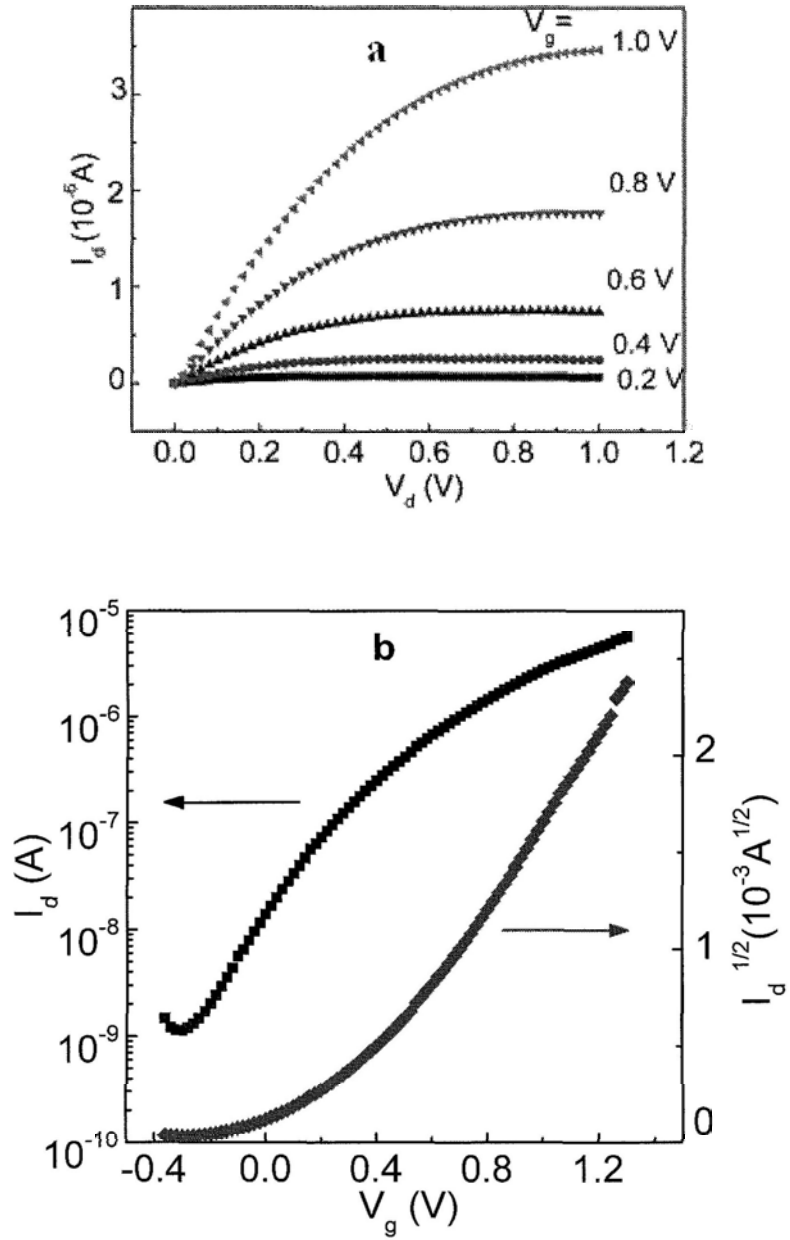
Fig.6-3-3 Output (a) and transfer (b) characteristics of ZnGaO thin film transistor.
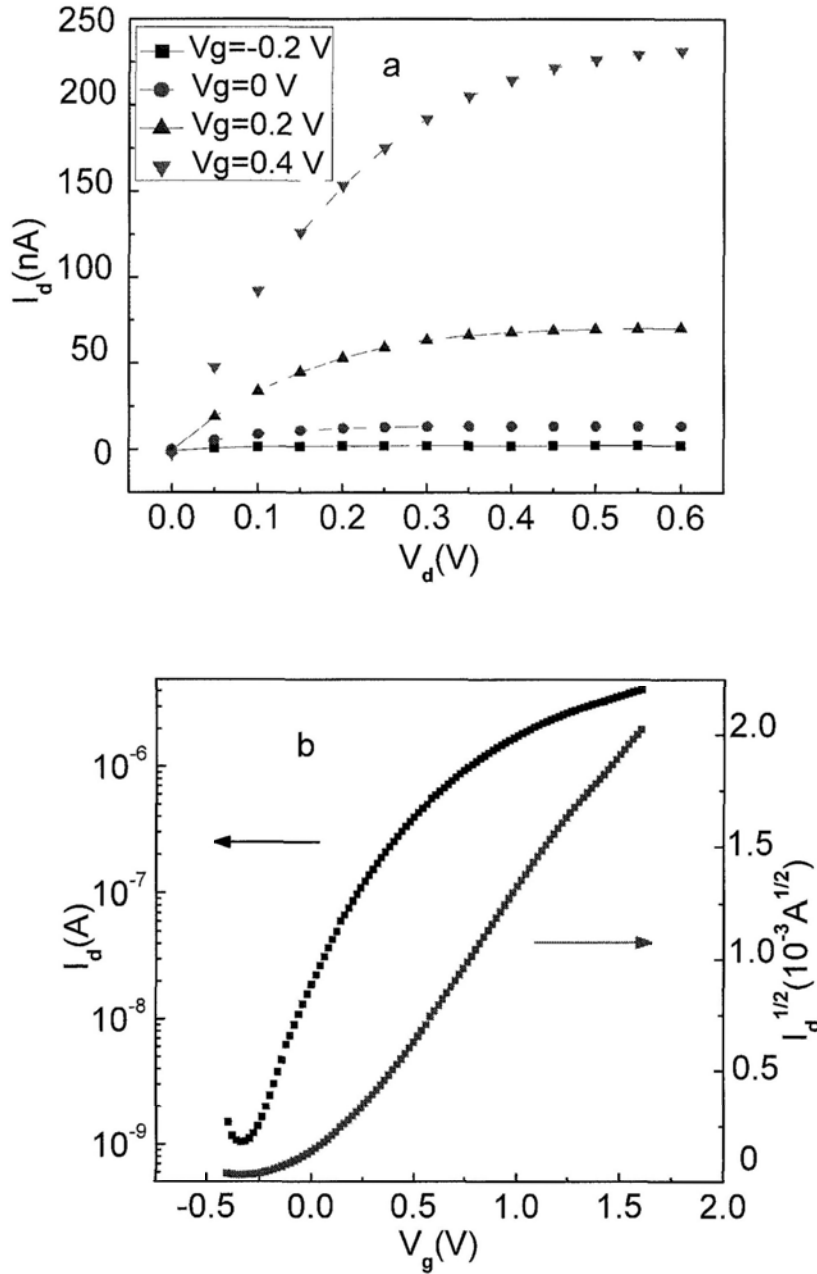
Fig.6-3-4 Output (a) and transfer (b) characteristics of ZnGaLiO thin film transistor.

Both output curves show clear classical n-channel field effect transistor behavior. A well-defined linear region and saturation region can be found. The devices work in accumulation mode. As the drain-source bias increases, the conducting path starts pinched-off, featured by the saturation of current. It is worth pointing out that the area of the drain/source contacts is slightly smaller than that in the leakage current measurement. Therefore, the drain-source current is at least two or three orders of magnitude larger than the leakage current, which unambiguously verifies the nature of

current modulation by the small applied gate bias.

A depth profile by XPS is collected for ZnGaO TFT device. The respective element distribution can be visualized in Fig.6-3-5.
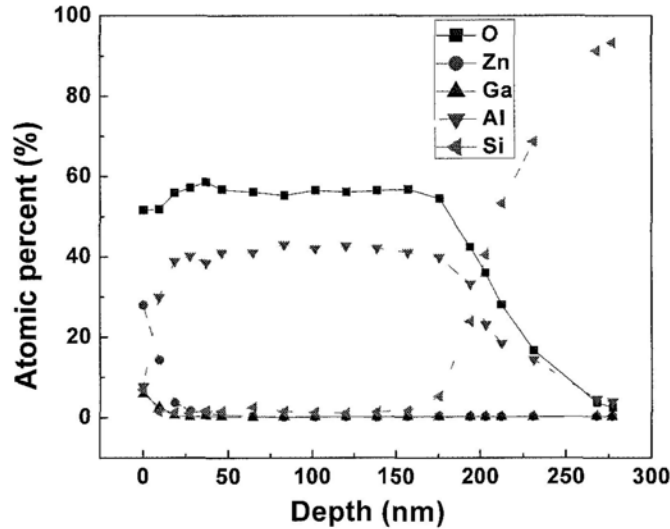
Fig.6-3-5 Element distribution along the vertical direction of ZnGaO TFT.

It can be roughly estimated that the thickness of the active ZnGaO layer and alumina gate dielectric is close to 25 nm and 150 nm, respectively. This estimation is in good agreement with that obtained by SEM cross section view.

For comparison, we fabricate the pure ZnO thin film transistor. The precursor concentration is still 0.1 M, and the annealing conditions are completely kept unchanged. The output and transfer characteristics are shown in Fig.6-3-6.

For convenience, we rewrite the current versus gate bias equation of the classical MOSFET, as mentioned in Chapter 5:

$$I_d = \frac{W}{2L} \mu C_i (V_g - V_{th})^2$$

$$(6\text{-}1)$$

The capacitance of the spin-coated alumina in this group of TFT devices is 57 nF·cm^{-2}. Following the similar way to that in Chapter 5, we can calculate the field effect mobility, threshold voltage and current on-off ratio for the above three devices, respectively, which are summarized in Table 6-3-1.

Table 6-3-1 Field effect properties of doped and un-doped ZnO thin films with spin-coated alumina as the gate dielectric.

	μ, mobility $(cm^2V^{-1}s^{-1})$	V_{th}, threshold voltage (V)	On-off ratio
Un-doped ZnO TFT	1.1	−0.4	0.6×10^3
ZnGaLiO TFT	2.1	0.06	4×10^3
ZnGaO TFT	4.7	0.2	5×10^3
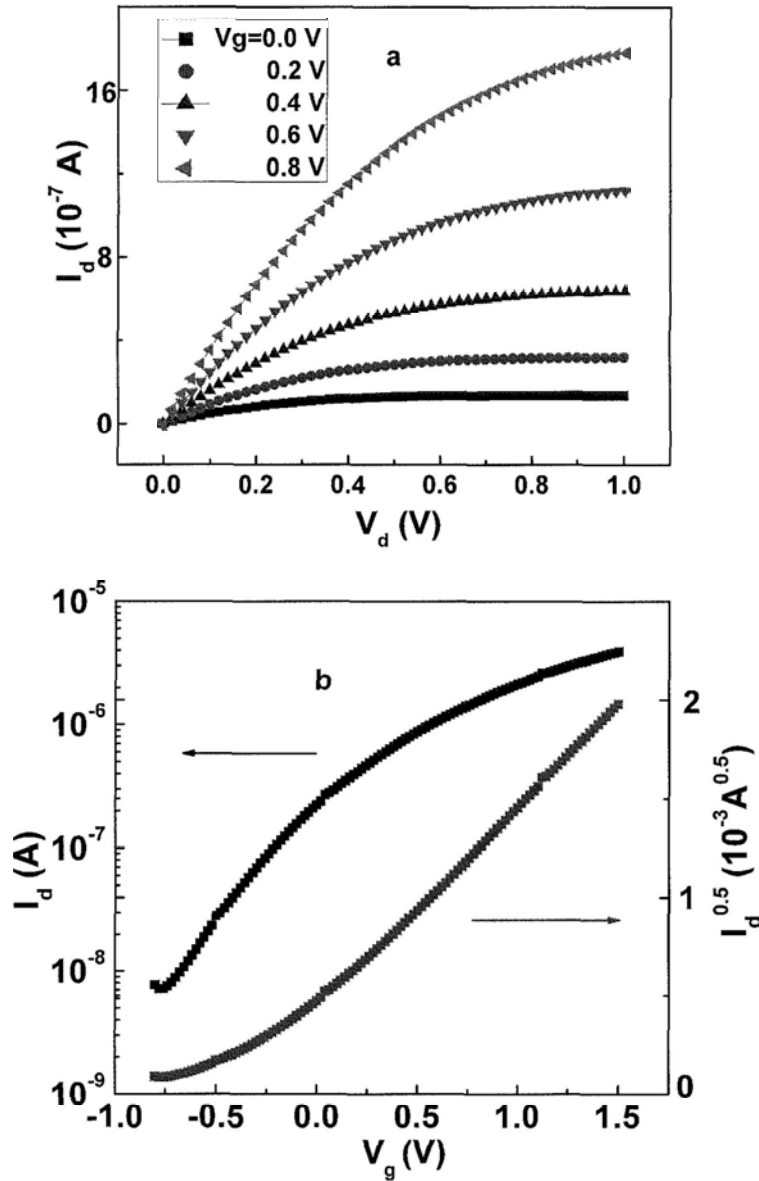
Fig.6-3-6 Output (a) and transfer (b) characteristics of ZnO thin film transistor.

It can be seen that the mobility for Ga-doped ZnO TFT is the largest, while Ga and Li co-doped counterpart shows smaller mobility. The reason might be additional acceptor defects introduced by doping of Li, which reduces the effective carrier concentration. Un-doped ZnO TFT shows poor field effect performance in terms of smallest mobility and on-off ratio, which can be attributed to small electron concentration.

As mentioned in Chapter 5, a larger mobility might be obtained if the doping ratio between Ga and Li is increased. Here, another ZnGaLiO based TFT is fabricated,

where the ratio of metal element is Zn: Ga: Li= 90: 4: 6. Other fabrication conditions are exactly following those of the above devices.

Fig.6-3-7 shows the output and transfer plots.
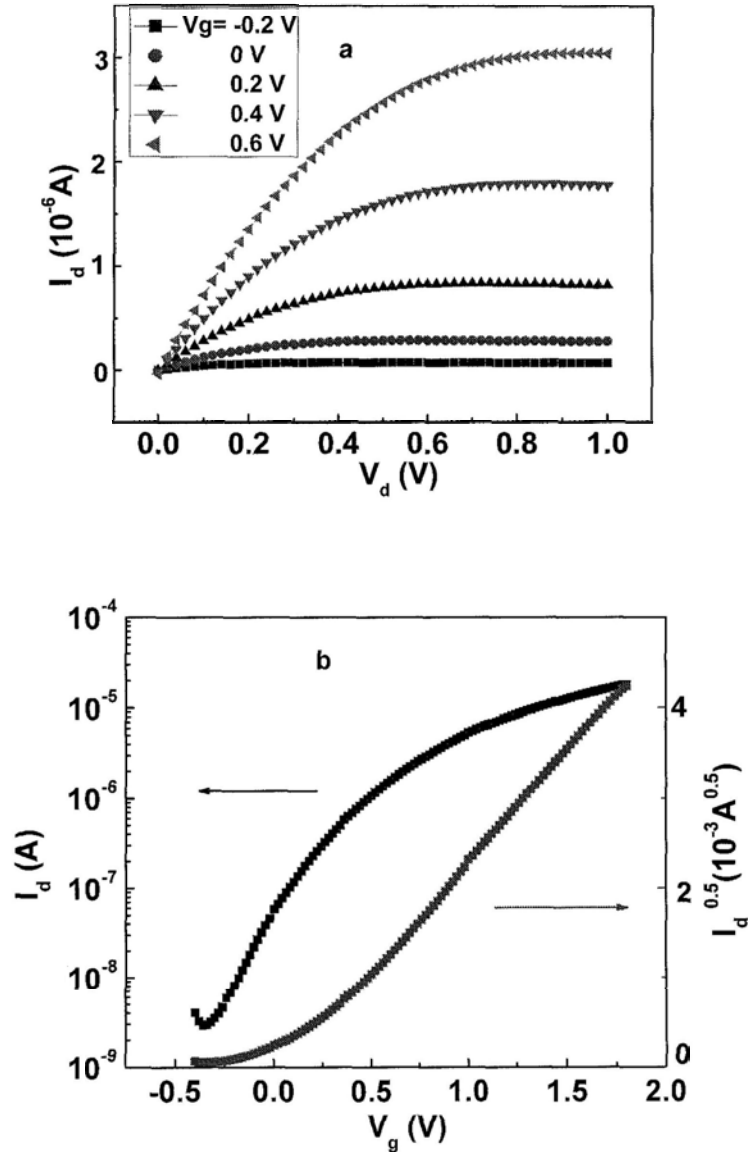
Fig.6-3-7 Output (a) and transfer (b) plots of ZnGaLiO TFT (Ga: Li= 4: 6).

Classical current saturation behavior at higher drain source voltage can be seen, and is a clear sign of the pinch-off phenomenon. The calculated field effect mobility, threshold voltage and current on-off ratio are 7.5 cm^2 V^{-1}s^{-1}, 0.15 V and 6.5×10^3. Therefore, increasing the ratio of Ga to Li can effectively increase the device performance.

6.4 Amorphous metal oxide semiconductor (AMOS) based thin film transistors

6.4.1 Introduction

Up until now, all of our devices require high temperature annealing (600 °C) before we can obtain high performance transistors. In fact, similar to our results, the recent development of oxide transparent TFTs represent a marked advance in the emerging field of transparent electronics. So far, most of this type of transistors comprise an active layer of crystalline oxide [13-15] that are typically produced at relatively high processing temperatures (400-700 °C) [16], which is inappropriate for large area production on flexible substrates. Amorphous metal oxide semiconductors (AMOSs) provide an alternative solution to the challenge, because low-temperature process, large band gap of the material, broad transparency windows, and mechanical stress tolerance are highly anticipated [17]. AMOSs are usually composed of heavy-metal cations with $(n-1)d^{10} ns^0$ ($n \geq 4$) electronic configurations and have large s orbital radii, leading to a high degree of overlap between adjacent orbitals and considerable band dispersion. Therefore, they can exhibit large mobilities comparable to those of their crystalline counterparts [16,18].

Various amorphous oxide semiconductor thin films such as In_2O_3, ZnO, In-Sn-O, Zn-Sn-O, In-Zn-O, In-Ga-Zn-O, etc., have been fabricated, predominantly using vacuum deposition techniques, such as pulsed laser deposition [19-21], and magnetron sputtering [22, 16,23]. High cost and low throughput issues overshadowed the merits of the techniques. In contrast, solution deposition of semiconductors offers many advantages such as fabrication simplicity, low cost, high throughput and the ease of controlling chemical stoichiometry. However, the previously reported solution processed amorphous TFTs still often needed annealing at high temperatures (usually ≥ 400°C) to achieve the best performance [24,25], incompatible with flexible substrates. Low operation voltage is another prerequisite in order to reduce the power consumption. Recently, encouraging results have been reported by H. S. Kim *et al.* [17] and H. Bong *et al.* [26], who reduced the annealing temperature to 250 °C and 300 °C, respectively, without significantly degrading the device performance.

However, the fabrication of the organic dielectric used is rather complicated, inherently difficult to be uniform with the subsequently fabricated inorganic semiconductor film, which may suffer from the integration difficulty, and the device stability due to high temperature annealing or oxidization. In this section, we report on solution-processed active layer of amorphous indium tin oxide (ITO) or InGaZnO TFTs, having a high mobility, low annealing temperature, and operation voltage. Spin-coated alumina is still prepared in the same way as the gate dielectric.

6.4.2 Indium tin oxide (ITO) based TFTs

Indium tin oxide precursor is prepared in the following way. 0.1 M (total metal concentration) indium tin oxide precursor is prepared by dissolving indium nitrate (99.9 %) and tin acetate (99.9 %) in 2-methoxyethanol, followed by stirring for 30 minutes at room temperature. The metal ratio is In: Sn = 7: 3. Monoethanolamine (MEA, 99.5 %) as a stabilizer is added to the solution with a ratio of 2: 1 to the total metal concentration. The channel layer is formed by spin-coating of ITO precursor onto n^{++} Si with the same conditions as previous devices. Three such prepared thin films are annealed at 220 °C, 240 °C and 260 °C respectively. Aluminum source and drain contacts are thermally evaporated as aforementioned. The temperature error has been calibrated to be about 10 ~ 20 °C.

Typical surface of ITO thin film annealed at 220 °C is observed by atomic force microscopy as shown in Fig.6-4-1.
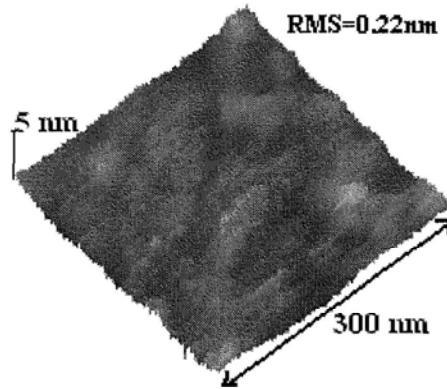
Fig.6-4-1 AFM image of ITO thin film annealed at 220 °C.

The spin-coated alumina thin film has a very smooth surface, and the rms roughness is 0.22 nm, close to that of the alumina dielectric surface. This implies that the upper semiconducting layer images the surface of the underlying dielectric. The smooth interface is very beneficial to reduce the interface scattering.

The output and transfer curves of the three devices are shown in Fig.6-4-2.
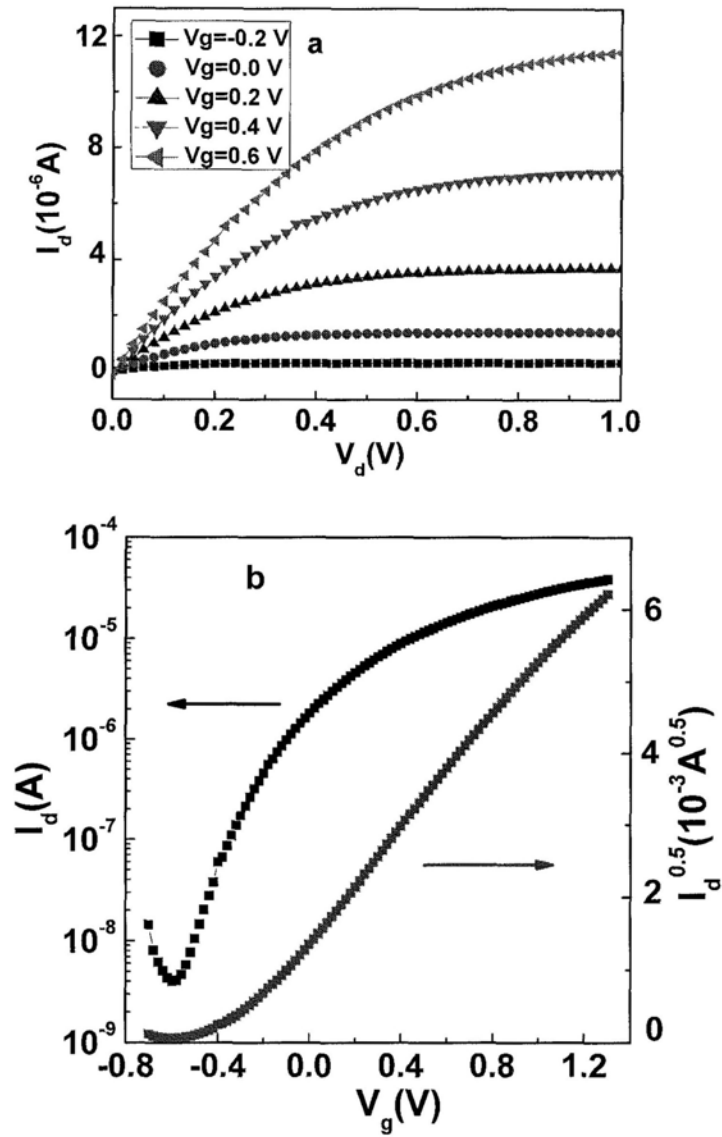
Fig.6-4-2 Output (a) and transfer (b) characteristics of ITO TFT annealed at 220 °C.

To verify the amorphous nature of the ITO thin film, XRD characterization is performed. The pattern is shown in Fig.6-4-3.

143
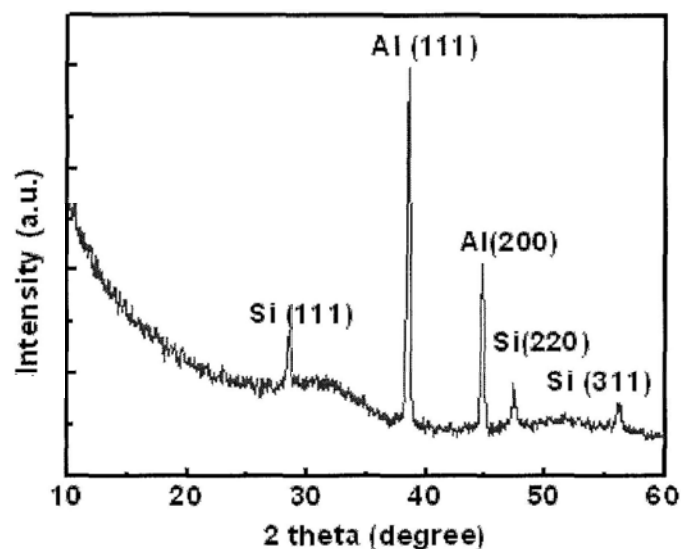
Fig.6-4-3 XRD pattern of ITO thin film annealed at 220 °C, followed by Al evaporation.

A broad peak profile at close to $2\theta= 30°$ is observed, corresponding to the (222) plane of indium oxide in its crystalline form, as compared to the standard ITO pattern (PDF # 894598).
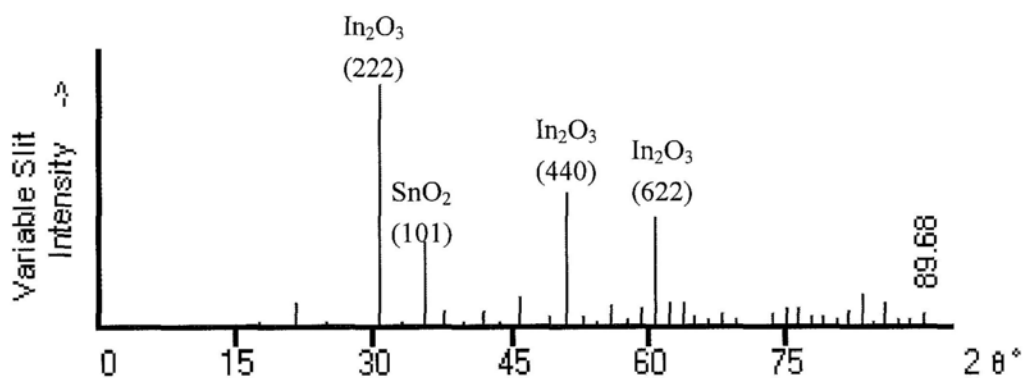
Fig.6-4- 4 Standard XRD pattern of ITO thin film.

The amorphous nature suggested by XRD pattern agreed with the surface morphology of the thin film. Similar AFM image and XRD pattern for the ITO thin films annealed at 240 °C and 260 °C are observed.
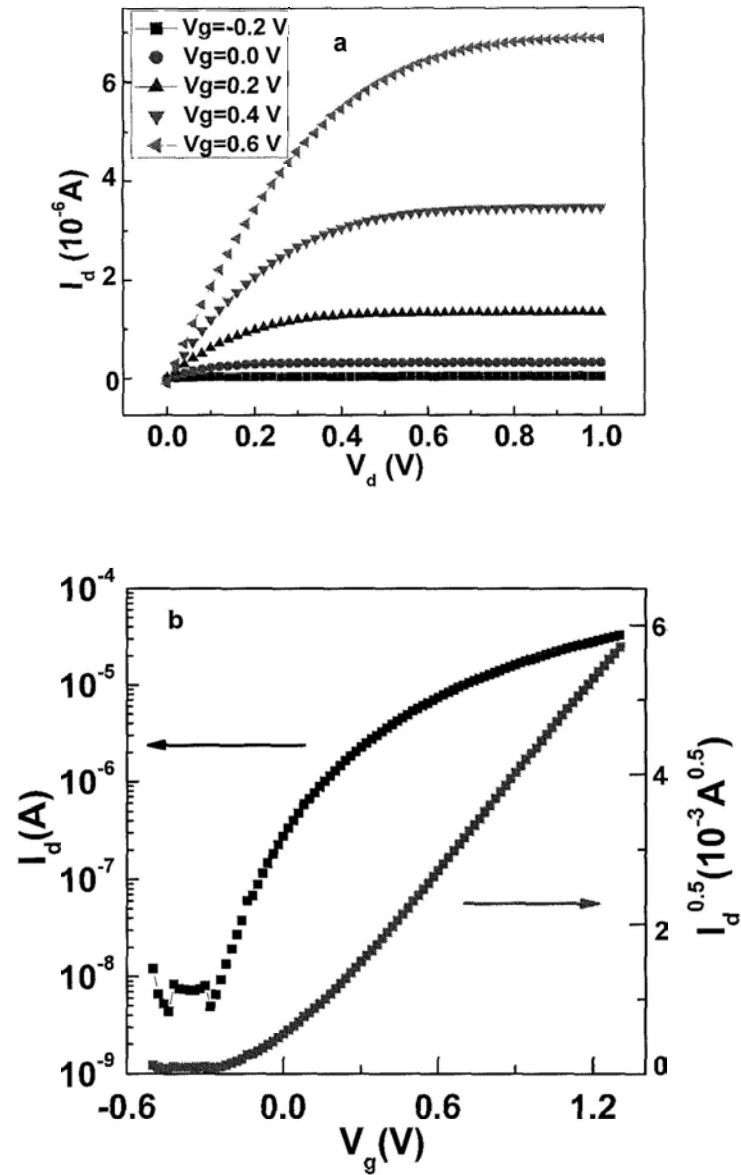
Fig.6-4-5 Output (a) and transfer (b) characteristics of ITO TFT annealed at 240 °C
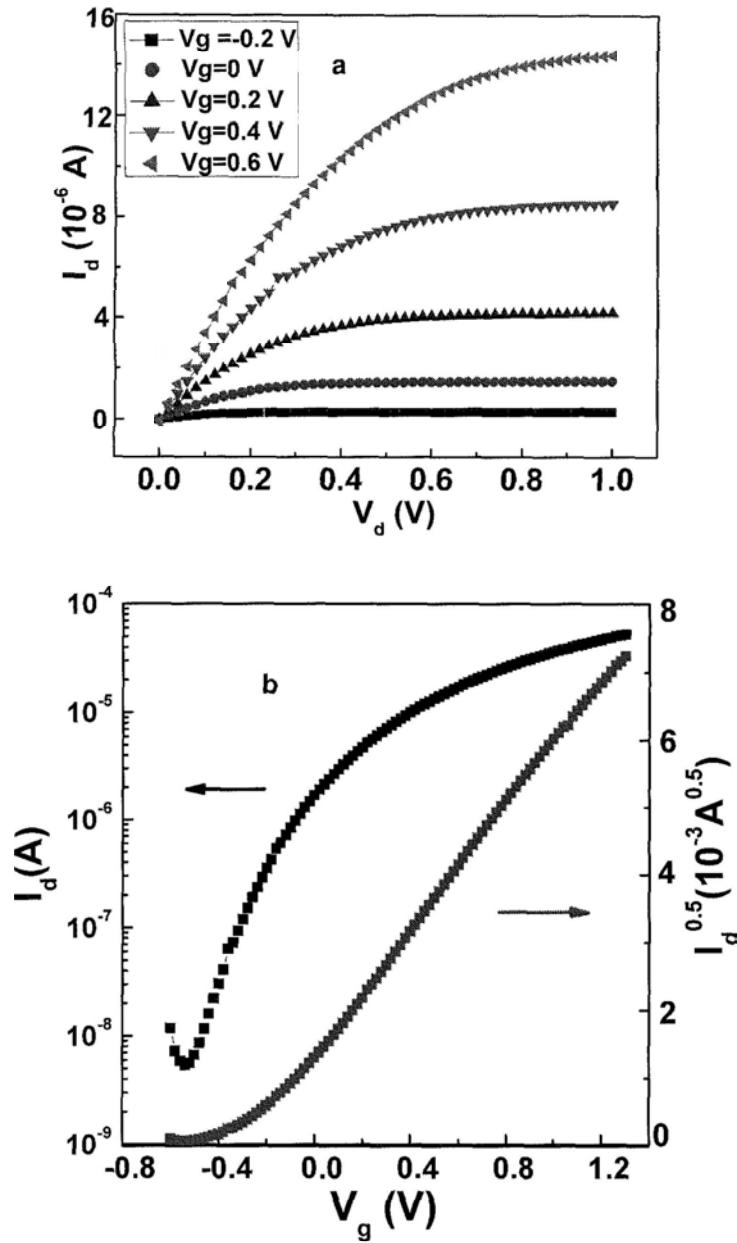
Fig.6-4-6 Output (a) and transfer (b) characteristics of ITO TFT annealed at 260 °C.

Following the identical way, saturation field effect mobility, current on-off ratio and threshold voltage are calculated, as summarized in Table 6-4-1. The unit area capacitance in this section is 170 nF·cm^{-2}.

Table 6-4-1 Field effect properties of ITO thin films annealed at different temperatures.

Annealing temperature (°C)	μ, mobility ($cm^2V^{-1}s^{-1}$)	V_{th}, threshold voltage (V)	On-off ratio	S, subthreshold Swing(V/decade)
220	5.5	-0.32	~10^4	0.20
240	6.3	-0.05	~10^4	0.13
260	8.5	-0.23	~10^4	0.16

The field effect mobility increases slightly as the annealing temperature increases. At 220 °C, the mobility is still quite large, compared with other devices experiencing high temperature annealing [13,15]. The current on-off ratio is close to 10^4.

6.4.3 InGaZnO TFTs with spin-coated alumina as the gate dielectric

Amorphous InGaZnO thin film is another widely studied semiconductor for oxide-based TFT devices, either prepared by pulsed laser deposition or magnetron sputtering [21,23]. To date, there is no report about the field effect properties of solution-processed amorphous InGaZnO thin films with spin-coated alumina as the gate dielectric, which is expected to show large field effect mobility according to the previous studies. In this section, spin-coated amorphous InGaZnO thin film on spin-coated alumina dielectric is fabricated.

InGaZnO precursor is prepared in the following way. 0.1 M (total metal concentration) indium gallium zinc oxide precursor is prepared by dissolving indium nitrate (99.9 %), gallium nitrate hydrate (99.9 %) and zinc acetate (99.99 %) in 2-methoxyethanol, followed by stirring for two hours at 52 °C. The metal ratio is In: Ga: Zn=65: 10: 25. Monoethanolamine (MEA, 99.5 %) as a stabilizer is added to the solution with a ratio of 2: 1 to the total metal concentration. The active semiconducting channel layer is prepared with the same spin-coating conditions. Two InGaZnO thin films annealed at 225°C and 260°C are employed as the semiconducting channel layers, respectively. Aluminum source and drain contacts are

evaporated through shadow masks. The temperatures are calibrated to be 225 ~ 245 °C and 260 ~ 280 °C, respectively.

The surface morphology of InGaZnO thin film annealed at 225 °C is observed by AFM, with the result shown in Fig.6-4-7.
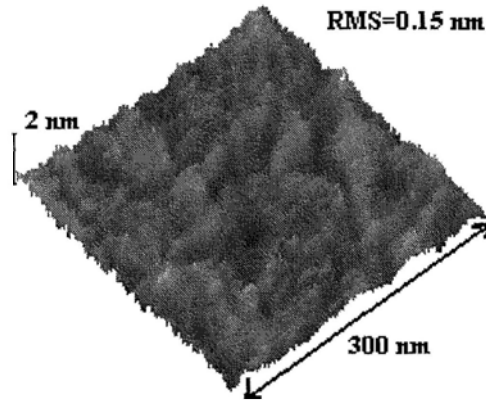
Fig.6-4-7 AFM image of InGaZnO thin film annealed at 225 °C

Similar to the spin-coated alumina, the InGaZnO thin film has a very smooth surface, and the rms roughness is 0.15 nm, close to that of the alumina dielectric surface. This implies that the upper semiconducting layer replicates the surface of the underlying dielectric. The smooth interface is very beneficial to reduce the interface scattering. The AFM image for the other one annealed at 260 °C is similar.

The output and transfer characteristics of InGaZnO TFT annealed at 225°C are shown in Fig.6-4-8.
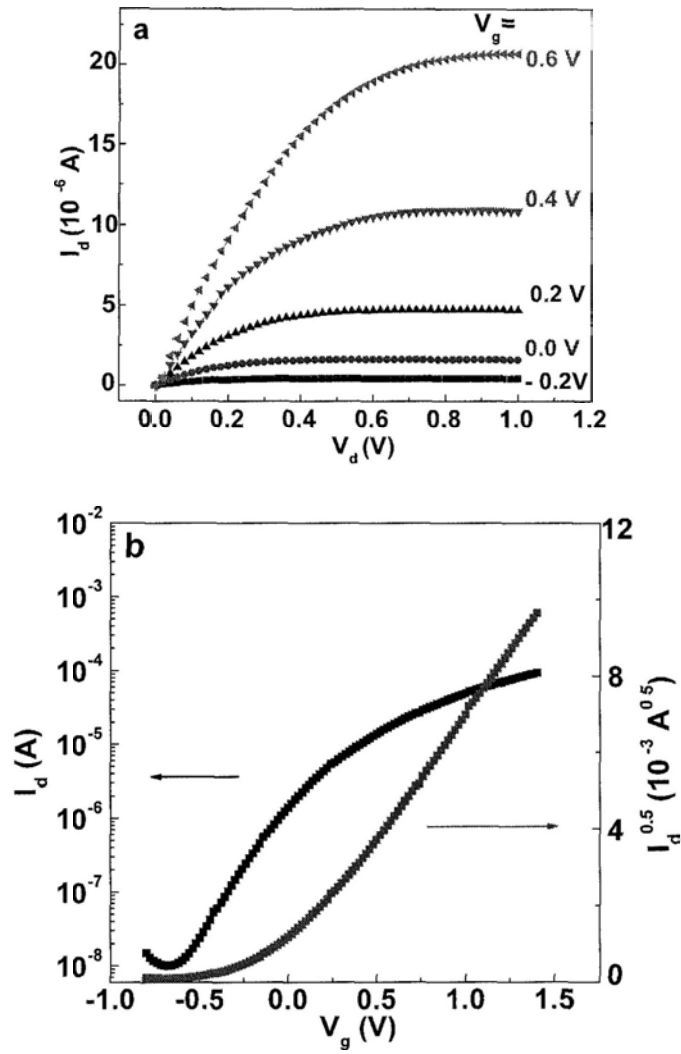
Fig.6-4-8 Output (a) and transfer (b) plots of InGaZnO TFT annealed at 225 °C

The amorphous nature of InGaZnO thin film annealed at 225 °C is examined by x-ray diffraction, as shown in Fig.6-4-9.
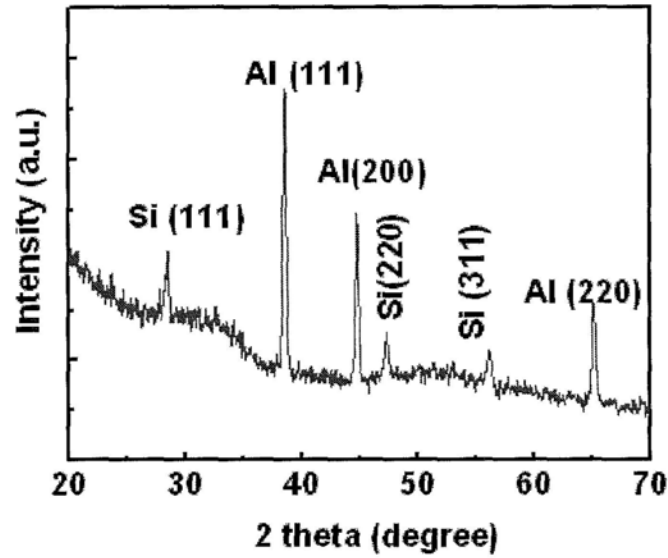
Fig.6-4-9 XRD pattern of amorphous InGaZnO thin film annealed at 225 °C.

Similarly, compared with the standard XRD pattern of indium oxide (Fig.6-4-4), the peak profile at close to 30° is attributed to the (222) In_2O_3 crystal plane. This agrees with the previously reported results in the reference [17]. Similar XRD pattern for InGaZnO thin film annealed at 260 °C is observed.

The output and transfer characteristics are demonstrated in Fig. 6-4-10.
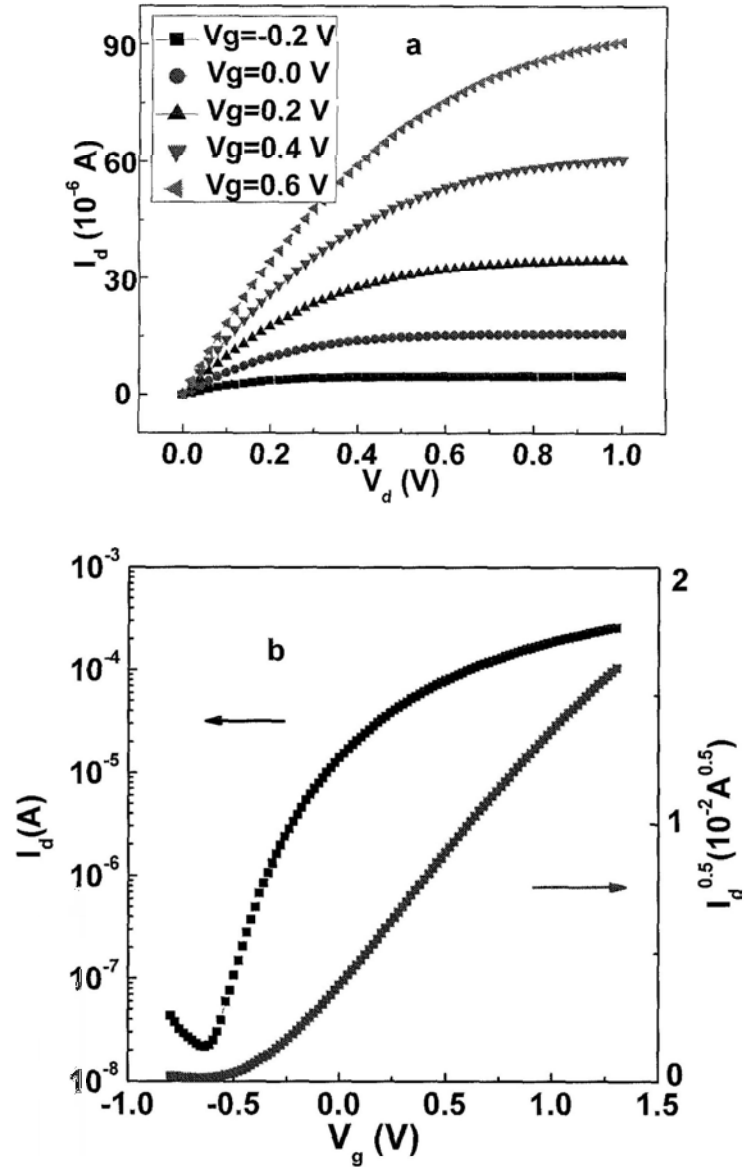
Fig.6-4-10 Output (a) and transfer (b) characteristics of InGaZnO thin film annealed at 260 °C.

The saturation field effect mobility, threshold voltage, current on-off ratio and subthreshold swing are summarized in Table 6-4-2:

Table 6-4-2 Field effect properties of InGaZnO thin films annealed at different temperatures.

	Annealing temperature (°C)	μ, mobility ($cm^2\ V^{-1}s^{-1}$)	V_{th}, threshold voltage (V)	On-off ratio	S, subthreshold swing (V/ decade)
InGaZnO	225	18.3	-0.05	~10^4	0.16
TFT	260	30	-0.35	~10^4	0.15

Exceptionally large motilities of 18.3 and 30 $cm^2\ V^{-1}s^{-1}$ are obtained, which are larger than most other devices fabricated by solution processing method [13, 15, 19]. They are even comparable with those oxide-based TFTs obtained by vacuum based techniques [11].

It is noted that the subthreshold swing of both ITO and InGaZnO TFTs is close to 0.2 V decade^{-1}, and can be used to estimate the maximum density of surface states by the following equation [28]:

$$N_{max}^{SS} = \left[\frac{S\log(e)}{(kT/q)} - 1 \right] \frac{C_i}{q}$$

(6-2)

where k, T, q and e are Boltzmann's constant, temperature, elemental charge of electrons and the base of natural logarithm, respectively. The inferred maximum density of surface states is 2.47×10^{12} cm^{-2} for the AMOS/alumina interface, after taking into account of C_i and S. This value is about one order of magnitude smaller than that found in previous TFTs on ATO insulator [27] and others [12].

It is noted that in the capacitance-frequency spectroscopy, the capacitance changes dramatically at low frequency, which has been attributed to the presence of mobile ions (usually protons) in the reference [11]. It is widely known that clockwise hysteresis is often caused by a large amount of defect states at the channel/gate dielectric interface, whereas a counter-clockwise hysteresis is presumably attributed to mobile ions (protons) [11]. Here, the density of protons may be evaluated, by taking the InGaZnO thin film annealed at 260 °C as an example. The dual sweeping of transfer curve of InGaZnO thin film annealed at 260 °C is shown in Fig.6-4-11.
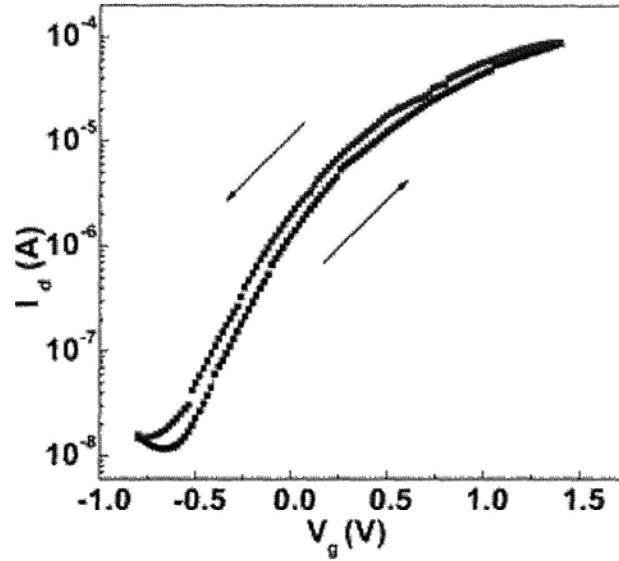
Fig.6-4-11 Transfer hysteresis of InGaZnO TFT. The active layer is annealed at 225 °C.

The density of protons is roughly estimated to be 1×10^{11} cm^{-2} based on the following equation [28]:

$$N = \frac{\Delta V_{th} \times C_i}{q}$$

(6-3)

where ΔV_{th}, C_i and q are the threshold voltage shift (~ 0.1 V), unit area capacitance of spin-coated alumina (170 nF·cm^{-2} at 20 Hz) and the elemental electron charge (1.6 $\times 10^{-19}$ C), respectively. With a positive gate bias applied, protons are moved to the thin boundary layer at the channel/alumina dielectric interface and induce image charges in the semiconducting channel layer. When the gate voltage decreases, since the slow motion of the protons, the electron concentration does not follow the decrease of gate voltage immediately. Therefore, the measured immediate current is larger than that in the forward scan, which exactly explains the counterclockwise behavior. The schematic is shown in Fig.6-4-12. This operation mechanism agrees very well with the previously proposed electric double layer model (EDL) [11].These protons are possibly created during the high temperature baking process to evaporate the organic residuals.

153
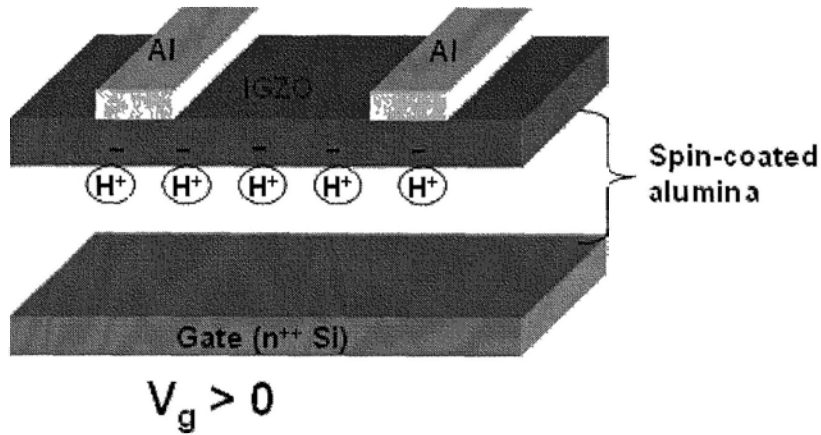
Fig.6-4-12 Schematic model of protons in the alumina dielectric.

According to the proposed model, it can be inferred that as the scan rate increases, a more pronounced counterclockwise behavior can be observed, which is exactly what we found. As shown in Fig.6-4-13, the "fast" mode means the holding time for each point is 0.01s, while in the "normal" mode, the holding time is 0.1s. We can find that the transfer hysteresis loop (in counterclockwise direction) in the fast mode is obviously larger than that in the normal mode. The faster the scanning rate, the larger hysteresis effect is caused by the slow motion of protons.
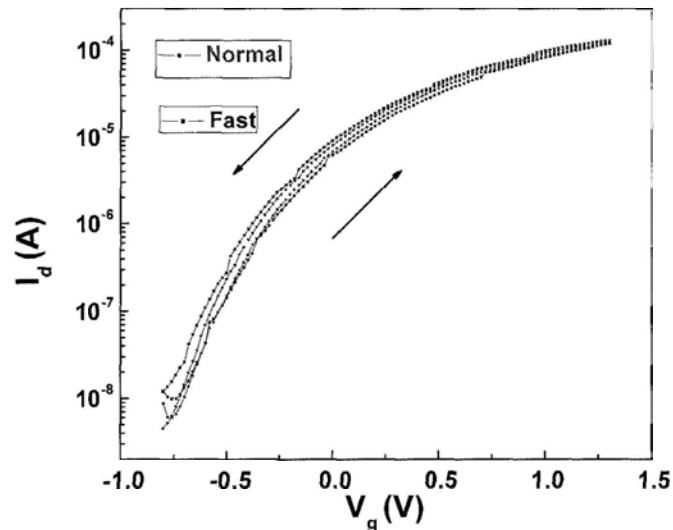
Fig.6-4-13 Transfer plots of IGZO TFT with different scanning rate.

To be more specific, we set the source drain voltage as a constant (1 V), measure the drain current (I_0) without gate bias, then we apply a pulse gate voltage (1 V) with

different pulse durations, and we measure the drain current (I_t) once the gate voltage has been withdrawn. The current change against different gate pulse duration is shown in Fig.6-4-14. It can be found that as the pulse length increases, the measured current increases accordingly. The reason is that a longer gate pulse can move more protons to the channel/alumina dielectric interface. Once the gate voltage has been removed, these protons linger near the interface. Therefore more electrons are imaged in the channel, resulting in a larger drain-source current. These observations have been repeated in other devices gated by spin-coated alumina, and can be well explained by the presence of protons in the dielectric. Unfortunately, by normal composition analysis (EDX, XPS, ICP-MS, etc), it is very difficult to detect protons because of the small mass.
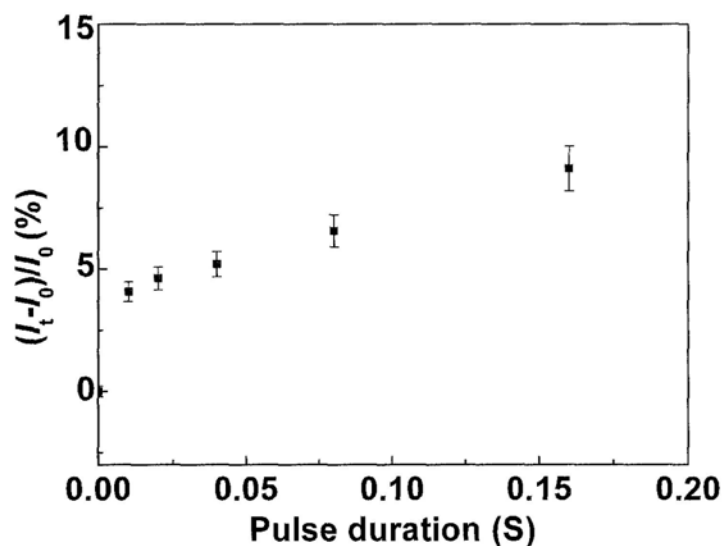
Fig.6-4-14 Drain current change after applying the gate bias for different pulse durations.

Meanwhile, the amorphous nature of metal oxide thin films accounts for the excellent field effect performance as well. As the annealing temperature decreases, the completion of atomic rearrangement and lattice formation deteriorates, however, in AMOSs, its effect on electronic performance may not be dominant because the conduction is via the spatial expanse of s-states. Provided that the expanse is greater than the interaction distance, the spherical symmetry of s orbital and hence high degree of orbital overlapping render the delocalized electronic transport less sensitive

to the degree of lattice formation or the long-range order [18]. A relatively high baking temperature as in the present study may be necessary to ensure sufficient spatial expanse of s-states.

6.5 Discussion

In the previous work, we have fabricated different thin film transistors with doped or un-doped ZnO as channels and with thermally grown SiO_2 or spin-coated alumina as the gate dielectrics. The semiconductor channels are either polycrystalline or amorphous. In this section, we will make some comparisons to discuss in more detail about some factors, which are playing significant roles in the field effect performances of devices.

6.5.1 Interface roughness

We have fabricated polycrystalline and amorphous semiconductor thin films as the channels. Usually, the polycrystalline ZnO thin film has a much larger interface roughness (rms = 4 ~ 6 nm), and the field effect performance is very poor without annealing at high temperature (400 ~ 700 °C); while the amorphous semiconductor thin film has a very smooth interface (RMS = ~ 0.15 nm), and the field effect mobility is much larger even by simple baking below 300 °C. This can be understood from the schematic Fig.6-5-1.
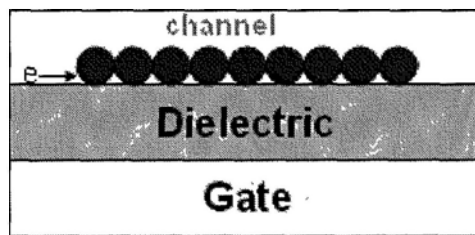
Fig.6-5-1 Interface roughness influence on the electron transport in the channel.

For simplicity, in the polycrystalline semiconductor, the channel near the dielectric can be simplified as round grains arranged in order. A rough interface means a larger grain size. We can find that as the grain size becomes larger, the gap between grains becomes larger as well. Therefore, the electrons in the channel experience much larger scattering by the grain boundary. It has been reported that even when the film roughness reduction is 1.7 nm, the field effect mobility of ZnO thin film can be

increased by about one order [29]. In the case of amorphous semiconductor, this kind of scattering by grain boundary can be minimized. This is one of the reasons we can have larger mobility in InGaZnO TFTs.

6.5.2 Interface carrier traps

The most widely accepted charge transport in semiconductor TFTs involve multiple trapping and release model (MTR). This model postulates that the free carrier mobility is diminished by recurrent charge trapping and thermal release from shallow trap states below the conduction band edge [30]. At room temperature, this carrier trap density can be estimated by the following equation [30]:

$$N = \frac{0.43S \bullet C_i}{kT}$$

$$(6-4)$$

where N is the carrier trap density at room temperature, T is the temperature (300 K), k is Boltzman's constant, C_i is the unit area capacitance of the dielectric and S is the subthreshold voltage, as defined in the preceding chapter. Therefore, the product of S and C_i determines the carrier trap density at the same temperature. We can compare the ZnO TFTs gated by SiO_2 and spin-coated alumina. C_i for SiO_2 and spin-coated alumina is about 10 $nF{\cdot}cm^{-2}$ (Fig.5-2-3) and 57 $nF{\cdot}cm^{-2}$ (Fig.6-3-6), respectively. The calculated S for SiO_2 and alumina gated devices is 15 V/decade and 0.15 V/ decade. Therefore, we can find that the carrier trap density in spin-coated alumina gated devices is at least one order of magnitude smaller than that in SiO_2 gated devices. It should be noted that Equation (6-3) depicts the mobile charge concentration (net) in a counterclockwise hysteresis [11] with different measurement process from Equation (6-4); whilst Equation (6-2) is used to calculate the maximum density of surface states, which is not necessarily equal to, but often very close to the trap density [28], calculated by (6-4).

The large carrier trap density in SiO_2 has been reported previously by various groups, and this large number of trap density can result in the degradation of field

effect mobility by several orders of magnitudes [17,26]. These traps are either from the dangling bonds or adsorbed H_2O molecules on the surface of SiO_2. The typical evidence showing the presence of carrier traps on the surface of SiO_2 is the clockwise transfer hysteresis. We examine various SiO_2 gated ZnO TFTs, either doped or un-doped, either polycrystalline or amorphous ZnO as the channels. All of them show very clear clockwise transfer hysteresis. Fig.6-5-2 is a typical result observed from the Li-doped ZnO TFT gated by SiO_2.
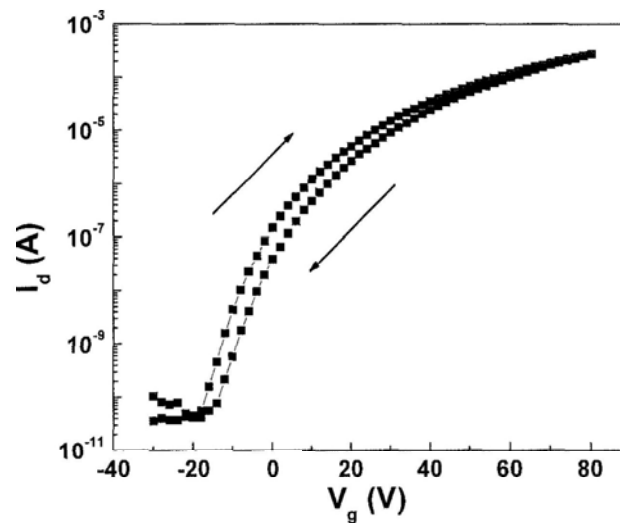
Fig.6-5-2 Transfer hysteresis of Li-doped ZnO TFT gated by SiO_2.

For a better comparison, we show the counterclockwise transfer plot of spin-coated alumina gated device again. The mechanism of this counterclockwise hysteresis has been discussed in detail in Section 6.4, which has been mainly ascribed to the presence of positive mobile ions (protons).
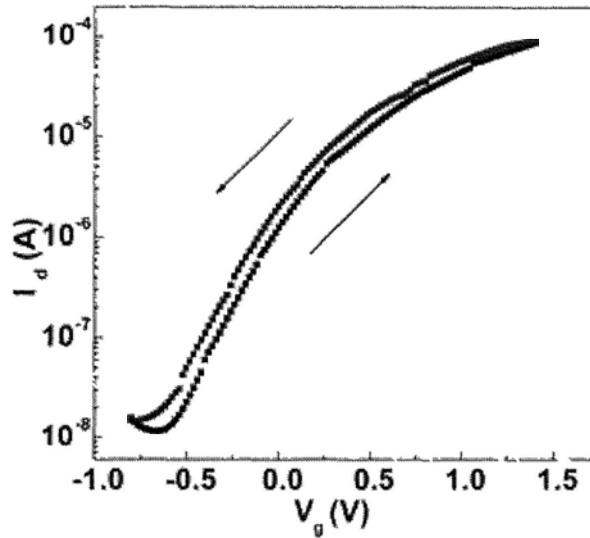
Fig.6-5-3 Transfer hysteresis of InGaZnO TFT gated by spin-coated alumina.

The reason of clockwise transfer hysteresis by the carrier traps in the surface of SiO$_2$ can be schematically explained in the following way.
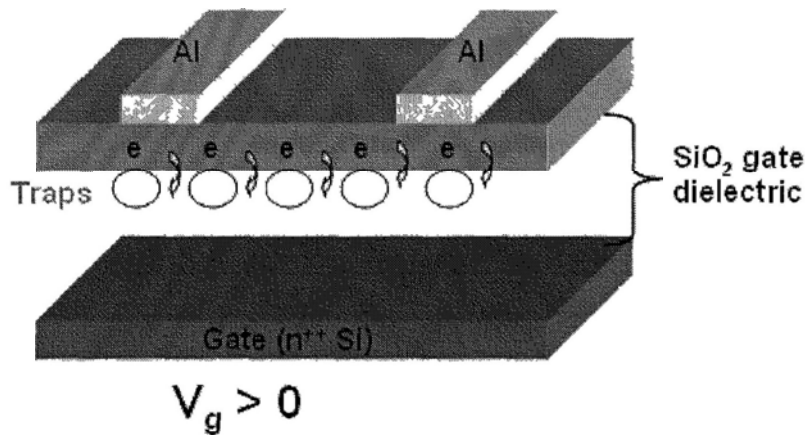
Fig.6-5-4 Schematic showing the trap states near the surface of SiO$_2$ dielectric.

As the gate voltage increases, electrons are attracted to the channel near the interface. The electron traps on the surface of SiO$_2$ gate dielectric are filled in by these attracted electrons. The filled traps are negatively charged, therefore, electrons in the channels are repelled by these traps as well as attracted by the gate bias. As the gate voltage decreases (backward scan), the trapped electrons cannot be activated immediately, and the electrons in the channel are repelled away. Therefore, at the same gate voltage, the current is smaller in the backward scan than the forward scan,

leading to the observed clockwise hysteresis, which is contrary to the protons in the spin-coated alumina gated devices. This kind of clockwise hysteresis in SiO_2 gated TFTs has often been reported previously [31-32].

In essence, in SiO_2 gated devices, the presence of large amount of electron traps significantly reduces the mobility, while in spin-coated alumina gated devices, the density of electron traps is smaller, and its role has been overtaken by the presence of some positive mobile ions (protons). So, larger field effect mobility can be obtained by use of spin-coated alumina as the gate dielectric.

6.5.3 Threshold voltage shift

All of our fabricated devices are in a bottom-gate top-contact (BG-TC) structure. The back channel is bare and can easily adsorb oxygen or water in air. This may result in the threshold voltage shift of the device.

Fig.6-5-5 shows the transfer plots of the same InGaZnO TFT measured initially after the fabrication and 5 months after the fabrication. The device is stored in a dry cabinet. Through calculation, the threshold voltage is - 0.05 V and 0.20 V, respectively. A clear positive threshold voltage has been observed. It is worth noting that this positive threshold voltage shift is a common phenomenon in our devices, whether gated by SiO_2 or spin-coated alumina, whether polycrystalline ZnO semiconductor channel or amorphous InGaZnO channel. In Chapter 5, the positive threshold voltage shift of un-doped ZnO TFT gated by SiO_2 has been shown (Fig.5-3-3, Table 5-3-2).
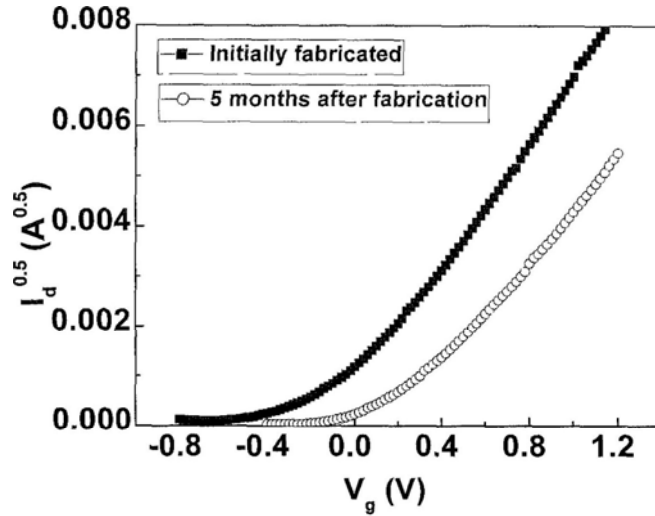
Fig.6-5-5 Transfer plots (square root) of the same InCaZnO TFT measured at different times.

It is well known that O_2 can be easily adsorbed onto the back channel area, and these adsorbed O_2 from the ambient atmosphere can capture electrons in the conducting channel and create the negatively charged species O_2^- (s) in the following way [33-34].

$$O_2(g) + e^- \rightarrow O_2^-(s)$$

(6-5)
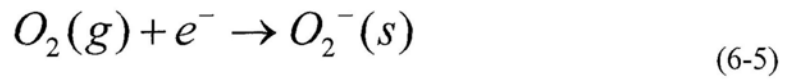
The adsorption can be schematically shown in Fig.6-5-6.
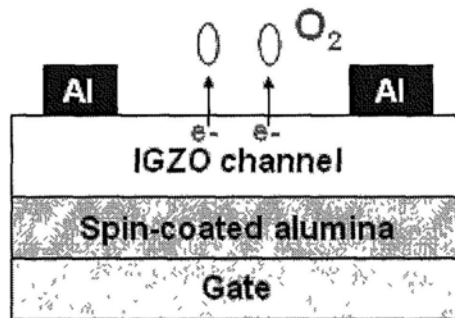
Fig.6-5-6 O_2 adsorption onto the bare back channel of IGZO.

The build-up of negatively charged space may repel the electrons in the amorphous IGZO conduction channel. Therefore a larger gate voltage is needed to turn the device

162

on, which well explains the positive threshold voltage shift. In Chapter 5, it has been shown that doping by Li can help to keep the threshold voltage stable (in Fig.5-3-3) . An alternative way to keep the bottom-gate top-contact device stable is by use of a passivation layer on the bare surface of the back channel. The role of different passivation layers on the stability of threshold voltage has been discussed in detail elsewhere [35-36].

6.5.4 Temperature dependence of mobility

The multiple trapping and release (MTR) model is widely accepted to describe the charge transport in thin film transistors. The free carrier mobility is diminished by charge carrier trapping and thermal release from the trap states below the conduction band edge, which defines the effective field effect mobility as what we measured [30]. The thermal release from the shallow trap states is a function of temperature; therefore, usually the field effect mobility depends on the temperature in the following way [30]:

$$\mu_{eff} = \mu_0 \exp(\frac{-E_a}{kT})$$

(6-6)

where μ_{eff} and μ_0 are the measured mobility and free electron mobility, respectively. E_a is the activation energy, k is Boltzman's constant and T is temperature in K. Therefore, the activation energy can be extracted from the linear relation between $\ln(\mu_{eff})$ and $1/T$.

We measured the field effect mobility dependence on temperature of polycrystalline Ga & Li co-doped ZnO (ZnGaLiO) and amorphous InGaZnO thin film transistors. The result is fitted as shown in Fig.6-5-7.
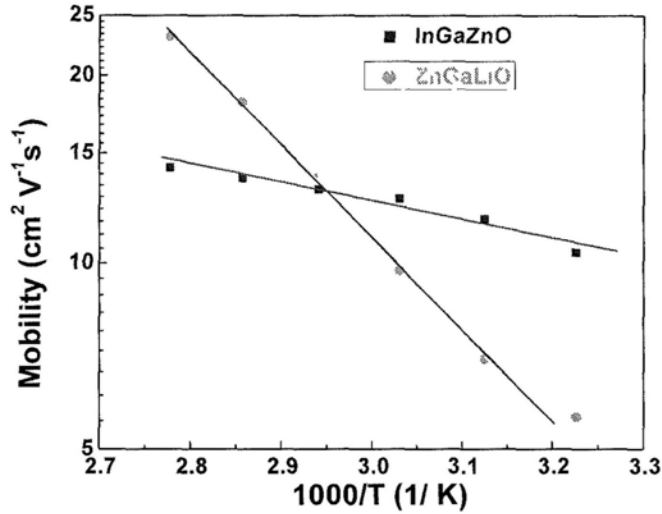
Fig.6-5-7 Temperature dependence of field effect mobility from 310 K ~ 360 K.

Based on Equation 6-6, the extracted activation energies for the amorphous InGaZnO thin film and the polycrystalline ZnGaLiO thin film are 50 meV and 300 meV, respectively. As expected, the activation energy for the polycrystalline ZnGaLiO thin film is much larger than that for the amorphous counterpart. This is due to the different conduction mechanism in these two films. In the polycrystalline structure, the electron transport is severely influenced by the grain boundary effect [37], while in the amorphous structure such grain boundary is not present and as aforementioned, the conduction is via the spatial expanse of s-states. As long as the expanse is greater than the interaction distance, the spherical symmetry of s orbital and hence high degree of orbital overlapping render the delocalized electronic transport less sensitive to the degree of lattice formation [18]. Although there is no long-range order in the amorphous structure, in the very short range, the electron transport is similar to that in the single crystalline structure. Without grain boundary scattering effect, the energy barrier is greatly reduced. This can account for the fact that without high temperature annealing, the amorphous semiconductor channel exhibits comparable or even larger field effect mobility than the polycrystalline semiconductor thin film.

6.6 Conclusions

In this chapter, we use spin-coated alumina as the gate dielectric. The leakage current is minute compared to the drain source current. ZnO based TFTs on the spin-coated alumina dielectric works in exceptionally low voltage range. The field effect mobility is larger than most of solution processed thin film transistors.

In order to reduce the annealing temperature, amorphous ITO and InGaZnO thin film transistors annealed at low temperature are fabricated with spin-coated alumina as the gate dielectric. They exhibit large mobilities, especially InGaZnO TFTs, which is found to be 18.3 $cm^2V^{-1}s^{-1}$ at the annealing temperature close to 250 °C. The high performance enables low power consumption, fast transition speed and deposition on heat-sensitive plastic substrates at low temperatures. The factors influencing the field effect performances such as interface roughness, carrier trap density, O_2 adsorption and activation energy has been discussed in detail. Spin-coated alumina provides unique dielectric properties, excellent thermal stability, transparency, high cost-effectiveness and seamless integration with oxide channel layers, which suggests potential wide applications in future transparent electronics based on plastic substrates.

References

[1] R. Rao and F. Irreraa, J. Appl. Phys. 107, 103708 (2010).

[2] Y. Aoki, T. Kunitake, Adv.Mater. 16, No.2 (2004).

[3] A. Bashir, P. H. Wöbkenberg, J. Smith , J. M. Ball, G. Adamopoulos, D. C. Bradley, and T. D. Anthopoulos, Adv. Mater. 21, 2226 (2009).

[4] H. Yuan, H. Shimotani, A. Tsukazaki, A. K. Ohtomo, M. Kawasaki, and Y. Iwasa, Adv. Funct. Mater.19, 1046 (2009).

[5] J. B. Koo, C. H. Ku, S.C. Lim, S. H. Kim, J. H. Lee, Appl. Phys. Lett. 90, 133503 (2007).

[6] J. Lee, J. H. Kim, and S. Im, J. Appl. Phys. 95, 7 (2004).

[7] L. A. Majewski, M. Grell, S. D. Ogier, J. Veres, Organic Electronics 4, 27 (2003).

[8] L. A. Majewski, R. Schroeder, M. Grell, P. A. Glarvey, M. L. Turner, J. Appl. Phys. 96, 10 (2004)

[9] L. A. Majewski, R. S. Schroeder, and M. Grell, Adv. Mater. 17, No.2 (2005).

[10] J. Liu, D. B. Buchholz, R. P. H. Chang, A. Facchetti, and T. J. Marks, Adv. Mater., 22, 2333 (2010).

[11] A. Lu, J. Sun, J. Jiang, and Q. Wan, Appl. Phys. Lett. 96, 043114 (2010); W. Lim, E. A. Douglas, D. P. Norton, S. J. Pearton, F. Ren, Y. W. Heo, S. Y. Son, and J. H. Yuh, Appl. Phys. Lett. 96, 053510 (2010).

[12] B. N. Pal, B. M. Dhar, K. C. See, and H. E. Katz, Nature Mater. 8, 898 (2009).

[13] B. S. Ong, C. Li, Y. Li, Y. Wu, R. Loutfy, J. Am. Chem. Soc., 129, 2750 (2007).

[14] L. Wang, M. H. Yoon, G. Lu, Y. Yang, A. Facchetti, T. J. Marks, Nature Mater., 15, 893 (2006).

[15] C. Li, Y. Li, Y. Wu, B. S. Ong, R. O. Loutfya, J. Mater. Chem., 19, 1626 (2009).

[16] H. Q. Chianga, J. F. Wager, R. L. Hoffman, J. Jeong, D. A. Keszler, Appl. Phys. Lett., 86, 013503 (2005).

[17] H. S. Kim, M. G. Kim, Y. G. Ha, M. G. Kanatzidis, T. J. Marks, A. Facchetti, J. Am. Chem. Soc., 131, 10826 (2009).

[18] S. Jeong, Y. G. Ha, J. Moon, A. Facchetti, T. J. Marks, Adv. Mater., 22, 1346 (2010).

[19] K. Nomura, H. Ohta, A. Takagi, T. Kamiya, M. Hirano, H. Hosono, Nature, 432, 488 (2004).

[20] H. Hosono, T. Kamiya, K. Nomura, Dig. Tech. Papers AM-LCD 05, The Japan Society of Applied Physics, Tokyo, 2005, p. 83.

[21] K. Nomura, A. Takagi, T. Kamiya, H. Ohta, M. Hirano, H. Hosono, Jpn. J. Appl. Phys., 45,4303 (2006).

[22] H. Kumomi, K. Nomura, T. Kamiya, H. Hosono, Thin Solid Film. 516 ,1516 (2008).

[23] H. H. Hsieh, C. C. Wua, Appl. Phys. Lett. 91, 013502 (2007).

[24] S. Jeong, Y. Jeong, J. Moon, J. Phys. Chem. C, 112, 11082 (2008).

[25] S. J. Seo, C. G. Choi, Y. H. Hwang, B. S. Bae, J. Phys. D: Appl. Phys. 42, 035106 (2009).

[26] H. Bong, W. H. Lee, D. Y. Lee, B. J. Kim, J. H. Cho, K. Cho, Appl. Phys. Lett., 96, 192115 (2010).

[27] R. Martins, P. Barquinha, I. Ferreira, L. Pereira, G. Gonçalves, E. Fortunato, J. Appl. Phys., 101, 044505 (2007).

[28] L. Zhang, J. Li, X. W. Zhang, X. Y. Jiang, and Z. L. Zhang, Appl. Phys. Lett. 95, 072112 (2009).

[29] K. Okamura, N. Mechau, D. Nikolova, H. Hahn, Appl. Phys. Lett. 93, 083105 (2008).

[30] J. A. Letizia, J. Rivnay, A. Facchetti, M. A. Ratner, T. J. Marks, Adv. Funct. Mater., 20, 50 (2010).

[31] D. Gupta, M. Anand, S. W. Ryu, Y. K. Choi, S. Yoo, Appl. Phys. Lett. 93, 224106 (2008).

[32] W. J. Park, H. S. Shin, B. D. Ahn, G. H. Kim, S. H. Lee, K. H. Kim, H. Kima, Appl. Phys. Lett., 93, 083508 (2008).

[33] D. Kang, H. Lim, C. J. Kim, I. Song, J. C. Park, Y. S. Park, Appl.Phys. Lett., 90, 192101 (2007).

[34] P. T. Liu, Y. T. Chou, L. F. Teng, Appl. Phys. Lett., 95, 233504 (2009).

[35] J. K. Jeong, H. W. Yang, J. H. Jeong, Y. G. Mo, H. D. Kim, Appl. Phys. Lett., 93, 123508 (2008).

[36] D. H. Levy, D. Freeman, S. F. Nelson, P. J. Cowdery-Corvan, L. M. Irving, Appl. Phys. Lett., 92, 192101 (2008).

[37] J. Gao, K. Asadi, J. B. Xu, J. An, Appl. Phys. Lett. 94, 093302 (2009).

Chapter 7 Summary and Future Work

7.1 Summary

In this work, firstly, ferromagnetic properties of ZnO thin films prepared by spin-coating method have been meticulously investigated. The main conclusions can be withdrawn as following:

(a) Room temperature ferromagnetism can be observed in un-doped ZnO thin film, even without the magnetic doping. It is intrinsic, rather than from extrinsic impurities or substrates.

(b) The observed ferromagnetism is closely related to defects. By electrical and spectroscopic investigation, we tentatively attribute the major origin to oxygen vacancy defects, with which we include oxygen vacancy clusters and oxygen vacancy related complex defects. The magnetic moment is more likely induced in a charge transfer process of Zn and surrounding oxygen vacancies.

(c) Grain boundary and interface effect are not the main origins of ferromagnetism, because even in single crystalline ZnO, the ferromagnetism can be observed as well after annealing under high vacuum conditions.

(d) The magnetization moment can be tuned by additional donor doping, which is not necessarily magnetic ion. Both in the cases of highly conductive (Ga doped) and nearly insulating ZnO thin films, ferromagnetism can be observed, which indicates disparate mechanism of ferromagnetic coupling in different electrical conduction regimes. Carrier mediated ferromagnetism through band conduction electrons is possible in the highly conductive region, whereas a bound magnetic polaron model through localized electron states is attributed to accounting for the mechanism in the less conductive or nearly insulating regime.

As the second part, field effect properties of ZnO (doped and un-doped) thin films prepared by spin-coating method has been closely studied, based on both the traditional SiO_2/Si substrate and newly developed Al_2O_3/Si substrate.

(a)   The optimized and presumably easiest fabrication conditions of ZnO TFTs have been found in the lab ambient. Under this condition, by un-optimized doping (Ga and Li), the field effect mobility can be significantly increased, which is comparable to many devices demanding delicate and complex growth and annealing control of the active thin films;

(b)   In order to reduce the operation voltage of TFTs, we developed a gate dielectric by a new process (spin-coating). The spin-coated alumina has unique dielectric properties, in contrast to those grown by other methods, which is supposedly related to the protons introduced during spin-coating process. Although the capacitance is moderate, it is very effective to reduce the operation voltage. Field effect performance has been greatly improved, compared with those on SiO_2/Si substrate;

(c)   By doping proper dopants into ZnO (e.g. Ga and In in the present work), amorphous ZnO TFTs can be fabricated, which possess high field effect mobility, low operating voltage, low preparation temperature, and simplified fabrication process. With InGaZnO thin film annealed at $\sim 250°C$, the field effect mobility is as high as 18.3 $cm^{-2} V^{-1}s^{-1}$, which is larger than most other devices fabricated by solution-processing method;

(d)   Spin-coated alumina provides unique dielectric properties, excellent thermal stability, visible transparency, low cost, and seamless integration with oxide channel layers, which will probably pave the way for wide applications in transparent flexible electronics in future.

Although our study of field effect properties of ZnO thin films are simply charge based, it is expected that clues might be provided in future spintronic device investigation especially in the highly conductive regimes.

7.2 Recommendations for future study directions

Future work on ZnO based dilute magnetic semiconductors and thin film transistors can be continued.

(a) The mechanism of ferromagnetic coupling in ZnO thin films has not been completely clarified. With highly conductive ZnO thin films, anomalous hall effect dependence on the carrier concentration needs to be investigated before claiming field effect controlled ferromagnetism, which may provide powerful evidence of carrier mediated ferromagnetism;

(b) Starting from above, the magnetic performance of the highly conductive amorphous ZnO can be tried. If it is ferromagnetic, the electrical field tuning of AHE can be continued. This investigation may lay a foundation for amorphous ZnO based spin field effect transistors;

(c) For ZnO TFT with spin-coated alumina as the gate dielectric, current on-off ratio may be improved by a proper surface treatment before coating the active layer. The metal ratio in amorphous InGaZnO might be fine-tuned to obtain the largest field effect mobility, and the preparation temperature might be reduced further;

(d) Based on (c), fully transparent InGaZnO thin film transistors on certain transparent plastic substrates can be fabricated. Moreover, transistor arrays with logic functions can be obtained, which may find practical application in active matrix LCD technology.

(e) The stability of threshold voltage of thin film transistors is very crucial to practical applications. We have investigated the air stability of some devices. A more careful study on the bias stress test is in need in the future, which may help to find ways to pin the threshold voltage in a controllable way.

Publications and Submissions

1 **D. X. Xia,** F. Y. Xie, X. F. Wang, K. Xue, J. Chen and J. B. Xu, "Defect studies in un-doped ZnO thin films with room temperature ferromagnetism", *Journal of Magnetism and Magnetic Materials* (Revised).

2 **D. X. Xia**, W. H. Zhang, F. Y. Xie, J. Chen and J. B. Xu, "Reversible ferromagnetism study in un-doped ZnO thin films", *Journal of Nanoscience and Nanotechnology* (Accepted).

3 **D. X. Xia** and J. B. Xu, "High mobility and low operation voltage ZnGaO and ZnGaLiO transistors with spin-coated Al_2O_3 as gate dielectric", *Journal of Physics: D, Applied Physics, Fast track communication*，43 (2010) 4420.

4 **D. X. Xia** and J. B. Xu, "High mobility and low voltage amorphous metal oxide thin film transistors by low temperature solution-processing", in preparation.

Conferences

1 **D. X. Xia,** J. B. Xu and R. Zhang, *Ferromagnetism study of un-doped ZnO thin film*, **International Conference on Materials for Advanced Techonologies**, 2009, Singapore, E1-S10.6 (O), Oral Presentation.

2 **D. X. Xia**, F. Y. Xie, W. H. Zhang, J. Chen and J. B. Xu, *Reversible ferromagnetism study in un-doped ZnO thin films*, **IEEE International Nano Electronics Conference**, 2010, Hong Kong, EP429, Poster.

3 **D. X. Xia**, B. Liu, Z. B. Guo, R. Zhang and J. B. Xu, *Room temperature ferromagnetism in un-doped and Ga-doped ZnO thin films*, **International Conference on Nanoscience and Technology**, 2010, Beijing, P2-NST4-2, Poster.

Patent (pending)

D. X. Xia and J. B. Xu, A facile and low-cost process for oxide based dielectrics and semiconductors and transistors therefrom.